A NUMERICAL STUDY OF INHOMOGENEOUS, VARIABLE-DENSITY TURBULENCE AND MIXING IN PLANAR AND CONVERGENT GEOMETRIES

by

Ismael Djibrilla Boureima

A dissertation submitted to the faculty of
The University of North Carolina at Charlotte
in partial fulfillment of the requirements
for the degree of Doctor of Philosophy in
Mechanical Engineering

Charlotte

2019

Approved by:

_____
Dr. Praveen Ramaprabhu

_____
Dr. Yuri Godin

_____
Dr. Susan Kurien

_____
Dr. Mesbah Uddin

ABSTRACT

ISMAEL DJIBRILLA BOUREIMA. A Numerical Study of Inhomogeneous Variable-Density Turbulence in Planar and Convergent Geometries. (Under the direction of DR. PRAVEEN RAMAPRABHU)

Hydrodynamic instabilities govern the growth of perturbations at the interfaces between two fluids of different densities when subjected to an acceleration. The applied external acceleration can lead to the Rayleigh-Taylor (RT) instability, or when an impulsive acceleration in the form of an incident shock is applied, it leads to the Richtmyer-Meshkov (RM) instability. Such hydrodynamic instabilities, when allowed to develop, eventually lead to a turbulent state, characterized by vigorous mixing between the fluids. However, since the density difference between the fluids is finite, the turbulent flow is referred to as variable-density turbulence and is fundamentally different from its constant density counterpart. Such flows are observed in several natural and man-made situations including mixing in the upper atmosphere, supernovae explosions, nuclear fusion and shock-powered propulsion devices. A broad category of such flows was investigated using numerical simulations, enabled by multiple continuum codes, and the results of the study will be discussed.

Properties of variable density turbulence were studied in detail through the following flow configurations: Rayleigh-Taylor turbulence, doubly-shocked Richtmyer-Meshkov instability, and turbulence in a confined spherical implosion. These flows represent varying degrees of external forcing and anisotropy, and thus provide a framework to understand the response of turbulent properties to these variations of interest to engineering applications. Such studies can be instrumental in improving current turbulence models or

in manipulating mixing to achieve engineering objectives in applications. Numerical results from RT-turbulence including profiles of the turbulent mass flux, density-specific volume correlation and the turbulent kinetic energy were compared with a two-point spectral turbulence model. The double-shocked RM problem is of relevance to recent experiments at the National Ignition Facility in which multiple shocks whose strength and timing could be optimized, were used to maximize the fuel areal density and improve the neutron yield. In our hydrodynamic simulations of the double-shocked RM problem, we find the memory of the initial conditions at the instance of second shock recedes over a self-similar timescale, resulting in nearly universal growth rates at late times. Finally, we investigate the properties of variable-density turbulence occurring within an imploding mixing layer confined by spherical geometry.

ACKNOWLEDGEMENTS

I would like to first express my sincere gratitude to my advisor Dr. Ramaprabhu for believing in me and for the given opportunity and support of my Ph.D. study and related research. I am grateful for his teachings, his patience and dedication, and for his commitment and continuous motivation. This work will have not been possible without his guidance and help with my research in general and with the writing of this thesis. I could not have imagined having a better advisor and mentor for my Ph.D. study.

Besides my advisor, I would like to thank the rest of my thesis committee: Dr. Godin, Dr. Kurien, and Dr. Uddin, for their insightful comments and encouragement, but also for the hard question which incented me to widen my research from various perspectives.

I am also very grateful to Dr. Kurien and Dr. Pal who gave me the privileged opportunity to join their team as an intern. I am very grateful for their mentorship, for their continuous support, insights, and encouragement even after my internship. Further, I would also like to thank Dr. Aslangil and Dr. Livescu for providing their DNS data which was very useful and helpful for my research and work at the laboratory. The FLASH software used in this work was developed by the DOE-sponsored ASC/Alliance Center for Astrophysical Thermonuclear Flashes at the University of Chicago. We are grateful to Dr. Andrew Lawrie, at the University of Bristol for allowing the use of his software MOBILE. This work was supported in part by the (U.S.) Department of Energy (DOE) under Contract No. DE-AC52-06NA2-5396.

I thank my fellow lab mates in for the passionate and sometimes heated discussions, for the exchange of ideas and all the inspiration. I have learned a great deal from each of you. Thank you.

Last but not the least, I would like to thank my family: my parents, my wife, my brothers and sister, and my in-laws, for all the support and encouragement throughout my life in general.

TABLE OF CONTENTS

LIST OF FIGURES

LIST OF TABLES

CHAPTER 1 : INTRODUCTION AND LITERATURE REVIEW

Turbulent flows in which considerable density variations occur are of importance in several natural situations as well as man-made applications. Such flows play a prominent role in inertial confinement fusion (ICF) [1, 2], type 1a supernovae detonations[3-5] , shock-driven mixing in scramjets [6], mantle convection[7], and turbulent transport and mixing in the upper atmosphere [8, 9]. The sources of density variations in these applications can vary significantly, thereby affecting the mechanisms that govern the turbulent transport processes. Theoretical treatments and engineering models of such flows must take in to account these variations in turbulent mechanisms. In this work, we have investigated using detailed numerical simulations, the properties of variable density turbulent flows associated with the Rayleigh-Taylor (RT) and Richtmyer-Meshkov (RM) instabilities. The RT instability [10, 11] occurs under the conditions of an applied acceleration directed from a light fluid in to a heavy fluid, where the two fluids are separated by a perturbed interface. The RM instability [12, 13] may be considered a special case of the RT problem, in which the acceleration is impulsive such as that generated by a passing shock wave. Three configurations have been studied, and represent different drive profiles and levels of anisotropy in the flow: (i) self-similar Rayleigh-Taylor turbulence (constant drive), (ii) double-shocked RM turbulence (impulsive drive) and (iii) spherical implosion [14] (variable drive due to geometric confinement and Bell-Plesset effects[15, 16]).

The above flows have been shown to affect the outcome of imploding capsules in ICF, where the implosion has been initiated by laser ablation [17-25]. The fuel capsules consist of an ablator shell encasing Deuterium (DT) gas, so that the laser ablation creates a powerful

imploding shock that compresses the fuel to the point of runaway thermonuclear reactions. However, the presence of surface imperfections at the interface between the fuel and the shell material seeds the above instabilities which evolve to a turbulent state. The attendant turbulent mixing can thus compromise the neutron yield, thereby jeopardizing ignition. Such processes are modeled using multiphysics codes, in which the variable density turbulent mixing is described using low-order engineering models. Thus, detailed numerical simulations such as those reported in this work are essential in the validation of such low-order models. In the discussion below, we briefly describe the variable-density turbulent flows studied in this dissertation.

Rayleigh-Taylor Turbulence

The Rayleigh-Taylor [10, 11] instability occurs at a perturbed interface between fluids of different densities, when an acceleration is directed from the light fluid (ρ_1) to the heavy (ρ_2) fluid. When a single-wavelength (λ) disturbance is imposed at the interface, normal mode analysis [11, 26] predicts an early exponential growth of the perturbation amplitude with a growth rate ~ $\sqrt{Agk}$, where g is the magnitude of the acceleration vector, $k = \frac{2\pi}{\lambda}$ is the perturbation wavenumber, and the Atwood number $A \equiv \frac{\rho_2 - \rho_1}{\rho_2 + \rho_1}$ characterizes the strength of the density difference. At late times, the mode growth transitions to a nonlinear behavior characterized by *bubbles* of light fluid penetrating and displacing the heavy fluid which 'descends' as *spike* fingers. During this stage of development, potential flow models[27-32], in which the two fluids are represented by distinct velocity potential functions have proven useful in predicting the bubble and spike velocities.

When a spectrum of modes are present at the initial interface, individual modes with different wavenumbers can achieve nonlinear saturation and then merge to form larger

structures. The late-time flow is thus self-similar as $h(t) \sim \lambda(t) \sim t^2$. Specifically, experiments[33-38] and numerical simulations[35, 38-47] have shown growth of the mixing layer consistent with $h(t) = \alpha A g t^2$, where α is the self-similar growth constant. In RT turbulence, the production of TKE is sustained by a constant drive and an infinite reservoir of pure fluid to feed the mixing.

Doubly-shocked Richtmyer-Meshkov Instability

While RM-driven turbulent mixing has been extensively investigated, the majority of studies have focused on mixing from either a single incident shock or a reflected shock in the opposite direction. In a departure from these studies, and to shed light on pulse-shaping efforts recently underway that seek to exploit timed shocks in the same direction, we address using numerical simulations the behavior of the turbulent mixing layer in a doubly-shocked RM flow. The timing of the second shock was varied to obtain different amplitudes of the mixing layer at the time of the second shock, so that the effect of varying the "initial" state of the interface may be ascertained.

Thus, these simulations address recent efforts to optimize the timing and strength of shocks traversing the DT-ice layer to minimize the fuel entropy, while increasing compressibility[33]. In recent experiments, these ideas have been demonstrated for up to four shocks [48], with the ultimate goal of achieving the required areal densities to ensure ignition. The corresponding optimization problem will rely heavily on an accurate low-order description of the mix development following each shock. Our simulation results can be used to validate and refine such low-order models, which can then be used in multiphysics codes as well as in the design of target experiments. A detailed review of advances in

experiments, simulations and theoretical efforts related to the RM and RT instabilities was published recently in [49, 50].

Spherical Implosion

The implosion phase in inertial confinement fusion (ICF)[51] can be characterized by aggressive turbulent mixing between the hot fuel and the shell material. The turbulent mixing is driven by the RM [12, 13] and RT [10, 11] instabilities, and can act to degrade the overall yield of the process. To address these issues, there have been a vast array of studies of such canonical instabilities, although most of the efforts have been directed at the simpler, planar configuration. The effect of spherical convergence on the nature of such instabilities has been treated analytically[15, 16, 52] as well as through numerical simulations[14, 52-56]. We have investigated the behavior of turbulent mixing when the flow is constrained by a spherically confined geometry, as is the case with spherical implosions.

The effect of geometric convergence, due to either a cylindrical or spherical geometry, on the growth of the RT instability was illustrated by Bell and Plesset [15, 16], and collectively referred to as Bell–Plesset (BP) effects. At high convergence ratios, BP effects that are also termed "undriven growth" can significantly enhance the development of the underlying RT instability. In a series of papers [52, 53, 57], Mikaelian investigated the linear growth rates of Rayleigh–Taylor and Richtmyer–Meshkov [12, 13] instabilities in stratified cylindrical and spherical shells, using a potential flow approach. For cylindrical convergence, the BP effects are separable from the growth of driven instabilities such as RM/RT, while more complex expressions for the growth rate were obtained for the corresponding spherical problem. Lombardini [58, 59] developed a linear model for instability growth in both cylindrical and spherical geometries, based on the RM impulsive model, in the limit of RM

growth driven by a self-similar shock [60, 61]. The effect of viscosity on the linear growth of an RT-unstable spherical interface was examined by Terrones and Carrara [62] in the limit of infinite density ratio between the fluids. Finally, Ramshaw [63] developed a kinetic energy based model coupled with a wavelength renormalization approach to obtain expressions for both the linear and nonlinear growth rates of interfaces in spherical geometry.

In the rest of the chapter, we introduce terminology and definitions associated with turbulent flows, and review turbulence models for constant density and variable density turbulence.

1.1 **Review of statistical moments**

The Navier-Stokes (NS) equations are statements of conservation of mass, momentum, and energy, and provide instantaneous information on the independent variables (density ρ , the ith velocity component u_i, pressure p, the temperature T and the total energy E) at any point ($\boldsymbol{x}$, t):

$$\frac{\partial \rho}{\partial t} + \frac{\partial}{\partial x_i}(\rho u_i) = 0 \tag{1.1.1}$$

$$\frac{\partial}{\partial t}(\rho u_i) + \frac{\partial}{\partial x_i}\left(\rho u_i u_i + p\delta_{ij} - \sigma_{ij}\right) = \rho F_i \tag{1.1.2}$$

$$\frac{\partial}{\partial t}(\rho E) + \frac{\partial}{\partial x_i}\left[\rho u_i\left(E + \frac{p}{\rho}\right) - \sigma_{ij}u_j + q_i\right] = \rho F_i - u_i \tag{1.1.3}$$

where F_i is the ith component of the net external forces on the flow, $\sigma_{ij}$is the viscous stress, and is given for a Newtonian fluid by:

$$\sigma_{ij} = \mu\left[\left(\frac{\partial u_i}{\partial x_j} + \frac{\partial u_j}{\partial x_i}\right) - \frac{2}{3}\delta_{ij}\frac{\partial u_k}{\partial k}\right] \tag{1.1.4}$$

Where μ is the dynamic viscosity of the fluid, q_i is the heat flux and is given by Fourier's Law:

$$q_i = -\kappa \vec{\nabla} T = -\kappa \frac{\partial T}{\partial x_i} \tag{1.1.5}$$

In eq. (1.1.5), κ is the thermal conductivity of the fluid.

For the special case of an incompressible flow, in which the density is constant, the above equations simplify to:

$$\frac{\partial u_i}{\partial x_i} = 0 \tag{1.1.6}$$

$$\frac{\partial u_i}{\partial t} + u_j \frac{\partial u_i}{\partial x_j} + \frac{1}{\rho}\frac{\partial p}{\partial x_i} = \frac{1}{\rho}\frac{\partial \sigma_{ij}}{\partial x_i} \tag{1.1.7}$$

$$\sigma_{ij} = \mu\left(\frac{\partial u_i}{\partial x_j} + \frac{\partial u_j}{\partial x_i}\right) = \rho\nu\left(\frac{\partial u_i}{\partial x_j} + \frac{\partial u_j}{\partial x_i}\right) = 2\rho\nu s_{ij} \tag{1.1.8}$$

where ν is the kinematic viscosity of the fluid, and

$$s_{ij} = \frac{1}{2}\left(\frac{\partial u_i}{\partial x_j} + \frac{\partial u_j}{\partial x_i}\right). \tag{1.1.9}$$

Due to the absence of closed-form solutions, the irregular and chaotic nature of turbulent flows are often treated statistically where the independent variables are taken as pseudo-random functions of space and time. For instance, the Reynolds' decomposition [64], involves the decomposition of each instantaneous variable in to mean and fluctuating components. For constant density flows, the Reynolds decomposition of the independent variables gives:

$$u_i = \bar{u}_i + u'_i \tag{1.1.10}$$

$$p = \bar{p} + p' \tag{1.1.11}$$

$$\rho = \bar{\rho} + \rho' \tag{1.1.12}$$

$$\sigma_{ij} = \overline{\sigma_{ij}} + \sigma'_{ij} \tag{1.1.13}$$

where the overbar ($\bar{}$) denotes mean (averaged) quantities, while prime (′) is used to denote fluctuations about the mean quantity. i.e. in eq. (1.1.12), ρ is the instantaneous density, and

ρ' is the density fluctuation about the mean density $\bar{\rho}$. For an instantaneous variable q, the corresponding mean value over a region $d\Omega$ is obtained by:

$$\bar{q}(t) = \frac{1}{\Omega}\int_{\Omega} q(t,x,y,z)d\Omega \tag{1.1.14}$$

Introducing the Reynolds decomposed variables from eqs. (1.1.10) - (1.1.13) into the incompressible NS equations (1.1.6) – (1.1.9) lead to the Reynolds-decomposed NS equations

$$\frac{\partial(\bar{u}_i+u'_i)}{\partial x_i} = 0 \tag{1.1.15}$$

$$\frac{\partial(\bar{u}_i+u'_i)}{\partial t} + \left(\bar{u}_j + u'_j\right)\frac{\partial(\bar{u}_i+u'_i)}{\partial x_j} + \frac{1}{\rho}\frac{\partial(\bar{p}+p')}{\partial x_i} = \frac{1}{\rho}\frac{\partial(\overline{\sigma_{ij}}+\sigma'_{ij})}{\partial x_i}. \tag{1.1.16}$$

1.2 **Turbulence models for constant density and variable density turbulence**

The above equations can be ensemble-averaged to yield a set of equations for the mean flow referred as the Reynolds Averaged Navier-Stokes (RANS) equations given below:

$$\frac{\partial \bar{u}_i}{\partial x_i} = 0 \tag{1.1.17}$$

$$\frac{\partial \bar{u}_i}{\partial t} + \bar{u}_j\frac{\partial \bar{u}_i}{\partial x_j} + \frac{1}{\rho}\frac{\partial \bar{p}}{\partial x_i} = \frac{1}{\rho}\frac{\partial}{\partial x_i}\left(\overline{\sigma_{ij}} + R_{ij}\right) \tag{1.1.18}$$

$$R_{ij} = -\overline{u'_i u'_j} \tag{1.1.19}$$

Here, R_{ij} is the turbulent Reynolds stress [65], and incorporates the effects of unresolved turbulent fluctuations on the mean flow, which can significantly enhance the mean transport. The Reynolds stress is a symmetric tensor and introduces six additional unknowns, leading to the widely discussed closure problem associated with the RANS equations. Thus, turbulence modeling refers to the class of theoretical treatments that develop and provide necessary closures by relating the components of R_{ij} and other high-order terms to the mean flow quantities.

Extensive work has been reported in the literature on constant density turbulence including Eddy Viscosity Models (EVM) based on Boussinesq's eddy viscosity approximation [66], consisting of the "Algebraic models" [67-69], 'one-equation models' [70-73] and "two-equation models"[74-79]. Higher-order turbulence models can be obtained by deriving a full transport equation for the Reynolds stress tensor from the fluctuating field equations obtained by subtracting the mean flow equations (1.1.17 - 1.1.18) from the Reynolds-decomposed NS equations (1.1.15 - 1.1.16) as detailed in [65]. Such models include the second order two-equation transport models of [80-82].

Besnard [83](BHRZ) expressed the Reynolds stress in the form of two-point statistical correlations computed at distinct points $\boldsymbol{x_1}$ and $\boldsymbol{x_2}$. This is often done in conjunction with deriving an exact but unclosed, transport equation for the Reynolds stress. The resulting equations are then expressed in terms of the separation distance $\boldsymbol{r = x_1 - x_2}$ and the center of mass $\boldsymbol{x = (x_1 + x_2)/2.}$ These equations in ($\boldsymbol{x}$, $\boldsymbol{r}$)-space are Fourier-transformed with respect to the separation variable ($\boldsymbol{r}$), and shell-averaged in k-space. Some of the popular two-point constant density turbulence models include the Eddy-Damped Quasi- Normal Markovian (EDQNM) models proposed by [84-87] , and the diffusion approximation proposed by Besnard[83].

Unlike with constant density flows, the understanding and modeling of variable-density turbulence is still in its early stages. Variable-density flows can involve incompressible fluids of different density, where the density variation in such flows results from the mixing of the different fluids. Variable-density flows are better described by the Favre-Reynolds Averaged Navier-Stokes (FRANS) equations which provide a conservative form of the Reynold stress tensor in the averaged momentum equations. The FRANS equations are

obtained following the same steps taken in deriving the RANS equation, however mass-weighted Favre-averaging is used instead for the calculation of mean quantities. The Favre mean associated with any instantaneous quantity q is defined as $\tilde{q} = \langle \rho q \rangle / \langle \rho \rangle$, and the corresponding Favre fluctuations are given by $q'' = q - \tilde{q}$. The resulting FRANS equations from the Favre-decomposed and ensemble averaged NS equations are given by:

$$\frac{\partial \bar{\rho}}{\partial t} + \frac{\partial}{\partial x_i}(\bar{\rho}\tilde{u}_\iota) = 0 \tag{1.1.24}$$

$$\frac{\partial}{\partial t}(\bar{\rho}\tilde{u}_\iota) + \frac{\partial}{\partial x_j}(\bar{\rho}\tilde{u}_\iota\tilde{u}_\jmath + \bar{p}\delta_{ij} + \overline{\rho u_\iota'' u_\jmath''} - \overline{\sigma_{\jmath\iota}}) = 0 \tag{1.1.25}$$

Variable density extensions to single-point, two-equation transport models [84-86, 88, 89], transporting additional terms such as the density-specific volume correlation and the mass flux velocity respectively defined in eqs. (1.1.31) and (1.1.28) below.

Similar to the constant density turbulence case, spectral models can be obtained from the two-point statistical treatment of the governing equations. Clark and Spitz[90] (CS1995) define the turbulent Reynolds stress tensor as

$$R_{ij}(x_1, x_2, t) = \overline{\frac{1}{2}[\rho(x_1, t) + \rho(x_2, t)]u_\iota''(x_1, t)u_\jmath''(x_2, t)}\ . \tag{1.1.26}$$

The authors in (CS1995) [90] have chosen the form in (1.1.26) to satisfy symmetry in x_1 and x_2, recovery of the single-point form as $x_1 \to x_2$, and requiring R_{ij} vanish for $|x_1 - x_2| \to \infty$. They derive a full but unclosed transport equation for R_{ij} from the FRANS equations, which is reproduced here from (CS1995) [90]:

$$\frac{\partial R_{ij}(\mathbf{x}_1, \mathbf{x}_2)}{\partial t} + \frac{\partial}{\partial x_{1n}}\left[R_{ij}(\mathbf{x}_1, \mathbf{x}_2)\tilde{u}_n(\mathbf{x}_1)\right] + \frac{\partial}{\partial x_{2n}}\left[R_{ij}(\mathbf{x}_1, \mathbf{x}_2)\tilde{u}_n(\mathbf{x}_2)\right]$$

$$+R_{in}(\mathbf{x}_1, \mathbf{x}_2)\frac{\partial \tilde{u}_j(\mathbf{x}_2)}{\partial x_{2n}} + R_{nj}(\mathbf{x}_1, \mathbf{x}_2)\frac{\partial \tilde{u}_i(\mathbf{x}_1)}{\partial x_{1n}}$$

$$-\frac{1}{2}R_{ij}(\mathbf{x}_1,\mathbf{x}_2)\left[\frac{\partial\tilde{u}_n(\mathbf{x}_2)}{\partial x_{2n}}+\frac{\partial\tilde{u}_n(\mathbf{x}_1)}{\partial x_{1n}}\right]-\frac{1}{2}\left[H_{ij}^{R^{(+)}}(\mathbf{x}_1,\mathbf{x}_2;\mathbf{x}_2)+H_{ji}^{R^{(+)}}(\mathbf{x}_2,\mathbf{x}_1;\mathbf{x}_1)\right]$$

$$-\frac{1}{2}R_{ij}^{(-)}(\mathbf{x}_1,\mathbf{x}_2)\left[\frac{\partial\tilde{u}_n(\mathbf{x}_2)}{\partial x_{2n}}-\frac{\partial\tilde{u}_n(\mathbf{x}_1)}{\partial x_{1n}}\right]-\frac{1}{2}\left[H_{ij}^{R^{(-)}}(\mathbf{x}_1,\mathbf{x}_2;\mathbf{x}_2)-H_{ji}^{R^{(-)}}(\mathbf{x}_2,\mathbf{x}_1;\mathbf{x}_1)\right]$$

$$+\frac{\partial T_{ijn}^{R^{(+)}}(\mathbf{x}_1,\mathbf{x}_2;\mathbf{x}_2)}{\partial x_{1n}}+\frac{\partial T_{jin}^{R^{(+)}}(\mathbf{x}_2,\mathbf{x}_1;\mathbf{x}_1)}{\partial x_{2n}}$$

$$=\frac{1}{2}\left\{\Psi_{ij}^{R}(\mathbf{x}_1,\mathbf{x}_2)+\Psi_{ji}^{R}(\mathbf{x}_2,\mathbf{x}_1)\right\}$$

$$+\frac{1}{2}\left\{\left[a_i(\mathbf{x}_1,\mathbf{x}_2)-\frac{m_i(\mathbf{x}_1,\mathbf{x}_2)}{\bar{\rho}(\mathbf{x}_2)}\right]\frac{\partial\bar{\sigma}_{nj}(\mathbf{x}_2)}{\partial x_{2n}}+\left[a_j(\mathbf{x}_2,\mathbf{x}_1)-\frac{m_j(\mathbf{x}_2,\mathbf{x}_1)}{\bar{\rho}(\mathbf{x}_1)}\right]\frac{\partial\bar{\sigma}_{in}(\mathbf{x}_1)}{\partial x_{1n}}\right\} \quad (1.1.27)$$

New auxiliary correlations appear in the equation for R_{ij}, which some are of the same or lower order than R_{ij}- these are a_i, m_i, and R_{ij}^{-} given below from (CS1995):

$$a_i(x_1,x_2,t)=\overline{u_i''(x_1,t)\rho(x_1,t)v(x_2,t)} \quad (1.1.28)$$

$$m_i(x_1,x_2,t)=\overline{u_i''(x_1,t)\rho'(x_2,t)} \quad (1.1.29)$$

$$R_{ij}^{-}(x_1,x_2,t)=\overline{\frac{1}{2}[\rho(x_1,t)-\rho(x_2,t)]u_i''(x_1,t)u_j''(x_2,t)}. \quad (1.1.30)$$

Additionally, unclosed transport equations are derived for those lower order correlations as well[90]. A new correlation, the density-specific volume correlation (b), appears in both the equation of a_i and m_i, and is defined as:

$$b=-\overline{\rho'(x_1,t)v'(x_2,t)} \quad (1.1.31)$$

with $v=\frac{1}{\rho}$. As explained by Livescu[91], b is an indicator of mixing that takes values between 0 (when the flow is fully mixed) and 1 (when the fluids are segregated), and is responsible for setting the buoyancy production rate; the turbulent mass flux a_i on the other hand mediates the conversion of the buoyant potential energy into turbulent kinetic energy

(TKE); thus both playing an important role in turbulence. The reader is referred to (CS1995) for the transport equations of a_i, m_i R_{ij}^- and b.

The higher order correlations appearing in the derived transport equation for of a_i, m_i R_{ij}^- and b include the turbulent dilatation terms (H-terms: H_{ij}), the triple correlations (T-terms: T_{ij}), and the fluctuating pressure-viscous strain correlations (ψ -terms: ψ_{ij}). Their general form in the transport equation of any turbulence quantity, say $\overline{\phi}$ ($\overline{\phi}$ can be a_i, m_i R_{ij}^- or b.), are given bellow from (CS1995):

$$H^{\overline{\phi}}(x_1, x_2; x', t) = \overline{\phi(x_1, x_2, t)} \frac{\partial a_n(x')}{\partial x'} + \hat{H}^{\overline{\phi}}(x_1, x_2; x', t) \tag{1.1.30}$$

$$\begin{aligned} T_{\dots n}^{\overline{\phi}}(x_1, x_2; x', t) &= \overline{\phi_{\dots}(x_1, x_2, t) u_n''(x')} \\ &= \overline{\phi(x_1, x_2, t)} a_n(x') + \hat{T}^{\overline{\phi}}(x_1, x_2; x', t) \end{aligned} \tag{1.1.31}$$

$$\begin{aligned} \psi_{i\dots j}^{\overline{\phi}}(x_1, x_2, t) &= \overline{[\overline{\phi}_{i\dots}(x_1, x_2, t) + \phi'_{i\dots}(x_1, x_2, t)]\left[\overline{\pi}_j(x_2, t) + \pi'_j(x_2, t)\right]} \\ &= \overline{\phi}_{i\dots}(x_1, x_2, t)\overline{\pi}_j(x_2, t) + \overline{\phi'_{i\dots}(x_1, x_2, t)\pi'_j(x_2, t)} \end{aligned} \tag{1.1.32}$$

Where

$$\hat{H}^{\overline{\phi}}(x_1, x_2; x', t) = \overline{\phi(x_1, x_2, t) \frac{\partial u_n'(x', t)}{\partial x'}},$$

$$\hat{T}_{\dots n}^{\overline{\phi}}(x_1, x_2; x', t) = \overline{\phi_{\dots}(x_1, x_2, t) u_n'(x', t)},$$

$$\pi_j(x, t) = \overline{v(x, t) \frac{\partial \sigma_{nJ}'(x)}{\partial x_n}}.$$

As explained above, spectral models are obtained by a transformation of coordinate from $[\boldsymbol{x_1}; \boldsymbol{x_2}]$ to $[\boldsymbol{r} = \boldsymbol{x_1} - \boldsymbol{x_2}; \boldsymbol{x} = (\boldsymbol{x_1} + \boldsymbol{x_2})/\boldsymbol{2}]$, and by Fourier transformation with respect to $\boldsymbol{r}$. The components of the resulting Fourier transformed correlations equations evolving the real spectrum are shell-averaged[90] (Imaginary terms and terms multiplied ik_n are dropped); consequently

No transport equations are derived for these higher order terms, but their final forms in the shell averaged transport equations for a_i, m_i R_{ij}^{-} and b in k-space will be modeled. the $\widehat{H}^{\bar{\phi}}$-terms which represent the production or destruction (or both) of turbulence due to the dilation of the fluctuating velocity field are modeled as diffusive/dissipative terms; the $\widehat{T}_{\ldots n}^{\bar{\phi}}$-terms are modeled as an advection/diffusion terms with the possibility of an altercation of cascade due to the presence of density fluctuation in k-space, and The ψ -terms are modeled based on dimensional consistency, physical arguments and analogy with the constant density case. The resulting model for the ψ –terms include a 'slow part' that mimic tendency to isotropy which is modeled in direct analogy to constant-density[83] and a 'rapid part' that couples spectral tensor to mean flow velocity gradient. Other modeling strategies are varied and include approaches in [88, 89, 92-106]. Steinkamp[106, 107] (SCH) proposed an extension of the two-point spectral model of (CS1995) to inhomogeneous variable density flows given below:

$$\frac{\partial R_{nn}}{\partial t} = -\frac{\partial R_{nn}\tilde{\mathrm{u}}_y}{\partial x} + \int_{-\infty}^{\infty} 2a_x \frac{\partial \bar{p}}{\partial x}(k\exp(-2k|x'-x|))dx' - 2R_{xx}\frac{\partial \tilde{\mathrm{u}}_x}{\partial x}$$
$$+ C_d \frac{\partial}{\partial x}\nu_t \frac{\partial R_{nn}}{\partial x} + \frac{\partial}{\partial k}\left[k\Theta^{-1}\left[-C_{r1}R_{nn} + C_{r2}k\frac{\partial R_{nn}}{\partial k}\right]\right]$$
$$-2\nu k^2 R_{nn} \qquad (1.1.33)$$

$$\frac{\partial R_{xx}}{\partial t} = -\frac{\partial R_{xx}\widetilde{u_x}}{\partial x} + \int_{-\infty}^{\infty} 2a_x \frac{\partial \bar{p}}{\partial x}(k\exp(-2k|x'-x|))dx' - 2R_{xx}\frac{\partial \tilde{\mathrm{u}}_x}{\partial x}$$
$$+ C_d \frac{\partial}{\partial x}\nu_t \frac{\partial R_{xx}}{\partial x} + \frac{\partial}{\partial k}\left[k\Theta^{-1}\left[-C_{r1}R_{xx} + C_{r2}k\frac{R_{xx}}{\partial k}\right]\right]$$
$$+ C_m \int_0^k \sqrt{\frac{kR_{nn}}{\bar{p}}}\,dk\left(\frac{1}{3}R_{nn} - R_{xx}\right) \qquad (1.1.34)$$

$$\frac{\partial a_x}{\partial t} = -\tilde{u}_x \frac{\partial a_x}{\partial x} + \frac{b}{\bar{\rho}} \frac{\partial \bar{p}}{\partial x} - \left[C_{rp1} k^2 \sqrt{a_n a_n} + C_{rp2} \Theta^{-1}\right] a_x - \frac{R_{xx}}{\bar{\rho}^2} \frac{\partial \bar{\rho}}{\partial x}$$

$$+ \frac{\partial}{\partial k}\left[k\Theta^{-1}\left[-C_{a1} a_x + C_{a2} k \frac{\partial a_x}{\partial k}\right]\right] + C_d \frac{\partial}{\partial x} \nu_t \frac{\partial a_x}{\partial x} \qquad (1.1.35)$$

$$\frac{\partial b}{\partial t} = \left(\frac{2\bar{\rho} - \rho_1 - \rho_2}{\rho_1 \rho_2}\right) \frac{\partial \bar{\rho} a_x}{\partial x} - C_{fb}\left[\bar{\nu}^2 \frac{\partial}{\partial x}\left(\frac{\bar{\rho}}{\bar{\nu}}\right)\right] \frac{\partial k a_x}{\partial k}$$

$$+ \frac{\partial}{\partial k}\left[k\Theta^{-1}\left[-C_{b1} b + C_{b2} k \frac{\partial b}{\partial k}\right]\right]$$

$$+ C_d \frac{\partial}{\partial x} \nu_t \frac{\partial b}{\partial x} - C_{db} k^2 D b \qquad (1.1.36)$$

In the above set of equations, $\nu_t = \int_0^\infty \sqrt{\frac{kR_{nn}}{\bar{\rho}} \frac{dk}{k^2}}$ is the turbulent eddy viscosity, and $\Theta^{-1} = \sqrt{\int_0^{k_1} \frac{k^2 R_{nn}}{\bar{\rho}} dk}$ is the eddy turn over. $C_{\phi 1}$ and $C_{\phi 2}$ are dimensionless model constants that appear in the model for the cascade terms ($\hat{T}^{\bar{\phi}}_{\ldots n}$-terms), C_{rp1} and C_{rp2} appear in the model for the fluctuating pressure term, which is modeled as drag, and C_d appears in the model for the $\hat{H}^{\bar{\phi}}$-terms, modeled as diffusive dissipative terms. The reader is referred to (SCH) and (CS1995) for additional details on modeling.

The Local Wavenumber (LWN) model, which is derived from the model proposed by (SCH)[106, 107] is under active development at LANL, and was recently validated for the case of homogeneous variable density turbulence by [108] using high resolution DNS data. In Chapter 3, we will discuss early results of our efforts in the validation of the LWN model for inhomogeneous turbulent flow case (RT turbulence) in the Boussinesq limit using ILES simulations.

CHAPTER 2 : NUMERICAL METHODS

In this chapter, we briefly review the numerical methods employed in the investigation of variable density turbulent flows. For additional details on these methods and codes, the reader is referred to [109-112] (FLASH) and [113-116] (MOBILE).

FLASH: The compressible flow simulations including the double-shocked RM, spherical RM and implosion cases were performed using the astrophysical FLASH[109-112] code developed at the University of Chicago's FLASH center. FLASH is a multi-physics code in which compressible gas dynamics is described as solutions to the Euler equations. A split version of the direct Eulerian Piecewise Parabolic Method (PPM) [117] solver was used in this study. Discontinuities between grid cells were treated by solving a local Riemann problem across the boundaries separating adjacent computational cells. The conservative flow variables are advanced in time using the fluxes obtained from solving the local Riemann problem, using an explicit forward in time difference scheme. The resulting algorithm is 2nd order accurate both in time and space, and has been demonstrated to be well suited to describing flows involving shocks and contact discontinuities such as sharp material interfaces.

Thermodynamic properties in FLASH are calculated using a multi-gamma ideal gas equation of state capable of handling multiple species. FLASH is also equipped with Adaptive Mesh Refinement (AMR) capability (through the PARAMESH [118] software suite which allows for the allocation of mesh resources to localized regions of interest within the flow, identified by a threshold value of the second derivatives of the flow variables. All the above features are also available in curvilinear coordinates, which is taken advantage of in

the current study to investigate turbulent RM and implosions in spherical geometries. It was shown in [54] from a comparison of implosion studies using Cartesian and curvilinear geometry codes that during periods of high convergence in the flow, misalignments between the interface and the mesh boundaries can render the interface more unstable to numerical errors and perturbations. FLASH is a massively parallel code, where the parallelism is achieved using the Message Passing Interface (MPI) protocol, and has demonstrated (near-linear) scaling on over 64k processor cores, and across multiple computing platforms [111].

MOBILE: The incompressible RT simulations described in chapter 3 were performed using MOBILE [113-116], a three-dimensional, hydrodynamic Navier-Stokes solver, developed at the University of Bristol. In MOBILE, computational expediency is achieved through splitting the incompressible governing equations (1.1.1 - 1.1.2) in to hyperbolic (advective transport), and non-hyperbolic (diffusion and viscous dissipation) and elliptic (pressure and velocity correction) components. MOBILE employs a split, high-order advection scheme using a fractional step approach comprised of a sequence of one-dimensional updates of the conserved variables. This is accomplished in the sequence of sweeps [X-Y-Z-Z-Y-X], which results in a net truncation error that is second order [119]. Fluxes of conserved variables are obtained by solving a local Riemann problem at each cell-interface with the left and right states obtained from a piecewise polynomial reconstruction of the most recent cell-centered values from neighboring cells.

Pressure correction to enforce the solenoidal property of the velocity field is achieved through a projection step, in which solution acceleration of the Poisson equation is accomplished using a multi-grid solver. MOBILE uses a uniform mesh, while MPI

protocol coupled with domain decomposition ensures highly scalable parallel performance. MOBILE has been validated for several fluid mixing and transport problems including single-mode and multimode Rayleigh-Taylor flows [113-116], Kelvin-Helmholtz instability [113], and lock-release gravity currents [113].

Implicit Large Eddy Simulations: Both MOBILE and FLASH are capable of handling simulations in which viscous and mass diffusion effects are included with fidelity. We refer to these simulations as Navier-Stokes calculations, although the term Direct Numerical Simulations is often used (and misused) in the literature. In certain cases, such as the shock-driven RM flows, a significant economy in computational costs can be achieved by solving the Euler equations instead. Such calculations are referred to as Implicit Large Eddy Simulations (ILES) [120], where the numerical scheme is tailored to ensure that for turbulent flows, simulated energy dissipation is consistent with a real fluid. This removes the need to simulate additional viscous diffusive terms that would reduce the range of dynamically significant scales that can be captured.

In ILES, small-scale dissipation is modeled numerically, thus eliminating the need for an explicit sub-grid filter with tunable coefficients. Aspden[121] developed a scaling analysis for the grid-dependent, numerical dissipation observed in such methods, from which an effective Kolmogorov scale was inferred, which can then be used to infer an equivalent numerical viscosity and Reynolds number. A similar approach was adopted in the code comparison study by [47], who deduced an effective numerical dissipation $\varepsilon_{numerical}$ from the implied Kolmogorov scales in the energy spectra. MOBILE and FLASH when operating as ILES codes, produce dissipative spectra consistent with the expected $E(k) \sim k^{-3}$ scaling observed in experiments and DNS[122] calculations.

One attractive feature of ILES methods relevant to RT and RM simulations is their ability to preserve monotonicity of the solution, even in the presence of discontinuous sharp flow features such as shocks or material interfaces. In contrast, when such sharp interfaces and contact lines are described using methods classified as DNS, oscillations due to Gibbs phenomena may often occur. To avoid these oscillations, DNS calculations of RT flow are often initialized with diffuse interfaces, resulting in an initial instability growth rate modified by the thickness of the interface. Note that the accurate description of the initial growth rate is critical since it determines the initial saturation amplitudes of the dominant modes, and thus the overall amplitude trajectory to self-similarity.

CHAPTER 3 : BOUYANCY DRIVEN VARIABLE-DENSITY TURBULENCE.

In this section, we describe detailed numerical simulations of the Rayleigh-Taylor (RT) instability-driven variable density turbulence using MOBILE, the results from which are then compared with the predictions of the LWN model. The simulations were carried out in the Boussinesq regime, with an Atwood number, A = 0.05. RT turbulence has extensively been studied [39-41, 115, 116, 122-128] and hence serves as a benchmark problem to validate our simulation techniques. In § 3.1, we describe the problem setup, followed by a discussion of ILES results and comparison with the LWN model in § 3.3.

3.1 **Problem Description and Numerical Setup**

The 3D simulations were performed in a rectangular domain shown in figure 3.1, with dimensions of $L_0 = 2\pi$ cm in the homogeneous (*y*-, *z*-) directions, and $4L_0$ in the direction of the applied acceleration (*x*-). Periodic boundary conditions were employed in the homogeneous directions, while the *x*-boundaries were treated as outflow surfaces. A uniform mesh resolution of 512 zones/L_0 was employed in all directions. The flow was initialized with a light fluid of density ρ_1 and a heavy fluid of density ρ_2 as shown in Figure 3.1, with a density ratio of $\frac{\rho_2}{\rho_1} = 1.10526$ (Atwood number of 0.05), initially interfacing at $x_c = L_x/2$. The light fluid is accelerated into the heavier fluid with an applied acceleration $g_x = -2\ cm.s^{-2}$, and a multimode perturbation is imposed at the interface separating the two fluids, given by the function [47] :

$$h(y,z,t=0) = \sum_{k_y\,k_z} \begin{bmatrix} a_k\ \cos(k_y\ y)\ \cos(k_z\ z) + \\ b_k\ \sin(k_y\ y)\ \sin(k_z\ z) + \\ c_k\ \cos y\ y)\ \cos(k_z\ z) + \\ d_k\ \sin(k_y\ y)\ \sin(k_z\ z) \end{bmatrix} \tag{3.1.1}$$

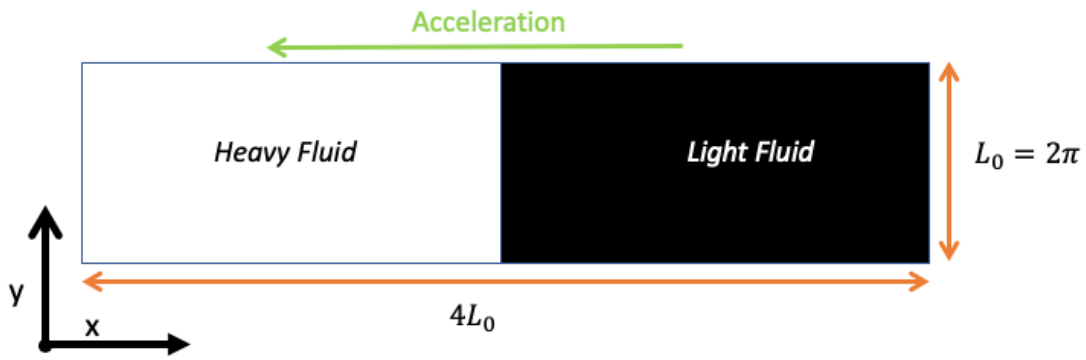

Figure 3. 1 Schematic of the computational domain for the turbulent RT simulations. Image represents a cross-section and shows the initial fluids and the direction of the applied acceleration.

where a_k, b_k, c_k, and d_k are random amplitudes. The perturbation modes in eq. (3.1.1) were chosen to be from a narrow-band spectrum in modenumber space in the range (32 - 64). Such an initial perturbation adapted from [47] ensures the development of self-similar turbulence through growth and early-onset saturation and mode-coupling of nonlinear modes.

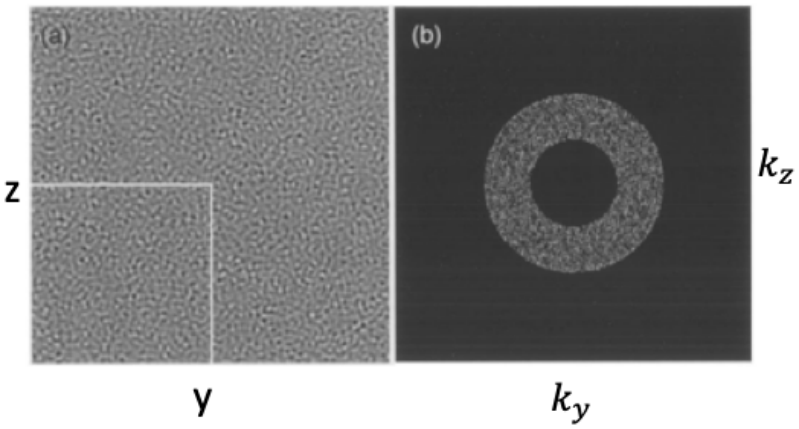

Figure 3. 2 Representation of the initial perturbation spectrum in (a) physical space and (b) wavenumber space. Images are reproduced from [47] .

3.2 **Results and Discussion**

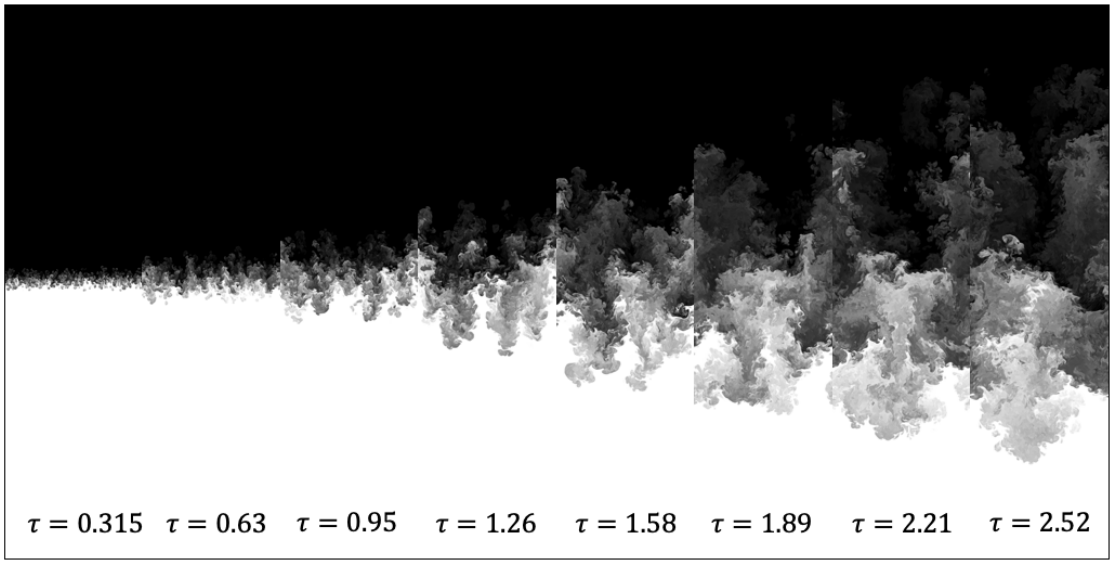

Figure 3. 3 Contours of volume fraction at the center (x-y) plane, showing the growth of the turbulent RT mixing layer at different non-dimensional times.

Contours of the volume fraction of the light fluid on the center plane (*x*-*y*) at different times in our simulation are plotted in figure 3.3. Since the simulations were performed in the Boussinesq limit, the growth of bubble and spike fronts are symmetric at late times. The process of mode-coupling is evident in these figures as fine-scale features that appear at early times undergo pairing across k-space so that at late times, only a few bubble and spike structures remain.

As before, plots of the density-specific volume covariance b, turbulent mass flux a_x, and the turbulent kinetic energy $\tilde{k} = R_{nn}/(2\bar{\rho})$ are plotted in non-dimensional time τ in figure 3.4 (a) – (c) respectively. These quantities were computed by averaging over the homogeneous directions at the mid-plane. We follow the widely used non-dimensionalization for time defined as:

$$\tau = t\sqrt{Ag/L_0} \tag{3.2.1}$$

and similarly, we define a characteristic velocity as:

$$U_0(\tau) = \sqrt{AgW(\tau)}, \tag{3.2.3}$$

and scale a_x and $\tilde{k}$ with U_0 and $\rho_0 U_0^2$ respectively, where $\rho_0 = \frac{\rho_1+\rho_2}{2}$ in eq. (3.2.3), $W(\tau)$ is the mixing layer width at scaled time τ, and is computed from volume fraction of light and heavy fluids respectively f_1 and f_2, using [129]:

$$W(\tau) = 6\int \overline{f}_1\overline{f}_2 dx, \tag{3.2.4}$$

where $\overline{\ }$ denote planar averages in the *y*-*z* plane.

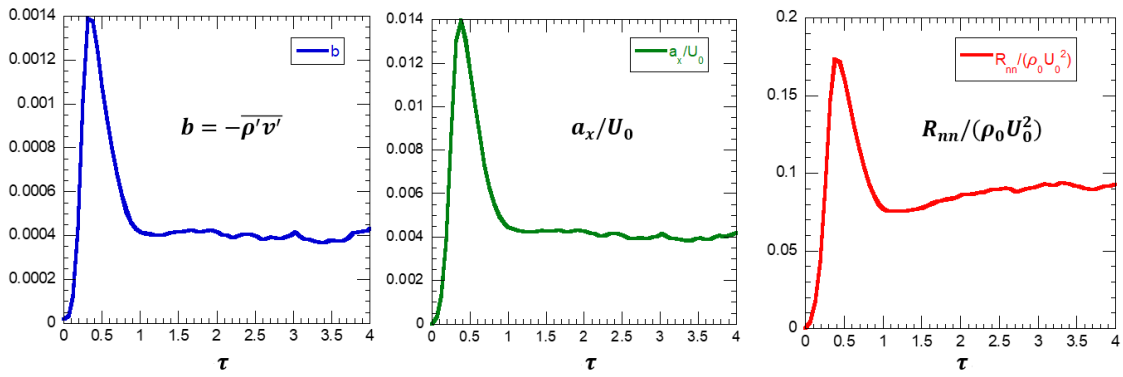

Figure 3. 4 Time evolution of centerline planar averages of (a) the density-specific volume correlation *b*, (b) the mass flux in the x-direction a_x scaled by U_0, and (c) the trace of the turbulent stress tensor R_{nn} scaled by $\rho_0 U_0^2$

At early times in figure 3.4 (a), the initially low values of *b* is an artifact of the initialization procedure in our simulations, and does not indicate the presence of completely mixed fluids. The initial amplitude perturbations from eq. (3.1.1) are converted to volume fraction perturbations with a sub-cell resolution using a linear interpolation procedure. Thus, within a cell, the density of the fluid is computed (based on f_1) and registers as a 'mixed' fluid in

the definition of b. As the flow develops, and structures on the interface grow to occupy multiple cells, the definition of b becomes a more reliable indicator of mixing. As the flow becomes nonlinear and transitions to turbulence, the attendant mixing results in an increase in b. At late times, the mid-plane features large bubble and spike plumes which transport pure fluid within them, leading to higher values of b.

We scale the x-direction mass flux a_x with the characteristic RT velocity U_0, which represents the nonlinear velocity of dominant structures within the mixing layer. The time evolution of the scaled mass flux is shown in figure 3.4 (b). Note that the initial spike is associated with the linear stage of growth, and is due to initially low values of the scaling velocity U_0. As the flow transitions to self-similarity, a_x/U_0 is dominated by leading bubble and spike structures (with velocities $\sim \tau$), and saturates to a constant value as expected. At late times, there is a gradual increase in the scaled mass flux due to the effect of the exit boundaries on the edges of the mixing layer. The scaled TKE in figure 3.4 (c) exhibits similar features as the mass flux: initial spike due to the linear growth rate exceeding the self-similar scaling, later saturation as the flow enters self-similarity and the late-time increase due to boundary effects. RT-turbulence is observed to be driven and sustained by the persistent acceleration and continuous supply of fresh material from the infinite reservoirs of pure fluid present outside the mixing zone.

3.3 **Comparison with LWN Model**

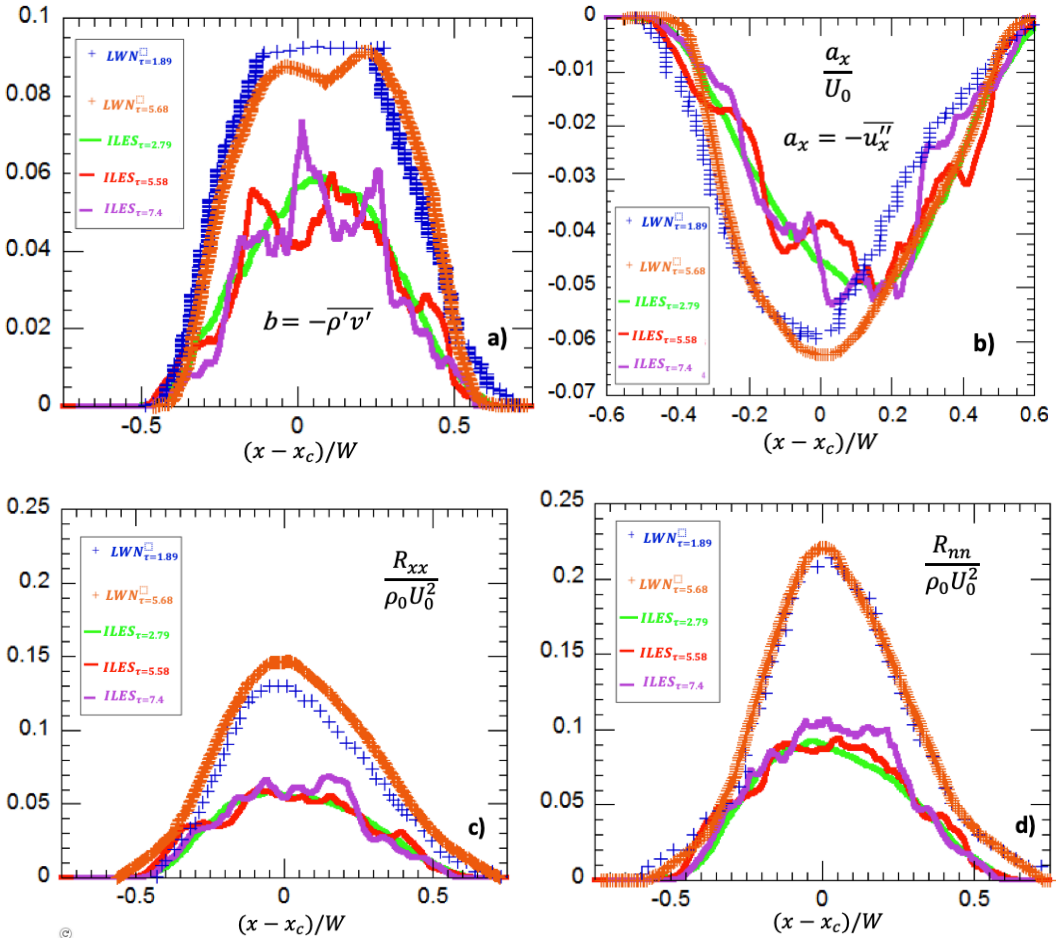

Figure 3. 5 Comparison of ILES simulation results (solid lines) from MOBILE with the LWN model of (SCH) [106, 107] at different non-dimensional times τ. x-coordinate is scaled by the time-dependent mix width $W(\tau)$ and centered at centerline x_c. Shown are (a) profiles of b, (b) profiles of a_x scaled by U_0, (c) profiles of R_{xx} scaled by $\rho_0 U_0^2$ and (d) profiles of R_{nn} scaled by $\rho_0 U_0^2$.

In figures 3.5 (a) - (d), we compare ILES results from MOBILE (solid lines) with two-point spectral model proposed by (SCH)[106, 107] at different non-dimensional times τ after the flow has achieved self-similarly. When scaled by the time-dependent mix-width, the ILES and model profiles collapse in the x-direction. Good agreement between the model

and simulation results for a_x is shown in Figure 3.5(b). However, the (scaled) turbulent stress R_{xx} and trace R_{nn} are overpredicted by the LWN model as observed in Figures 3.5 (c) and 3.5 (d). We believe these differences are due to the initial conditions employed in each calculation. MOBILE was initialized with a narrowband power spectrum, while the model computation reported in (SCH)[106, 107]used a broadband ~ k^{-2} power spectrum to initialize the calculations. Previous studies[125] have shown that RT mix growth is sensitive to the structure of the initial conditions, and that broadband perturbation spectra lead to a more aggressive growth of the mixing layer. Additional simulations in which the initial conditions are matched to those reported in [106, 107] will be reported in the future.

Next, we present a preliminary comparison of our ILES results with the modified LWN models derived from the two-point spectral model proposed by (SCH)[106, 107] discussed in section 1.2. The modified LWN model uses a non-local form for the turbulence frequency in the modeling of the cascade term (CS1995 and Sandoval[130]), and the employed calibration coefficients in the comparison are given below in table 3.1:

Table 3. 1 Table summarizing the calibration coefficients used in the calculation of the LWN model (SCH) [106, 107] .

C_{fb}	C_{bd}	C_{b1}	C_{b2}	C_{a1}	C_{a2}	C_{ad}	C_{r1}	C_{r2}	C_{rp1}	C_{rp2}	C_{rd}	C_{rpd}
0.5	0.03	0.12	0.06	0.12	0.06	0.03	0.12	0.06	0.08	0.08	0.03	0.03

In figure 3.6 (a)-(n), we compare results from MOBILE simulations with the LWN model. The model was initialized at $\tau = 1.89$, with data from the simulations at that time. This avoids integrating the model through the initial transition between the linear and

nonlinear stages of the flow. Several quantities are compared in figure 3.6, and show encouraging agreement between the model and the simulations. The LWN prediction of the evolution of the mixing layer width, according to figure 3.6 (a), is in excellent agreement with the simulation (MOBILE) results. We also compare the scaled mass flux in figures 3.6 (b)-(e), *b* in figures 3.6 (f)-(j), and the scaled kinetic energy in figures 3.6 (k)-(n). We find that while the LWN model prediction of these quantities are in excellent agreement with MOBILE's simulation results at early times, quickly , the model overpredicts a_x and R_{nn} as seen respectively in figures 3.6 (c)-(e) and in figures 3.6 (l)-(n). Meanwhile, the model's prediction for *b* remains excellent as seen in figures 3.6 (g)-(i) until late times when oscillations rise in the region around the edges of the TMZ as we can see in figure 3.6 (j). These oscillations are believed to be caused by high and sharp gradients in a_x.developing around the edges of the mixing layer as seen in figure 3.6 (e). High gradients in a_x can cause spikes in the equation of *b*, e.q (1.1.36), through the production term $\frac{\partial \bar{\rho} a_x}{\partial x}$; consequently destabilizing the numerical solution if the employed numerical scheme is not robust to sharp gradients.

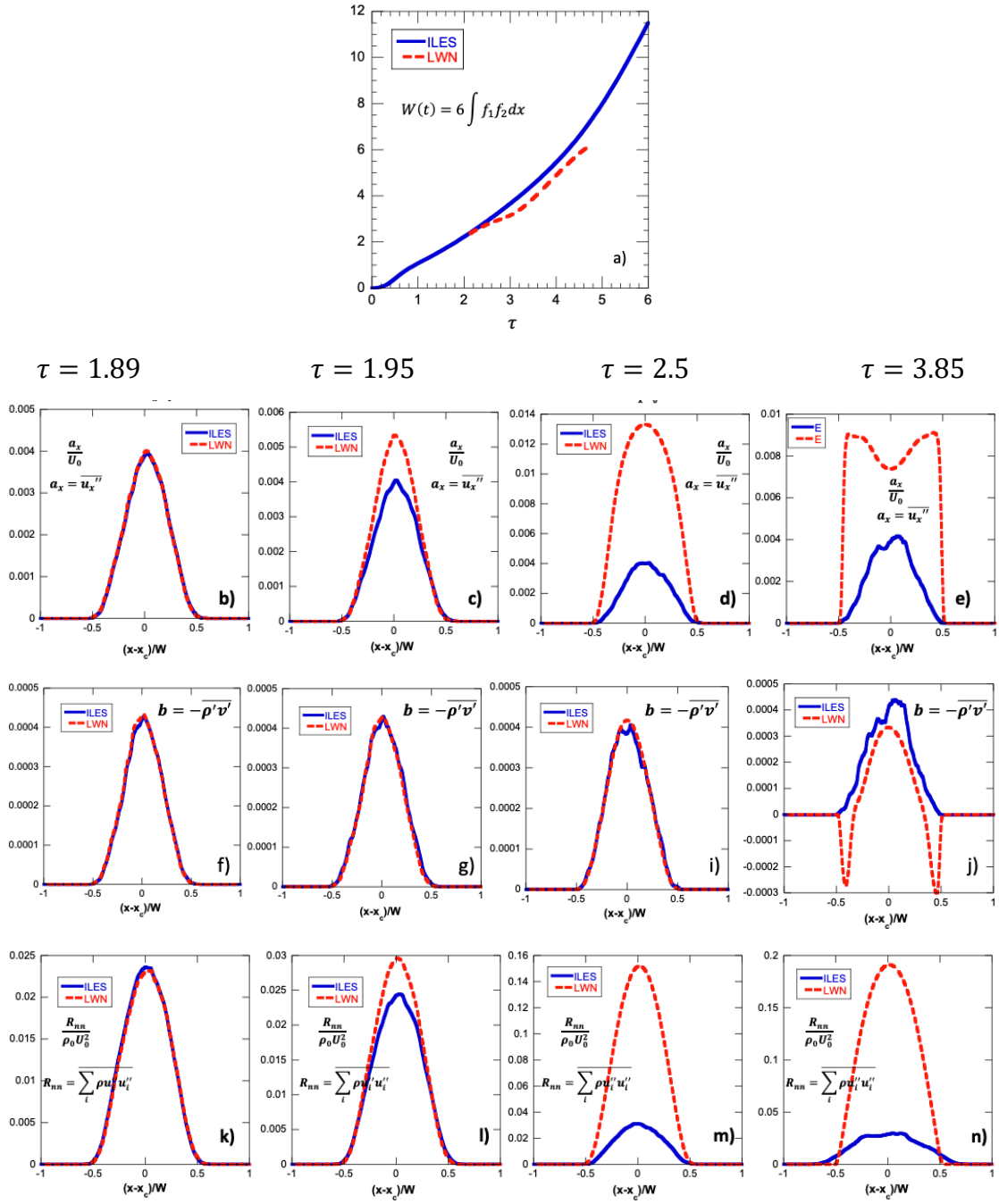

Figure 3. 6 Comparison of MOBILE simulation results with the LWN model initialized with simulation data at $\tau = 1.89$: (a) Time evolution of mixing layer width, (b)-(c) profiles of a_x scaled by U_0 at τ=[1.89, 1.95, 2.5,3.85], (f)-(i) profiles of b at τ=[1.89, 1.95, 2.5,3.85], and (j)-(m) profiles of R_{nn} scaled by $\rho_0 U_0^2$ at τ=[1.89, 1.95, 2.5,3.85]. x-coordinate is scaled by the time-dependent mix width $W(\tau)$ and centered at centerline x_c.

Next, the LWN model was initialized with corresponding simulation data at $\tau = 0$, and the production term in the b-equation ($\frac{(2\bar{\rho}-\rho_1-\rho_2)}{\rho_1\rho_2}\frac{\partial \bar{\rho} a_y}{\partial y}$) was neglected due to the negligible value of $(2\bar{\rho} - \rho_1 - \rho_2)$. An improvement is observed in the comparison of $W(\tau)$ as seen in figure 3.7 (a), also we note that the model is not able to capture the linear growth of the mixing layer width ($\tau < 1$). Further, an overall improvement in the prediction of scaled profiles of a_x, b, R_{nn} and R_{xx}, by the model are observed in figures 3.7 (c)-(f): Note the vanishing of the oscillations at late time in the LWN calculation of the profile of b in figure 3.7(c) even when the profile of a_x is sharp near the edges of the TMZ as seen in figure 3.7 (d); also note an improvement in the shape of the profiles of a_x in figure 3.7 (d) compared to its previous shape in figure 3.6(e).

In conclusion, preliminary comparisons with the LWN model for RT turbulence are encouraging, and include good agreement in quantities such as the mix width and the density-specific volume correlation. However, at late times, the LWN prediction of scaled mass flux and TKE are in disagreement with the simulations results.

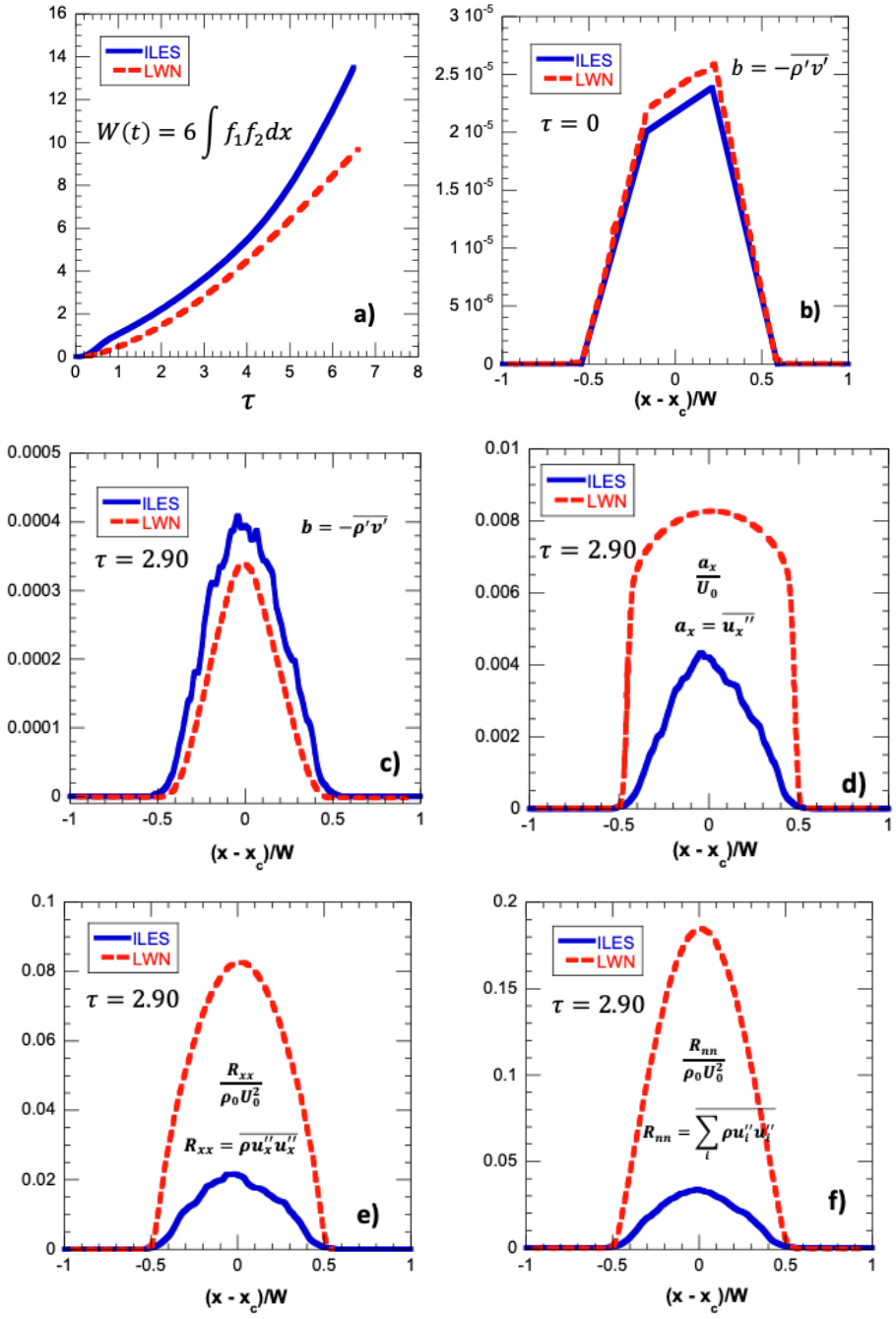

Figure 3. 7 Comparison of MOBILE simulation results with the LWN model initialized with simulation data at $\tau = 0$: (a) Time evolution of mixing layer width, (b) initial profiles of b, (c) late time (τ=2.9) profile of b, (d) late time profile of a_x scaled by U_0, (e) late time profiles of R_{xx} scaled by $\rho_0 U_0^2$, and (f) late time profiles of R_{nn} scaled by $\rho_0 U_0^2$. x-coordinate is scaled by the time-dependent mix width $W(\tau)$ and centered at centerline x_c.

CHAPTER 4 : DOUBLE-SHOCKED RICHTMYER-MESHKOV TURBULENCE

We describe results from numerical simulations of the turbulent Richtmyer-Meshkov instability subjected to successive shocks in the same direction. The single-shock RM driven turbulence has been previously studied in several theoretical, experimental and numerical[58, 115, 125, 131, 132] studies. Most recently, the so-called Theta group study [133] was a code-comparison effort involving multiple shock-physics codes to investigate the self-similar behavior of RM turbulence at late times. To allow for the flow to develop to a mature state of self-similarity, and to trigger the onset of self-similarity at earlier non-dimensional times, the initial conditions were comprised of short wavelength perturbations and referred as the quarter-scale problem in [133]. In a follow-up study[134], energy budgets were computed from simulation data to quantify the relative importance of terms in the transport equation, as well as terms arising from the compressibility of the flow such as the pressure-dilatation term.

The multiply-shocked RM problem is relevant to ICF implosions, where the interface between fuel and shell material is subjected to a cascade of shocks during both the implosion and post-stagnation stags. Similarly, in SCRAMJET applications, to satisfy the requirement of minimal residence times for the fuel jets, a shock train is used to repeatedly shock and achieve turbulation of the flow. Thus, we have extended the scope of these earlier studies [133] , to investigate the effect of multiple shocks originating in the heavier fluid, and their effect on the subsequent evolution of RM-driven turbulent mixing layer. Note that the double-shock configuration reported here is fundamentally different from the extensively studied reshock problem[135-143]in which the transmitted shock from the first

shock-interface interaction is reflected from an end wall, and allowed to impinge on the nonlinear mixing layer. In the current configuration (suggested by Mikaelian[144]), both shocks originate in the same fluid so that each interaction corresponds to a slow-fast ($A < 0$) shock-contact problem. Thus, following each shock-interface interaction, the negative RM growth rate will trigger an indirect phase inversion due to the negative Atwood number [132]. However, the precise nature of this transition is unclear for the following reason: If the second shock interaction occurs at early non-dimensional times (when individual modes are still linear in their amplitudes; with respect to their wavelengths), we can expect these modes to invert phase completely. In contrast, when the interaction occurs at a time such that the dominant modes have already become nonlinear, the phase reversal could be complicated by the presence of lagging structures which might lead to 'shredding' of the reversed bubble and spike structures. The simulations reported in this chapter are an attempt to clarify these issues. The details of the phase reversal and subsequent growth are of substantial interest to turbulence modelers seeking to develop low-order descriptions of mix development in ICF capsule implosions in which a series of timed shocks are used to maximize yield [48].

Our objective is to investigate the effect of the second shock arrival time on several turbulent flow features. By varying the time of second shock impact, we control the properties of the interface (composition of perturbation wavelengths and amplitudes) prior to this event. The simulations were all initialized with a perturbation front dominated by short wavelength signals, and obtained from the quarter-scale problem in the theta group study [133]. The second shock was initialized using the procedure described in § 4.1, while the second shock arrival time at the interface was systematically varied.

The problem configuration is shown in figures 4.1 (a) – (b), and depict the pre-shock and post-shock states respectively. The terminology describing the different regions in fig. 4.1 is adapted from [145], and can be generalized to multiple shocks. Figure 4.1a describes the flow configuration immediately before the arrival of an incident shock of strength M, and moving to the right with an incident shock speed (in the frame of the interface) of U_s. Region 3 refers to the state of the shocked material, while Regions 2^- and 1^- refer to the unshocked states associated with heavy and light fluids on either side of the perturbed interface. The superscripts '-' indicate pre-shocked states, while '+' refer to fluid states immediately following the passage of the shock. Similarly, '--' and '++' indicate the corresponding states preceding and following the passage of the second shock in the same direction. The fluid states and velocities following shock passage are shown in Figure 4.1b in the laboratory frame of reference. The interface acquires a jump velocity dU from the shock interaction, while the incident shock has split in to transmitted and reflected waves with velocities of U_t and U_r respectively.

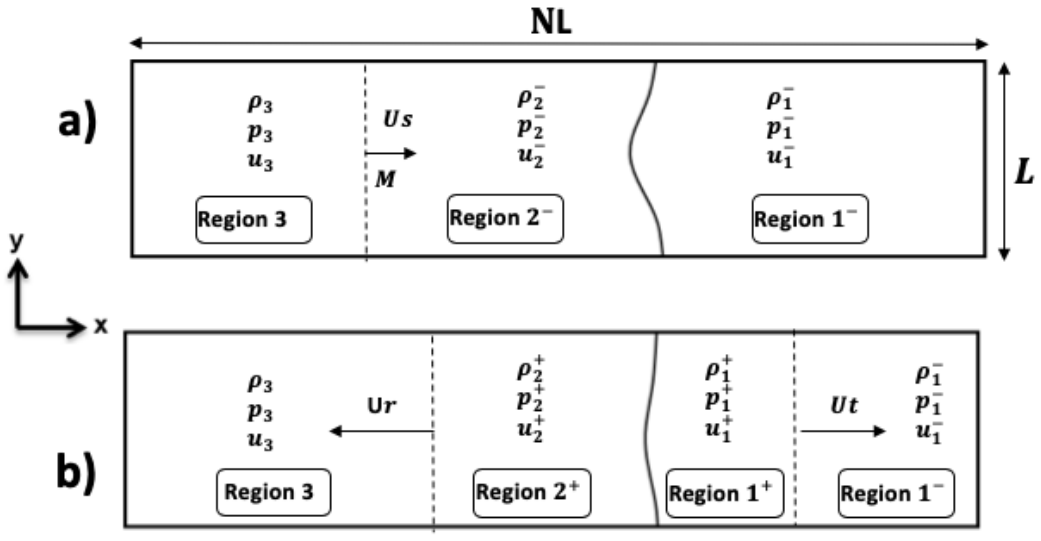

Figure 4. 1 Schematic of the initial flow configuration. Problem terminology adapted from Mikaelian[145]. (a) Pre-shock flow configuration, (b) post-shock flow configuration.

We briefly describe the notation employed in this chapter to describe flow behavior following each shock. Pre- and post-shocked states are denoted by superscripts '-' and '+' respectively. Subscripts can refer to the initial state '0', or the region of the flow. Thus, p_2^- refers to the pressure in region '2' before the first shock, while $\dot{W}_0^{++}$ refers to the initial growth rate of the mixing layer following the second shock. We non-dimensionalize time using

$$\tau = t\dot{W}_0 \backslash \bar{\lambda} \tag{4.1}$$

where $\dot{W}_0 \approx 1264.9\ cm/s$ (for conditions of the theta group problem) is the predicted initial growth rate of the mixing layer width after the first shock, t is the time in seconds, and $\bar{\lambda} = 2\pi/\bar{k}$. The averaged wavenumber $\bar{k}$ is associated with the initial quarter-scale perturbation (detailed in § 4.1 below) and given by

$$\bar{k} = \sqrt{7/12}k_{max} \tag{4.2}$$

In eq. (4.2), the maximum wave number is given by $k_{max} = 2\pi/\lambda_{min}$ with $\lambda_{min} = L/32$ for the initial conditions in Thornber[133] , and L is the width of the shock tube cross section.

4.1 **Problem Description and Numerical Setup**

We report results from three simulations (cases 1 – 3), summarized in table 4.1 corresponding to different instances of second shock arrival ($\tau_2 = 1, 3, and\ 6$ respectively). The simulations were performed using the FLASH code (details in Chapter 2), and initialized with fluids with densities $\rho_2^- = 0.003\ g/cm^3$ and $\rho_1^- = 0.001\ g/cm^3$ (see figure 4.1), resulting in an initial Atwood number $A = -0.5$. The initial pressure was chosen to be $p_2^- = p_1^- = 100\ kPa$, while the compressibility of both fluids was taken as $\gamma_2^- = \gamma_1^- = 5/3$ (to match the problem parameters from the theta group study [133]. The

initial incident shock S_1 was of strength M_1 = 1.83, while the second shock S_2 was initialized with M_2 = 1.5 and reached the interface at non-dimensional times of τ_2 = [1, 3, and 6]. The simulations were performed with a Cartesian mesh of 256 zones/ L, where $L = 2\pi$ is the domain cross-sectional length.

Table 4. 1 Summary of second shock simulations.

	Second shock Mach number M_2	Time of Second shock τ_2
Case 1	1.5	1
Case 2	1.5	3
Case 3	1.5	6

4.2 **Results and Discussion**

4.2.1 Unperturbed, 1D Simulations

Figure 4.2 is an x-t diagram showing significant events from one of our simulations, in which the second shock arrived at the interface at $\tau_2 = 6$. The initial interface is given a negative velocity $-U_0$ computed by requiring the final (post-second shock) interface velocity should be zero. Following the interaction with the first shock, the interface velocity (in the fixed frame of reference) was $U_1 = -22855.6\ cm/s$. Once the reflected rarefaction from the first shock exited the outflow boundary at x = 0, the guard cells were filled with material corresponding to the second shock. The second shock was then 'released' at a time such that it would reach the moving interface at $\tau_2 = 6$, as required for this case. From the

calculations presented in chapter A.4.1.3, this results in a stationary interface following the second shock interaction.

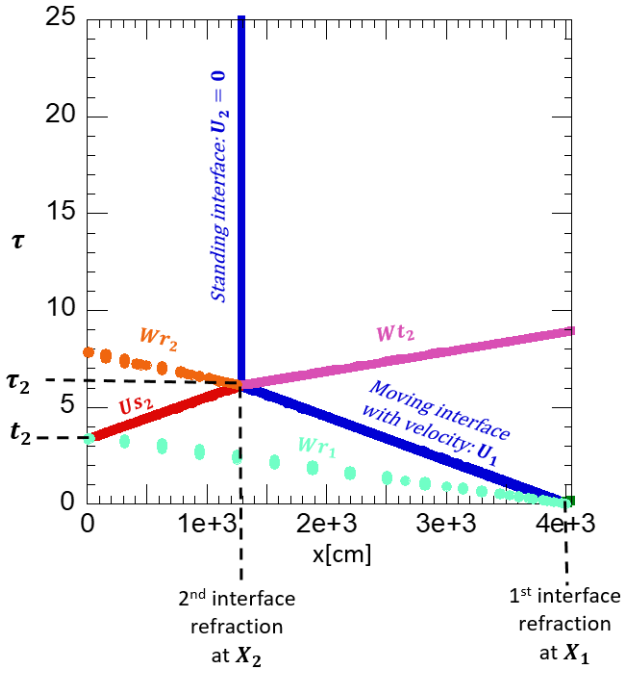

Figure 4. 2 x-t diagram showing the trajectory of the interface (blue), transmitted (pink) and reflected waves (light green and orange) following 1st (not shown) and 2nd (red) shocks for case 3 ($\tau_2 = 6$).

4.2.2 Multimode, 3D Simulations

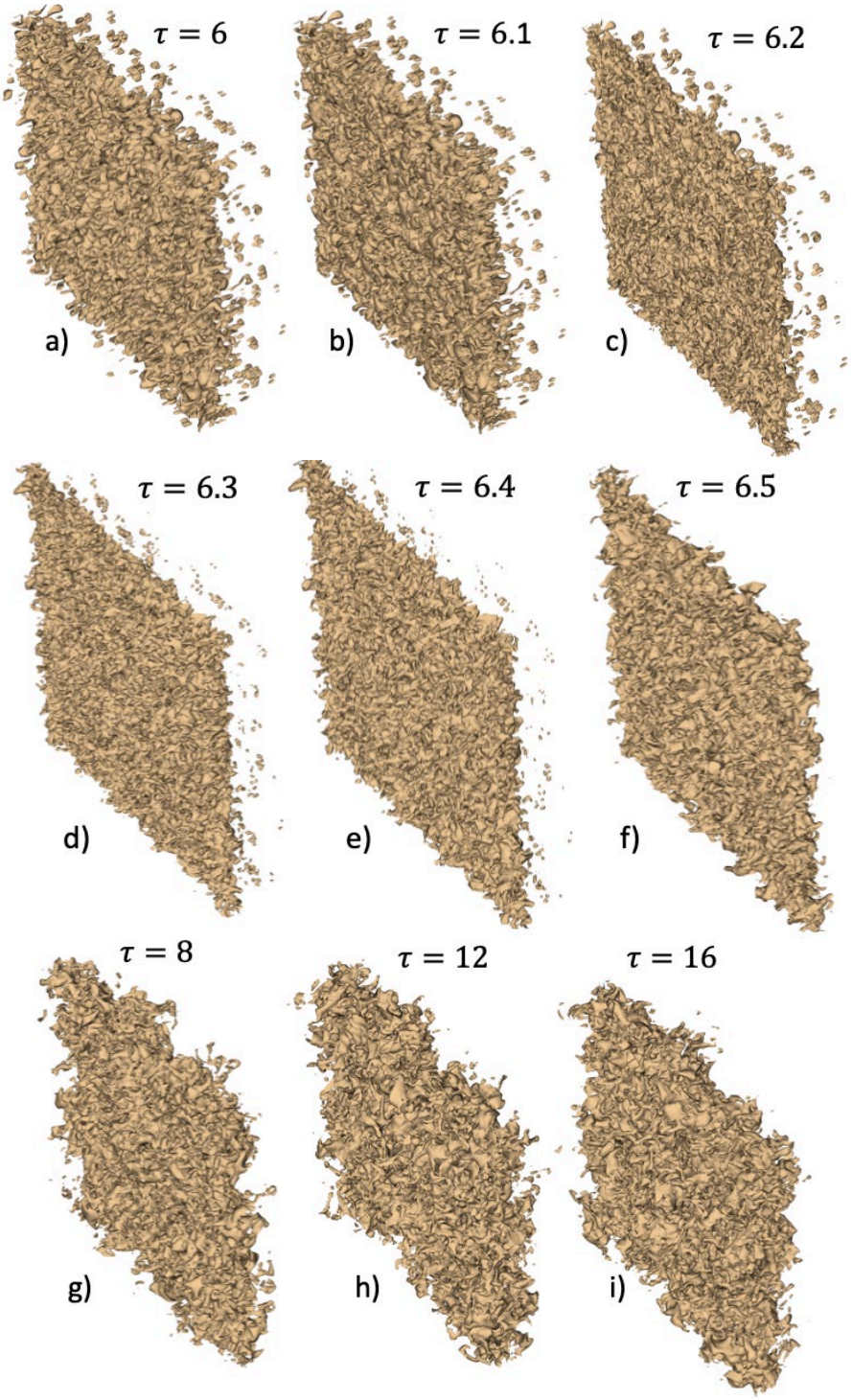

Figure 4.3 Isosurfaces of 50% mass fraction of the heavy fluid showing (a) - (c) the compression of the mixing layer by the 2nd, followed by (d) - (f) phase reversal sand by (g) - (i) late time regrowth .

The evolution of the mixing layer from case 3 is tracked in figure 4.3 (a) – (i) using isosurfaces of the 50% mass fraction of the heavy fluid. The compression of the mixing layer induced by the second shock is visible through figures 4.3 (a) - (c), where the thickness of the mixing layer reduces sharply in response to compression ($6 < \tau \leq 6.2$). Bubbles and spikes appear to undergo phase reversal in figures 4.3 (d) – (f) ($6.2 < \tau \leq 6.5$), although this process is complicated by the high mixing caused by "shredding" of the non-linear structures (see figure 4.6 below and corresponding discussion). At late times (figures 4.3 (g)-(i)), the mixing layer appears to grow to a self-similar state, leading eventually to increased mixing between the fluids.

In figure. 4.6, we provide a closer look at the partial phase reversal observed during the passage of the second shock by plotting contours of the density field before, during and immediately following shock passage for case 1. We focus our attention on two bubble/spike pairs identified by the green and white circles. The bubble/spike pair 'A' is still at a linear stage of evolution at the time of arrival of the second shock, while the pair labelled 'B' appeared to have entered nonlinear saturation. This difference in the maturity of the structures produces very different outcomes associated with the shock passage. Bubbles and spikes associated with 'A' appear to undergo a complete phase reversal. In contrast, leading structures in 'B' initially reverse direction, but are then shredded by lagging structures in their wake, preventing a complete phase reversal. This process of shredding is accompanied by a significant increase in the appearance of small-scale structures, and in the corresponding atomic mix fraction (discussed below). The dynamics are similar to the observations in accel-decel-accel problems studied in [115], where the onset of deceleration resulted in (i) an initial phase reversal of leading structures, (ii) 'shredding'

of dominant bubbles and spikes as the reversed structures encounter lagging features in the flow and (iii) an accompanying increase in mixing parameters. With increasing τ_2, we expect increased shredding and atomic mixing as the highly nonlinear state of the flow implies a wider hierarchy of leading/lagging structures within the bubble/spike fronts. Finally, note that in this heavy-to-light interaction, bubbles encounter a nearly planar incident shock, while the shock is likely distorted by the mixing layer before reaching the spike structures. This could result in a weaker shock impacting the spike structures resulting in a partial phase reversal and slower growth rate.

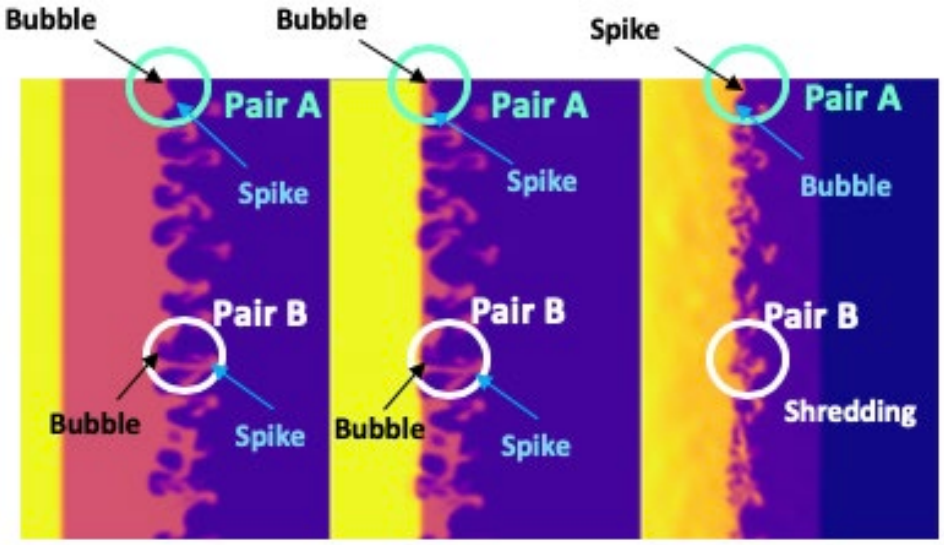

Figure 4. 4 Density contours (a) before (b) during and (c) after the passage of the second shock for case 1 (τ_2=1)

Based on these qualitative observations, we list the following preliminary conclusions: (i) Individual structures appear to undergo phase reversal, but this process depends extensively on the state of the structures prior to shock interaction (ii) Structures that have evolved to nonlinearity, are less likely to survive the phase reversal process and instead are

'shredded' by lagging structures which the reversed bubbles/spikes encounter. This process is similar to the shredding of leading bubbles and spikes observed in the accel-decel-accel (RT) problem [115] . (iii) The shredding leads to the breakup of large-scale structures in to smaller-scale features, with a corresponding increase in atomic mixing, while the mass transport across the mixing layer is decreased. In addition to this partial phase reversal, the mixing layer is also compressed by the shock. This results in an initial reduction in the mixing layer width, and associated densification which might partially stabilize the mixing layer[146]. Thus, these dynamic processes represent a complex set of phenomena occurring simultaneously, which will be investigated in greater detail in subsequent studies. For the purposes of the analysis presented here, we take the mix width (or amplitude) at the end of the compression/phase reversal process as the initial amplitude that seeds the subsequent growth.

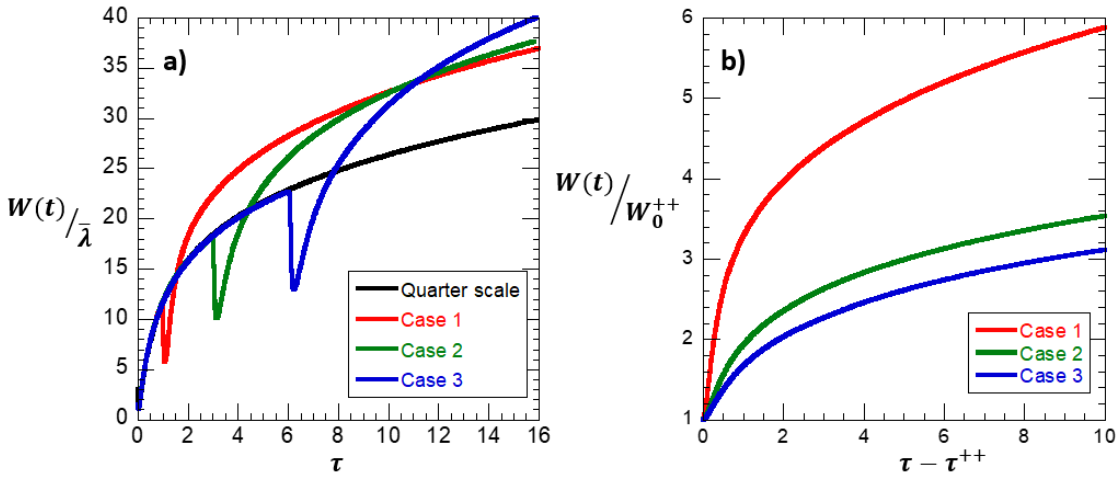

Figure 4. 5: (a) Comparison of the evolution of the scaled turbulent mixing layer width plotted against the non-dimensional time τ for cases 1 – 3 along with the benchmark theta group result from Thornber[133]. (b) Evolution of the non-dimensional mixing layer widths scaled by the post-second shock amplitude $W_0^{++} = W(\tau^{++})$ plotted against the local scaled time $\tau - \tau^{++}$.

The evolution of the mix width ($W(t) = \int_0^{L_x} \langle f_1 \rangle \langle f_2 \rangle dx$) from FLASH simulations of cases 1 – 3 are compared with results from the theta-group study (quarter-scale problem) which is included here as a benchmark in figure 4.5(a). The mixing layer width is scaled by $\bar{\lambda}$, and plotted against the non-dimensional time τ as defined earlier. Following the second shock, the turbulent mixing zones (TMZ) experience an amplitude compression, followed by rapid growth culminating in an asymptotic self-similar stage. For cases 1-3, the simulations report a compression of the mixing layer width of ${W_0}^{++}/{W_0}^{--}$ = 0.45, 0.53, and 0.53 respectively. These values are close to the expected value of Richtmyer's compression factor[12, 132] based on incident shock and interface velocities of $\chi \equiv 1 - \frac{dU}{W_0^{--}} = 0.49$, although this process appears to be complicated by a partial phase reversal process as discussed earlier.

When scaled by the post-second shock amplitudes ${W_0}^{++} = W(\tau^{++})$, and plotted against the origin-shifted non-dimensional time $\tau - \tau^{++}$, the mixing widths from cases (1 – 3) in figure 4.5(b) appear to be nearly parallel at late times. The initial post-shock growth rates appear to depend on the modal content of the interface at the time of the second shock. For simulations in which the second shock was delayed, the perturbation front is likely dominated by larger structures (i.e. $\bar{\lambda}_3 > \bar{\lambda}_1$ *and* $\bar{k}_3 < \bar{k}_1$) leading to a relatively slower linear growth rate for case 3 compared with case 1 and consistent with the Meyer-Blewett[147] formula:

$$\frac{W(t)}{{W_0}^{++}} \sim 1 + \bar{k} A^{++} \Delta U (t - t^{++}). \tag{4.3}$$

The scaled mix widths in figure 4.5 (b) appear to satisfy eq. (4.3) over a time τ_{NL}, after which a transition to self-similar ($\sim \tau^{\theta}$) behavior is observed. The RM dependence on

initial conditions manifests in the initial linear growth rate and the turnover time, while the late-time curves in figure 4.5(b) are nearly parallel (the linear stage is thus directly influenced by the applied drive, while the late-stage decaying behavior can be treated as a return to isotropy in the absence of the drive [146]).

These observations are confirmed in figure 4.6, where we plot the self-similar growth exponent θ computed from the mix width using[146] $\theta^{-1} = 1 - \ddot{W}W/\dot{W}^2$ from cases 1 – 3 and the θ-group test problem. The large spikes in each case are due to shock compression, and correspond to the arrival times of the second shock. Following the transients (due to the initial linear growth discussed above), θ saturates to a universal late time value of ~ 0.25 regardless of the initial conditions present at the time of the second shock. While more detailed investigations of initial condition effects are currently under way, these second shock simulations suggest initial conditions significantly influence the linear growth regime and the nonlinear transition time, but not the late-time asymptotic behavior.

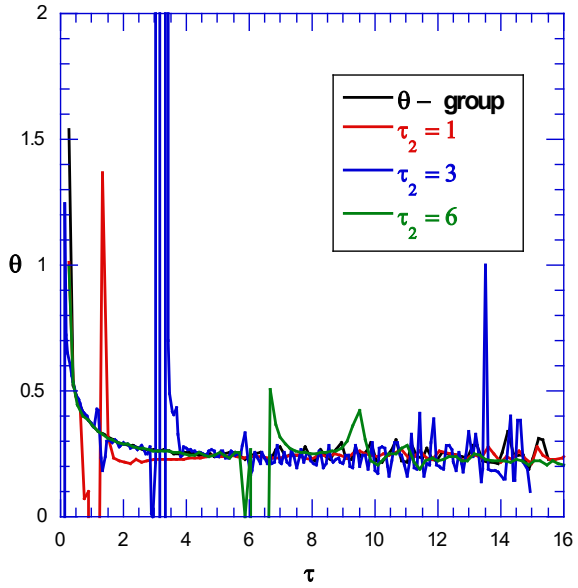

Figure 4. 6 The time-dependent RM growth exponent θ from cases 1 – 3 and the benchmark θ-group case [133].

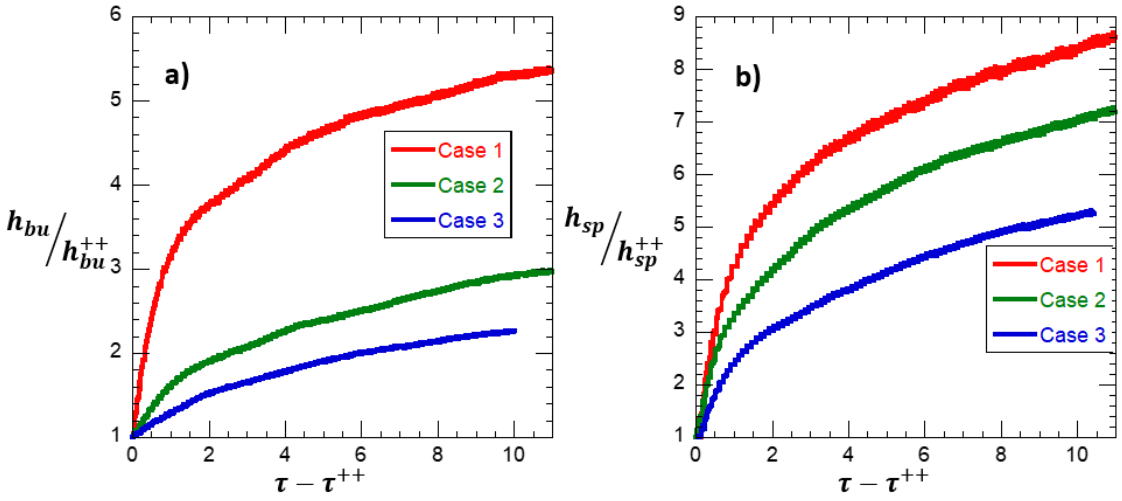

Figure 4. 7 (a) Comparison in origin-shifted non-dimensional time (τ - τ^{++}) of (a) the bubble amplitudes scaled by $h_{bu}{}^{++}$ and (b) spike amplitudes scaled by $h_{sp}{}^{++}$, for cases 1-3.

We compare the bubble and spike amplitude evolution for cases 1 - 3 respectively in fig. 4.7 (a) and fig 4.7 (b). The bubble and spike amplitudes are defined from our simulations using $h_{bu} = \left|x|_{\langle f_1\rangle=1\%} - x|_{\langle f_1\rangle=50\%}\right|$ and $h_{sp} = \left|x|_{\langle f_1\rangle=99\%} - x|_{\langle f_1\rangle=50\%}\right|$ where $\langle\cdot\rangle$ denote planar averages in the directions perpendicular to shock traverse (both quantities are then scaled by the corresponding amplitudes at the end of the shock compression). Note that these planar-averaged definitions of bubble and spike amplitudes are insensitive to phase reversals by individual bubble and spike structures if they occur. Hence, while individual bubbles and spikes might undergo an indirect phase reversal, this does not cause the amplitudes based on planar-averaged quantities to 'zero-out' in fig. 4.7 (a)-(b). The results are similar to the mix width behavior discussed earlier, while spike growth outpaces bubbles as expected at this Atwood number.

In fig. 4.8 (a) – (b), we plot the development of the streamwise ($a_x = -\overline{u_x''}$) and spanwise ($a_z = -\overline{u_z''}$) mass fluxes evaluated at the mid-plane of the mixing layer ($x|_{\langle f\rangle=0.5}$). Fig. 4.8

(a) shows an initial spike in the streamwise mass flux due to the shock-compression and phase reversal process. Thus, the largest increase is observed for case 1 ($\tau_2 = 1$), in which a nearly complete phase reversal is expected for bubbles and spikes. In contrast, case 3 ($\tau_2 = 6$) shows the smallest increase in the initial streamwise flux, since the compression and phase reversal process is interrupted by shredding as discussed above. Following the passage of the shock, the net streamwise mass flux shows an asymptotic decay for cases 1 – 3, as expected for a decaying flow. At late times, the streamwise mass flux appears to saturate to a positive asymptotic limit, suggesting a net mass flux across the mixing layer in favor of the spikes in this heavy-to-light flow. This is consistent with observations and models of the single-mode RMI [148], in which the ratio of the nonlinear spike velocity to the corresponding bubble velocity increased with the Atwood number.

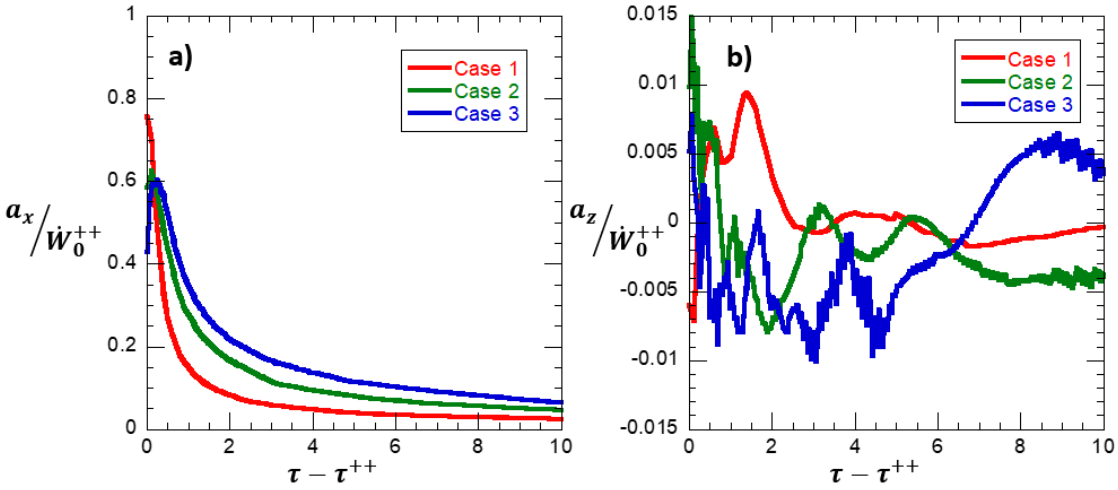

Figure 4. 8 Time evolution of the centerline (a) streamwise mass flux a_x scaled by $\dot{w}_0{}^{++}$ and (b) spanwise mass flux $a_z = -\overline{u_z''}$ scaled by $\dot{w}_0{}^{++}$, in local scaled time (τ - τ^{++}).

Figure 4.8 (b) shows (as expected) that there is no net spanwise mass flux at late stages in the flow. However, the decay to this state appears to be modulated by acoustic waves with

a time period that increases with τ_2 and the wavelength of the dominant structures at the time of the second shock impact. We believe these modulations are linked to acoustic waves generated by the passage of the distorted shock wave through the mixing layer. The initially planar shock is distorted through its interaction with the bubble front. As the distorted shock passes through the mixing layer, it is likely refracted by the lagging structures and density gradients leading to locally generated transmitted and reflected waves. The reflected rarefactions travel at an angle to the streamwise direction and are further reflected or weakened by other structures within the mixing layer. Eventually, these acoustic waves decay over a timescale that is proportional to $\frac{\bar{\lambda}(\tau_2)}{\Delta U}$, where $\bar{\lambda}(\tau_2)$ is the wavelength of the dominant structure at the time of the second shock.

Cross-stream profiles of the streamwise mass flux a_x are plotted in figure 4.9, where they have been scaled by the RM initial growth rate immediately following the second shock event. By scaling the coordinate according to $\frac{x-x|_{\langle f\rangle=0.5}}{W(t)}$, we find the profiles obtained at different times appear to collapse suggesting a self-similar behavior at late times. Additionally, the profiles are skewed towards the bubble side, since bubbles transport more mass in variable density flows, an effect that is likely to increase with the Atwood number.

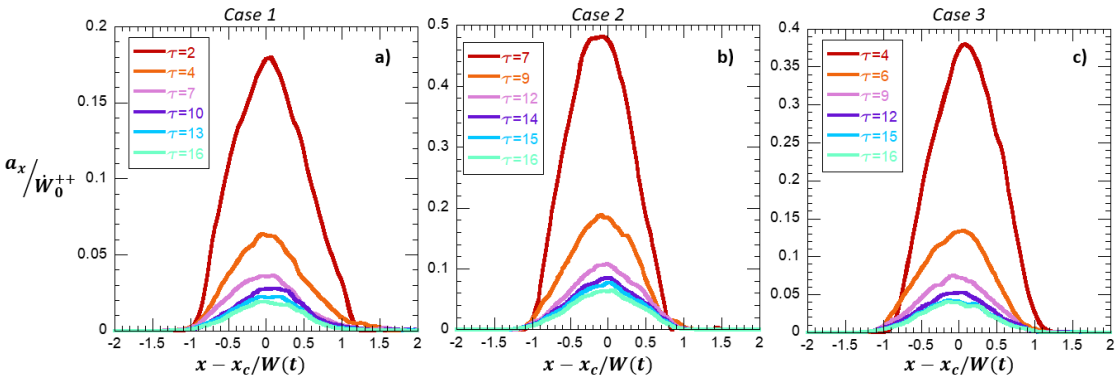

Figure 4. 9 Cross-stream profiles of the streamwise mass flux a_x for (a) cases 1, (b) case 2, and (c) case 3, at different non-dimensional times. x-coordinate is scaled by the time-dependent mix width $W(\tau)$ and centered at TMZ centerline x_c.

Cross-stream profiles of the density-specific volume correlation ($b = -\overline{\rho' v'}$) are plotted against the scaled coordinate $\frac{x - x|_{\langle f \rangle = 0.5}}{W(t)}$ for cases 1 – 3 in figure 4.10. As the flow evolves to a self-similar state, b-profiles at different times collapse to a single functional form, while the peak values observed in all three cases are in agreement. The time evolution of b is plotted for cases 1 – 3 in fig. 4.11 and shows a decay to a near-constant value at late times.

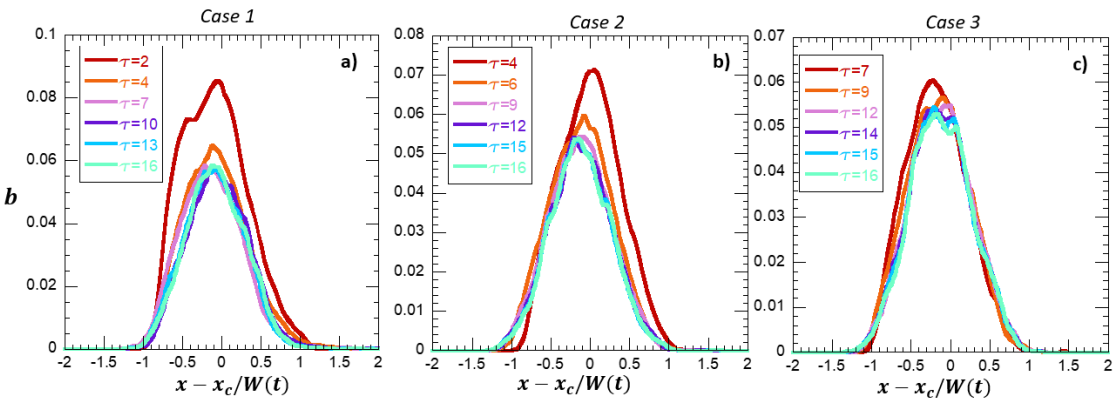

Figure 4. 10 Cross-stream profiles of the density-specific volume self-correlation b for (a) cases 1, (b) case 2, and (c) case 3 at different non-dimensional times. x-coordinate is scaled by the time-dependent mix width $W(\tau)$ and centered at TMZ centerline x_c.

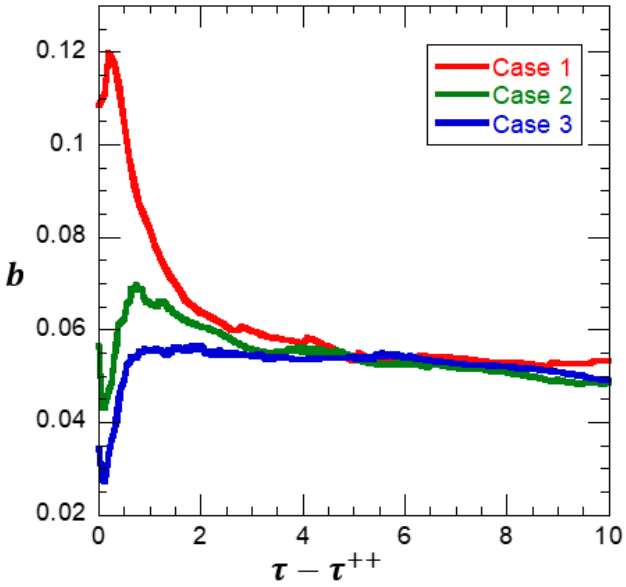

Figure 4. 11 Time evolution of TMZ centerline planar average of the density-specific volume self-correlation b for cases 1 – 3, in local scaled time (τ - τ^{++}).

In figure 4.12, we plot the development in time of the atomic mix fraction, Θ defined by

$$\Theta = \frac{\int \langle f_1 f_2 \rangle dx}{\int \langle f_1 \rangle \langle f_2 \rangle dx} \tag{4.4}$$

where f_1 and f_2 are the volume fraction of the light and heavy fluids respectively. The initial spike in Θ is associated with shock compression, and the breakup of larger structures

due to shredding leading to atomization and enhanced local mixing. This is followed by a short-lived drop in the value of Θ, likely due to the 'de-mixing' occurring as the homogenized mixing layer from compression and phase reversal begins to grow sorting in to newly formed bubbles and spikes. However, at late times the atomic mix fraction from the three cases asymptote to a constant value approaching ~ 0.8 consistent with reported values from single-shock RM studies [133] . Thus, figures 4.10 – 4.12 suggest that in all the simulations, following initial transients associated with the shock compression, there is a return to self-similarity at late times. This is evident in asymptotic values of the atomic mix, scaled mass flux and the density-specific volume correlations.

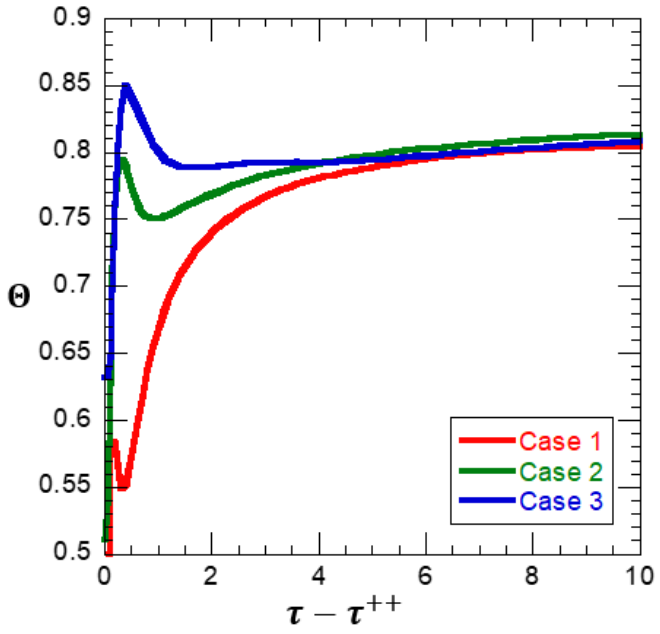

Figure 4. 12 Time evolution of TMZ centerline atomic mix fraction Θ for cases 1 – 3 in local scaled time (τ - τ^{++}).

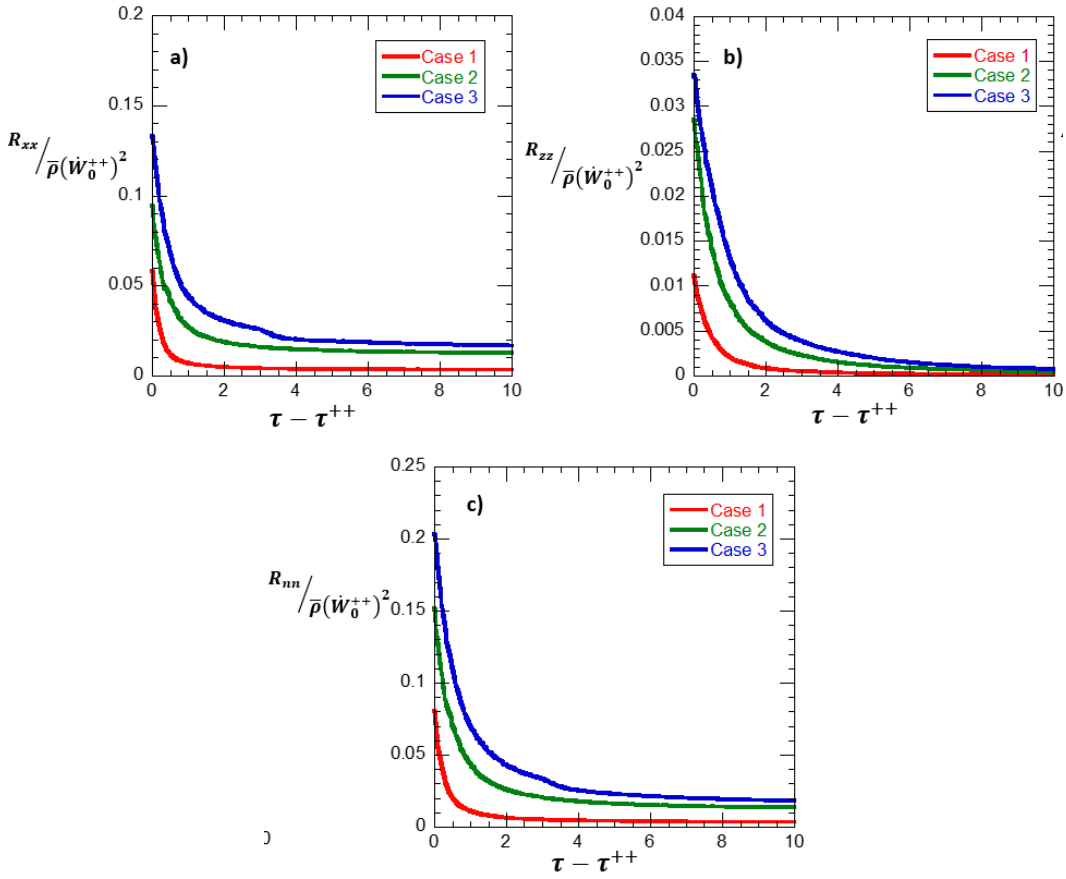

Figure 4. 13 Evolution of TMZ centerline averages of (a) TKE streamwise component R_{xx}, (b) TKE cross-stream component R_{zz}, and (c) total TKE R_{nn}, for cases 1-3. Plots are scaled by the squared growth of the mixing layer measured at τ^{++} ($\dot{W}_0^{++}$) and in local scaled time (τ - τ^{++}).

In figures 4.13 (a)-(c), we plot the development in time of the streamwise (R_{xx}) and the spanwise (R_{zz}) Reynolds stress components and the total TKE computed at the center of the mixing layer and with appropriate non-dimensionalization. Following the second shock, R_{xx}, R_{zz}, and R_{nn} are observed to rapidly decay at a rate inversely proportional to τ_2. The self-similar regime at late time is observed by the asymptotic collapse in R_{xx}, R_{zz}, and R_{nn} for all three cases. The inhomogeneity in the flow is also persistent, as indicated by R_{xx} being an order of magnitude larger than R_{zz} for all the double-shock cases. Cross-

stream profiles of R_{nn} at different times are plotted in figures 4.14 (a)-(c) below. While the collapse of the scaled profiles at late times suggests the flow reaching a self-similar regime, the inhomogeneity in the flow is also visible and indicated by higher values of R_{nn} at the left (heavy side) of the TMZ.

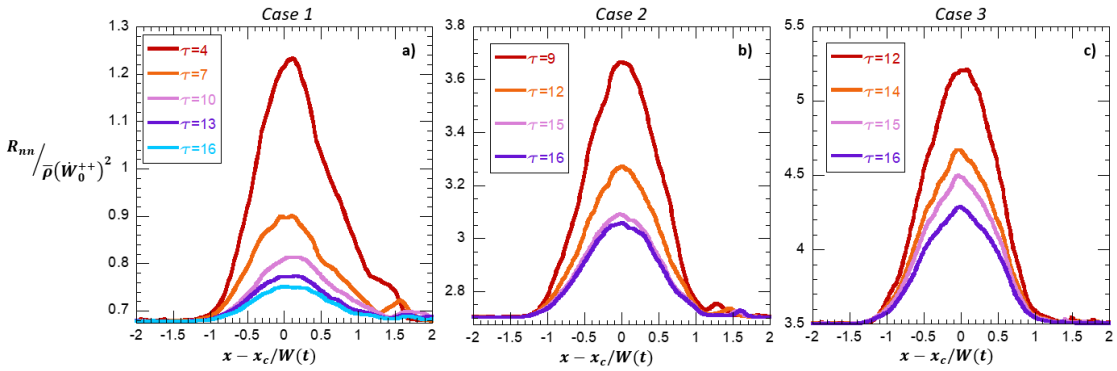

Figure 4. 14 Profiles of the total TKE scaled by $(\dot{W}_0^{++})^2$ for (a) cases 1, (b) case 2 and (c) case 3, at different non-dimensional times. x-coordinate is scaled by the time-dependent mix width $W(\tau)$ and centered at TMZ centerline x_c.

4.3 **Summary and Conclusions**

The behavior of twice-shocked RM mixing layer was studied using high resolution numerical simulations. The problem configuration is fundamentally different from several reshock studies, in which the second shock event is associated with a reflected shock from the endwall. In the current configuration, both shocks travel in the same direction and is thus relevant to recent interest in high energy density experiments in which timed shocks were used to manipulate the mixing and the neutron yield.

Since both shocks traverse the interface in a heavy-to-light interaction, a complex sequence of events unfolds particularly if the interface is already nonlinear. This occurs when the second shock is released much later in time, so that the bubbles and spikes have been

allowed to develop to nonlinear amplitudes. In such cases, leading structures at the bubble/spike front appear to initially reverse direction but the phase reversal is interrupted by collision with slower, lagging structures. The phenomena is not unlike bubble shredding previously observed in accel-decel-accel studies [115] of the Rayleigh-Taylor flow.

The variation in second shock times can be treated as an initial condition problem, in which the spectral content of the interface skews towards longer wavelengths/larger amplitudes as the time of second shock is increased. Accordingly, the initial linear growth rate and the nonlinear transition time are dependent on τ_2, but the late time mix widths are parallel for all the cases. This late-time universal behavior can also be extracted by plotting the power law exponent θ which asymptotes to ~ 0.25 for all the cases regardless of the value of τ_2. The nonlinear transition time may be interpreted as the time at which the flow recovers from the initial conditions and reverts to an asymptotic behavior. Several quantities of interest to turbulence modelers were also presented, including turbulent mass fluxes (in the shock- and lateral directions), density-specific volume self-correlation, Reynolds stresses and turbulent kinetic energy.

CHAPTER 5 : RICHTMYER-MESHKOV TURBULENCE IN A SPHERICALLY CONVERGENT GEOMETRY

An interface separating two distinct fluids is susceptible to the Richtmyer-Meshkov [12, 13] (RM) Instability, when an impulsive acceleration is applied. The instance of a planar interface accelerated by a planar shock has been investigated extensively in the literature through theory, experiments and numerical simulations (see [149] for detailed summary and references). The evolution of the single-mode RM has also been treated theoretically [53, 57, 58, 149] and through numerical simulations [58, 59, 150] in cylindrical and spherical geometries. However, a detailed description of the corresponding turbulent mixing layer growth confined by a spherically convergent geometry has not been treated exhaustively due to challenges in computationally resolving the turbulent mix or in experimentally diagnosing a convergent mixing layer. Through detailed simulations using an ALE code, Youngs et al. [14] investigated a turbulent mixing layer initialized by random perturbations, and driven by a time-varying implosion history. The same implosion history was employed in a comparative study[54] of several codes (and numerical methods), which concluded that when convergence effects are significant, an aligned numerical grid is critical to preventing the appearance of spurious, grid-generated, numerical modes in the simulation. Lombardini and Pullin [55, 56] performed 3D Large Eddy Simulations of turbulent RM accelerated by a self-similar Chisnell [151] shock wave. In this chapter, we report on results from numerical simulations of a spherically convergent, turbulent mixing layer energized through the RM instability from a Chisnell-type[60, 151] convergent shock. The 3D simulations were performed using the FLASH [109] code, in spherical coordinates that are

always in alignment with the mixing layer and the shock, while the use of Adaptive Mesh Refinement (AMR) ensures local mesh volumes scale with the sharpest features of the flow. In addition to qualitative results, we describe the evolution of mean quantities associated with RM turbulence in a convergent geometry.

5.1 **Numerical Details and Problem Definition**

The problem configuration is depicted schematically in figure 5.1, which shows a spherical wedge defined by $\frac{\pi}{2}-\frac{\pi}{5} \leq (\theta,\phi) \leq \frac{\pi}{2}+\frac{\pi}{5}$, and extending to r = 20 cm in the radial direction. The interface between the two gases is situated at r = 15 cm, while the spherical shock originates at r = 15.2 cm in the heavy gas (Air, r ≥ 15 cm). As the shock crosses the interface, a transmitted shock is generated in the lighter gas (He, r < 15 cm), while a reflected rarefaction is returned in the heavy fluid. Outflow boundary conditions at r = 20 cm ensure the rarefaction (and any other acoustic waves) exit the boundary without spurious reflections. Periodic boundary conditions are enforced on the lateral boundaries, while the origin is modeled as a reflecting surface at r = dr (so that the singularity at r = 0 is excluded from our computational domain). The flow properties on either side of the initial shock are computed using Rankine-Hugoniot relations found in [145], while the shocked region is described using the self-similar solution of Chisnell [151] given in Figure 5.2. We track all other shocks and rarefaction waves subsequently generated in the flow through a shock detection algorithm.

The interface in the 3D simulations was initialized with a multimode perturbation, along the lines of the alpha-group[47] collaboration, with energetic modes confined to $20 \leq (m_\theta, m_\phi) \leq 40$. We randomize the initial amplitudes and phases with a Gaussian distribution, thereby ensuring the initial perturbation surface is devoid of concentrated peaks and

valleys. The choice of an initial perturbation concentrated in the high mode numbers, also minimizes the impact of Bell-Plesset effects in our simulation [15, 16], so that the growth is largely due to the baroclinic instability. The RMS amplitude of the initial perturbation was chosen to be 0.005 cm, corresponding to ~ 0.03 % of R_0. The surface perturbations within a cell volume are converted to corresponding perturbations of the mass fraction Y of air and He. For this preliminary study, a resolution of 256 zones was used in each angular direction of the (θ,ϕ) and 1024 zones in the radial direction.

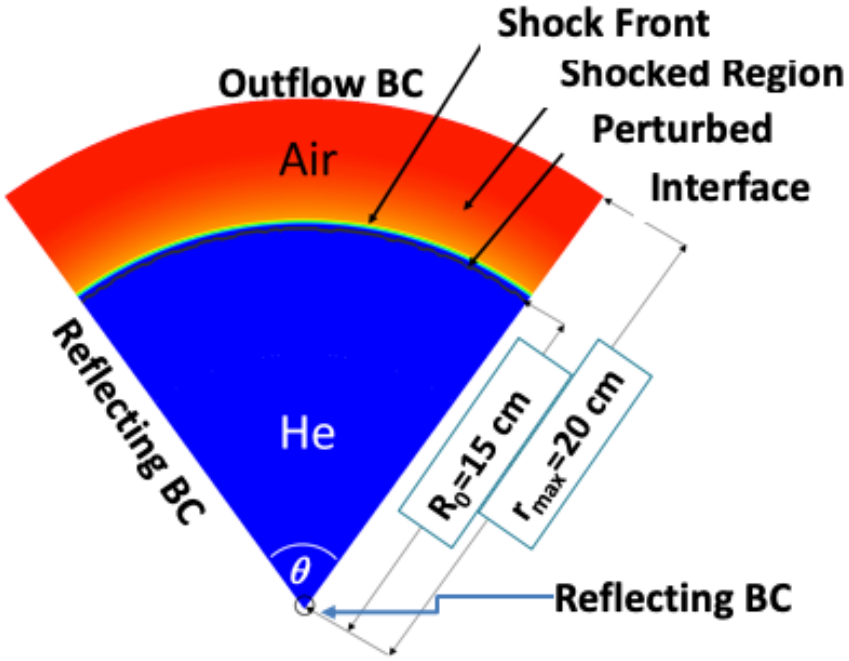

Figure 5. 1 Schematic of the problem setup.

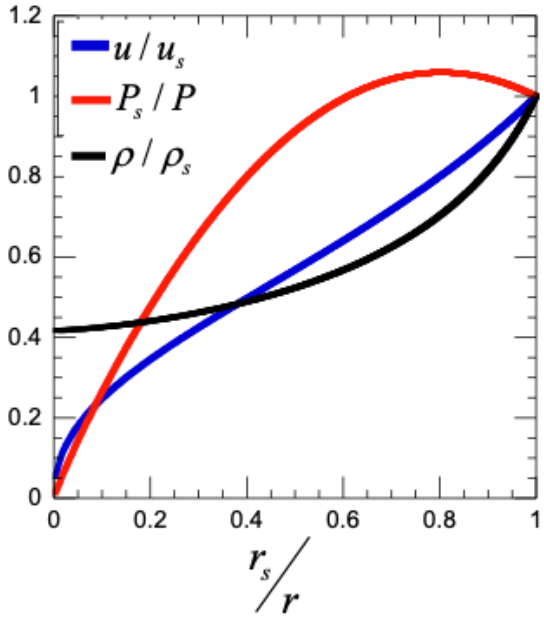

Figure 5. 2 Plots of Chisnell's self-similar in the form of ratios of particle properties: radial velocity (blue), pressure (red) and density (black), to shock properties, as a function of ratio of shock radial location to particle radial location.

5.2 **Results and Discussion**

5.2.1 Unperturbed, 1D Simulations

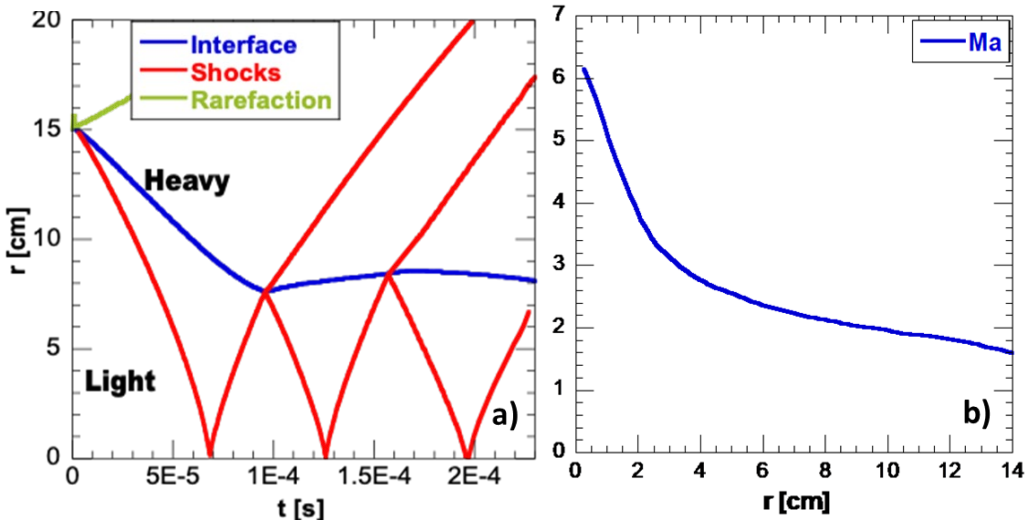

Figure 5. 3(a) Radial trajectories of the interface and shocks from an unperturbed 1D simulation. (b) Radial profile of the transmitted shock Mach number.

In Figure 5.3 (a), we show the radial trajectory of an unperturbed interface from 1D numerical simulations using the FLASH code. The r-t diagram shows the incident shock originating at r = 15.2 cm, and immediately interacting with the interface located at r = 15 cm. The pre-shock Atwood number is approximately equal to -0.75, which increases to ~ 0.82 following the initial shock compression of the fluids. The interaction results in a reflected rarefaction that exits the computational domain through the outflow surface at r = 20 cm. The transmitted shock continues to strengthen as it converges towards r = r_{min}, reaching a maximum Mach number of ~6 (Figure 5.3 (b)) before reflecting from the surface near the origin. The reflected shock once again interacts with the interface, so that the interface stagnates at r ~ 8cm from the reshock. The reshock event (Light → Heavy) generates additional reflected waves, which bounce back from the origin and shock the interface several times during the course of the simulation, as shown in Figure 5.3 (a).

For the example shown in Figure 5.3(a), the convergence ratio may be computed as $\frac{r_{initial}}{r_{final}}$ ~ 2. As pointed out by [55], in the heavy-light configuration, the flow evolves largely under RM, while the corresponding light-heavy configuration in a spherical geometry is also influenced by stretches of RT-dominated growth when the interface is accelerating/decelerating.

5.2.2 Multimode, 3D Simulations

The corresponding radial trajectories computed from the 3D simulation are plotted in Figure 5.4. We identify as bubble and spike locations, the radial extents where the surface-averaged mass fraction values reach 1 % and 99 % respectively. Since the Atwood number for the initial shock is negative, we expect a local phase inversion of the imposed perturbations at the interface. However, the surface-averaging is not capable of detecting

localized phase inversions of the perturbations, and this is not explicitly observed in Figure 5.4. During the initial collapse, the growth resulting from the initial conditions dominated by small scales, is muted. However, the reshock event at t ~ 100 μs deposits significant energy to the already nonlinear interface, thereby spurring rapid growth of perturbations during this phase of development. We also observe distinct asymmetry between bubble and spike locations (referenced to the unperturbed interface location), during the reshocked phase. By t ~ 250 μs, the interface has been reshocked a second time, which further accelerates perturbation growth. However, these subsequent shocks are progressively weaker in strength.

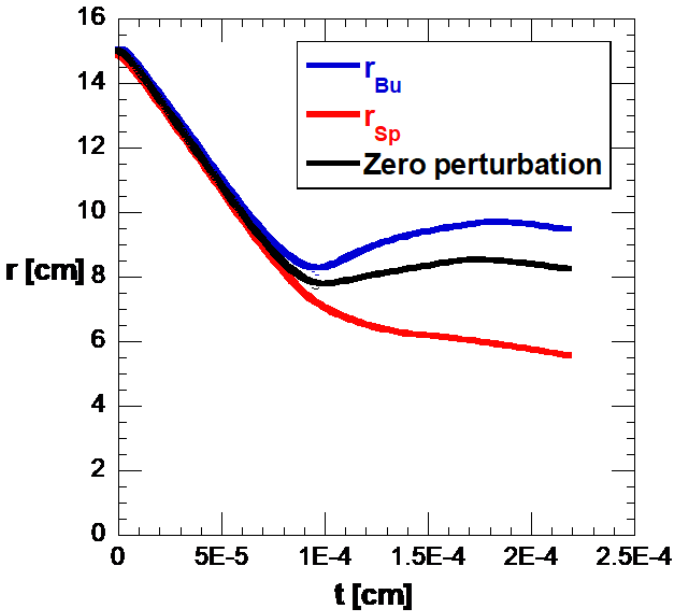

Figure 5. 4 Bubble and spike locations from 3D FLASH simulations of spherically convergent RM. The unperturbed interface trajectory is shown for reference.

Figures 5.5 (a) – (d) are plots of isosurfaces of the mass fraction (corresponding to surface averaged value of 50%), realized at key instances in the interface evolution shown earlier in Figure 5.3. Figure 5.5 (a) shows the interface shortly after the incident shock has

impacted the interface, and is marked by the presence of short wavelength modes. By t = 87.5 μs (Figure 5.5 (b)), these modes appear to have reached nonlinearity, but most of the energy is still concentrated in the high modenumbers. Shortly following the first reshock (Figure 5.5 (c)) at t = 107.5 μs, significant nonlinearity is observed along with cross-modal interaction which will eventually lead to mixing. The nonlinearity also results in asymmetric growth of spikes and bubbles in this high Atwood number flow. Note that the asymmetry is enhanced by convergence effects (Bell-Plesset effects [15, 16, 152, 153]), which accelerate the spikes disproportionately, since $r_{spike} < r_{bubble}$ for this configuration. We expect these effects to be more pronounced at late times due to the higher convergence, as well as the appearance of larger wavelengths on the bubble/spike fronts. Figures 5.5 (d)-(e) show the mixing layer immediately following the second reshock at t = 211.5 μs, with the interface characterized by significant turbulent mixing, and asymmetry between bubble/spike structures.

In Figure 5.6 we plot the time evolution of bubble and spike amplitudes separately, and evaluated as $h_{Bu} = r_{1\%} - r_{int}$, and $h_{Sp} = r_{int} - r_{99\%}$, where r_{int} is the radial location of the corresponding unperturbed interface obtained from Figure 5.3(a). Consistent with Figures 5.4 – 5.5, the interface retains symmetry following the first shock event, where the perturbation growth is confined to the linear stage. Significant asymmetry is observed for t > 90 μs (first reshock), with spikes outpacing bubble growth. Both bubble and spike amplitudes appear to saturate at late times, as the turbulent state decays as the effects of the shock recede.

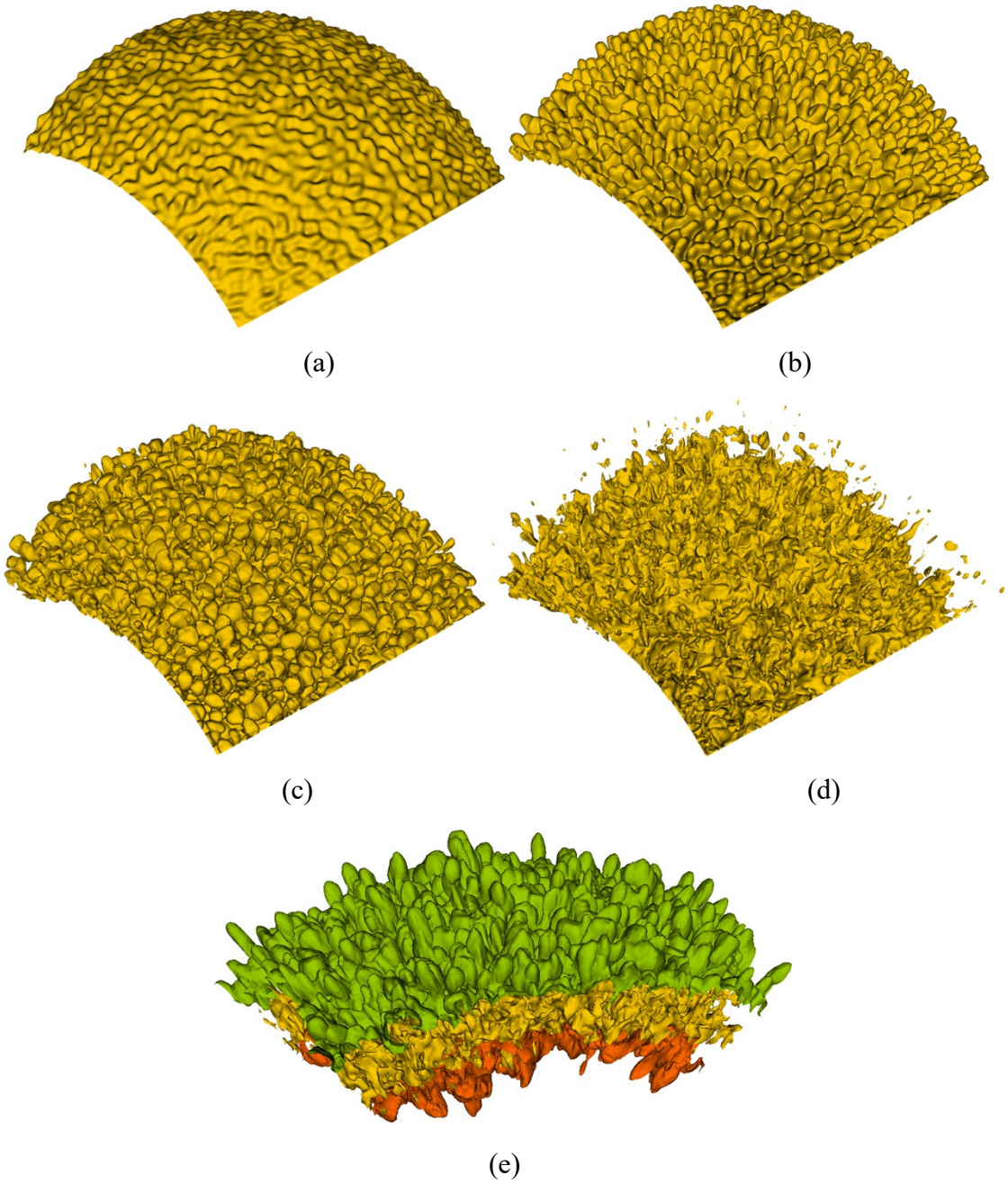

Figure 5. 5 Isosurfaces of mass fraction corresponding to the 50% level at (a) t = 58 μs, (b) 87.5 μs, (c) 107.5 μs and (d) 211.5 μs. Figure (e) displays iso-surfaces of 1%, 50% and 99% at t=211.5 μs.

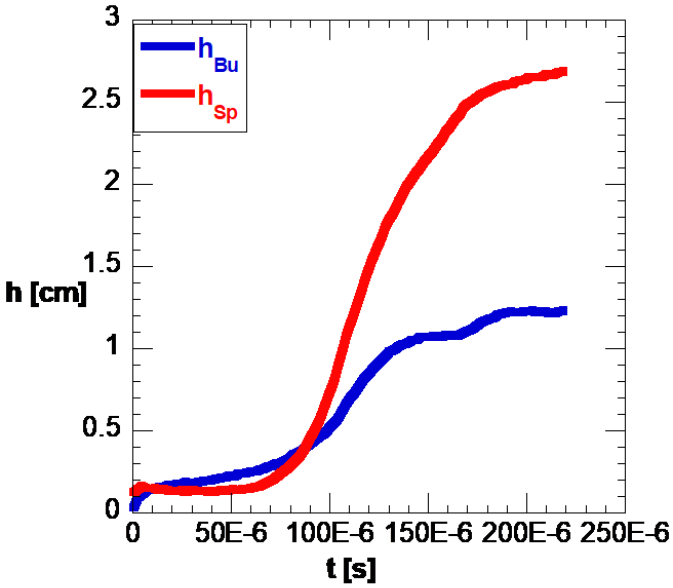

Figure 5. 6 Time evolution of bubble and spike amplitudes from FLASH simulation of spherically convergent Air/He interface.

5.3 **Summary and Conclusions**

We report on 3D ILES computations using the FLASH software, of a spherically convergent mixing layer, driven by a converging shock satisfying the Chisnell[151] self-similar solution. The configuration corresponds to a heavy-to-light RM instability, confined by a convergent geometry. The instability-driven mixing layer is shocked by a train of progressively weaker shocks reflected from the surface approximating the origin in our simulations. Significant mix development and asymmetry between bubble and spike structures (compounded by convergence effects) is observed in our simulations. Higher resolution simulations are planned for the future and will investigate the effect of initial shock strength and the role played by initial conditions in mix development.

CHAPTER 6 : IMPLOSION-DRIVEN VARIABLE-DENSITY TURBULENCE

We describe in this chapter the behavior of a spherical interface that degenerates in to a turbulent mixing layer when subjected to a spherical implosion. Results are presented from three-dimensional (3D) numerical simulations performed using the astrophysical FLASH code, while the underlying problem description is adopted from Youngs and Williams (YW). During the implosion, perturbations at the interface are subjected to growth due to the Richtmyer–Meshkov (RM) instability, the Rayleigh–Taylor (RT) instability, as well as the Bell–Plesset (BP) effects. We report on several quantities of interest to the turbulence modeling community, including the turbulent kinetic energy (TKE), components of the anisotropy tensor, density self-correlation, and atomic mixing, among others.

Youngs and Williams (YW) [14] defined an implosion problem in spherical geometry, as an idealization of the ICF process. In particular, Youngs and YW [14] used the Lagrange-remap code TURMOIL [41, 154] to perform high resolution, 3D numerical simulations of the implosion in a spherical wedge, with multimode perturbations prescribed at the interface between the gases. Joggerst et al. [54] performed a code comparison study to examine the effect of different meshes on instability growth at various stages of the implosion defined by [14]. They found the growth rates of short wavelength modes, in particular were affected by the choice of mesh, and a grid that is aligned with the interface was less susceptible to the rise of spurious modes at late times. Lombardini et al. [55, 56] used Large Eddy Simulations to investigate RM-driven turbulent mixing in a spherical geometry, where the drive was provided by a self-similar shock wave defined in [60, 151]. In this chapter, we report results

from high-resolution simulations of the implosion problem [14] using the FLASH [109] code, and describe in detail the behavior of several turbulent quantities at various stages of the implosion history.

The rest of the Chapter is organized in to numerical details and problem definition (section 6.1), results and discussion (section 6.2) and a summary (section 6.3).

6.1 **Numerical Details and Problem Definition**

We briefly review the problem definition from Refs. [14] and [54], before highlighting specific modifications required to simulate the problem with the capabilities embedded in FLASH. The problem configuration is adapted from [14], where the spherical implosion is driven by a time-dependent pressure drive (shown in Figure 6.2) applied to a moving boundary initially located at $r = 12\ cm$. The interface between dense, "shell" ($\rho = 1.0\ g/cm^3,\ 10\ cm \leq r < 12\ cm$) and light, "inner" ($\rho = 0.05\ g/cm^3,\ r < 10\ cm$) gases is initially at $R_0 = 10\ cm$, and can support a prescribed, multimode perturbation. Since FLASH is an Eulerian code, we introduce a third layer of a fictitious "outer" fluid ($12\ cm \leq r < 15\ cm$), whose purpose is to support the pressure drive, so that the interface between the outer and shell materials provides the required piston action. Following[54], the boundary location is forced to satisfy:

$$R_{bd}(t) = R_{out}(1 - u_{bd}t), \tag{6.1}$$

where $R_{bd}(t)$ refers to the time-dependent trajectory of the boundary, R_{out} is its initial location, and u_{bd} is a constant (0.2 s^{-1}).

Figure 6.1 is a cross-section of the spherical wedge $\left(\frac{\pi}{2} - \frac{\pi}{8} \leq (\theta, \phi) \leq \frac{\pi}{2} + \frac{\pi}{8}\right)$ investigated here, and shows the arrangement involving the three fluids, along with the corresponding

dimensions of the problem (in cgs units). Periodic boundary conditions were employed in the lateral directions, while the surface at $r = 15\ cm$ was treated as an outflow boundary to allow the reflected rarefaction (and other acoustic waves) to exit the computational domain without triggering spurious reflections. A reflecting boundary is placed at $r = dr$, so that the singularity at $r = 0$ is excluded from the computational domain. The fluid properties are listed in table 1. We use R_0 as a length scale, the initial interface jump velocity ΔU as a velocity scale, and $R_0/\Delta U$ as the time scale for normalizing the variables.

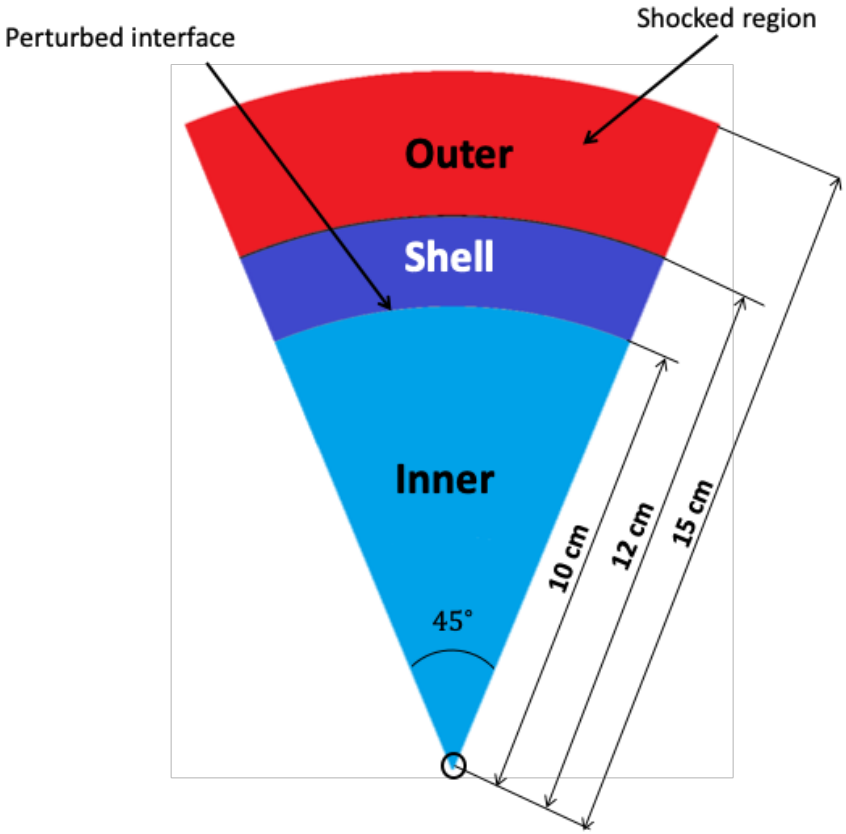

Figure 6. 1 Schematic of the numerical setup for the implosion problem defined by YW [14].

In the 3D simulations, the interface between the inner and shell materials was initialized with a multimode perturbation suggested by [14] (consisting of a superposition of cosine waves), with wavenumbers confined to $k_{\min} = \pi \le (k_\theta, k_\varphi) \le k_{\max} = \pi / 2dr$. The initial amplitudes and phases are randomized with a Gaussian distribution, thereby avoiding local pileups of peaks and valleys.

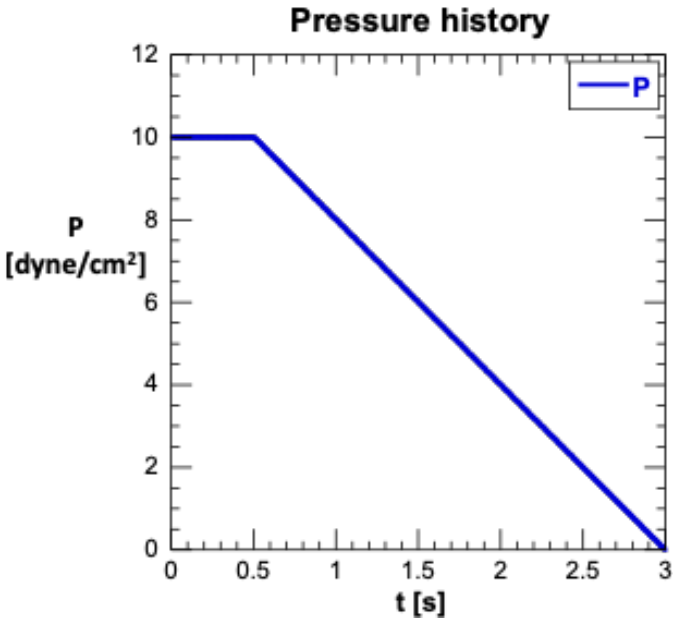

Figure 6. 2 Profiles of pressure applied in the third outer layer acting like a piston in time.

Table 6. 1 Simulation details and fluid properties

Fluid	$r(cm)$	γ	$p\left(\frac{dyne}{cm^2}\right)$	$\rho\left(\frac{g}{cm^3}\right)$	$e\ (erg)$
Inner	10	5/3	0.1	0.05	3
Shell	12	5/3	0.1	1	0.15
Outer	15	5/3	10	0.1	150

Following [14], the power spectrum of the perturbation field satisfies $p(k) = Ck^{-2}$ for $k_{\min} < (k_\theta, k_\varphi) < k_{\max}$, and $p(k) = 0$ otherwise. The constant C is chosen so that $s.d.^2 = \int p(k)dk$, where $s.d. = 0.005$ is the standard deviation of the perturbation field. Surface perturbations within a cell volume are converted to corresponding perturbations of the mass fraction *Y*. When more than a single fluid is present in a cell, the fluids are assumed to be numerically mixed leading to a corresponding cell mass fraction. Thus, we do not explicitly track the interface between the fluids, an approach that has been shown to be successful in the handling of flows with sharp discontinuities and shocks.

The resulting perturbation field is shown in Figure 6.3. The radial cell containing the perturbation is further sub-sampled to adequately resolve perturbation growth during the linear stages. In the next section, we present results from three simulations with grid resolutions in (θ, φ, r) of 128x128x384, 256x256x786 and 512x512x1536 zones. The AMR mesh is locally derefined to 64x64x192 in the region $r < 1.5cm$, to avoid the significant computational costs associated with tracking the convergent shock in that region at late times. From an examination of results from the two approaches, we found radial profiles of pressure, density and other quantities are in excellent agreement, and the maximum discrepancy in local values does not exceed 10% at any radial location and at any time.

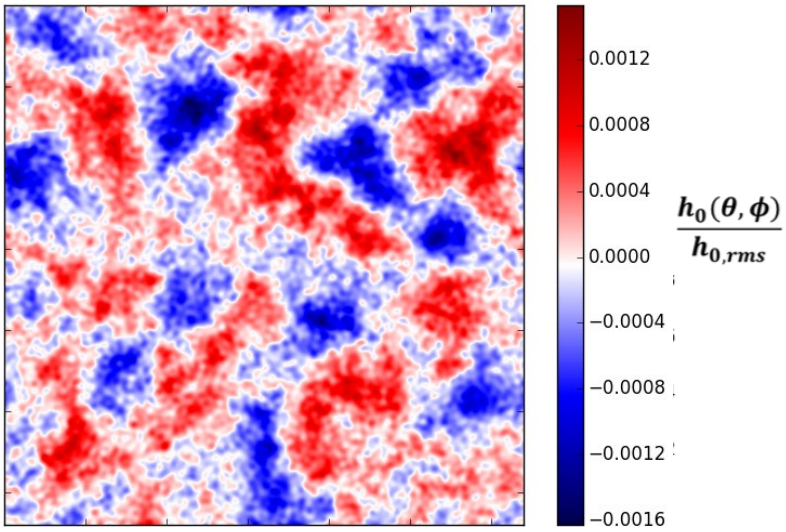

Figure 6. 3 Contours of the initial perturbation field.

6.2 **Results and Discussion**

6.2.1 Unperturbed, 1D Simulations

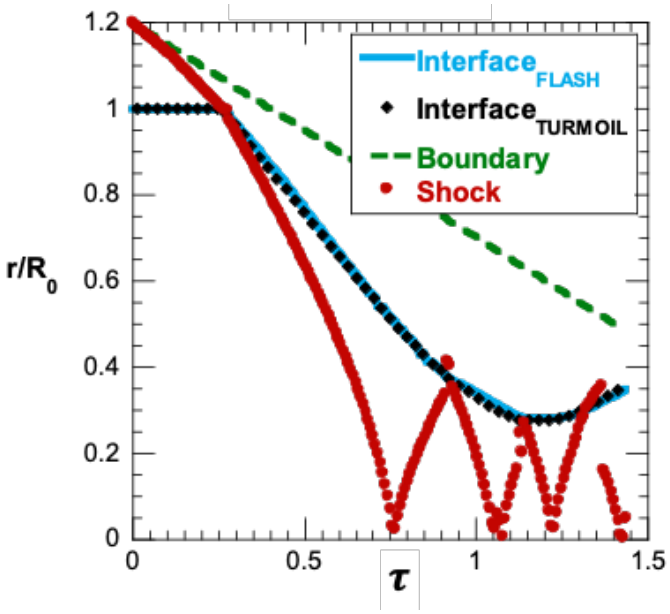

Figure 6. 4 Radial trajectories of the unperturbed interface, shocks and boundary from 1D, FLASH simulations. Results are compared with data from [14].

We verify our numerical problem setup by comparing results from a 1D, unperturbed simulation (768 zones in *r*-direction) with corresponding data from [14]. Figure 6.4 is a plot

of the trajectories of the inner/shell interface, as well as the external boundary between the shell and outer material which follows eq. (6.1). We also track the location of the driving shock in each case through local maxima of the pressure gradients. Thus, for $\tau \leq 0.24$, we plot the trajectory of the incident shock, while we track the transmitted and reflected shocks from the origin for $\tau > 0.24$.

The unperturbed, interface location from FLASH is compared with corresponding results from [14], and shows excellent agreement in Figure 6.4. Following the incident shock impact at $\tau = 0.24$, the interface is initially RM-unstable, while the large initial radius likely implies the effects of convergence will be limited at this stage. For the initial heavy → light interaction, the Atwood number associated with the inner/shell interface is – 0.905. The shock impact results in a transmitted shock and a reflected rarefaction, while the interface appears to coast with a nearly constant radial velocity. However, the transmitted shock is reflected from the origin, and shocks the collapsing interface several times in a light → heavy configuration. These interactions cause the interface to stagnate at $\tau \sim 1.2$, followed by a slight rebound. The flow development at this stage is complex and involves stages of RM instability immediately following each shock, interspersed with durations of RT instability subjected to variable acceleration. For the flow conditions investigated here, a radial convergence ratio of ~4 is observed in the FLASH simulations. As shown in [54], the use of an aligned coordinate mesh in FLASH here eliminates the formation of spurious, grid-seeded modes even at high convergences.

6.2.2 Multimode, 3D Simulations

The simulations were repeated in 3D with multimode perturbations described in section 2, and at the three different mesh resolutions to establish grid convergence. In Figure 6.5, we

plot the time history of the extents of the mixing layer defined as the *r*-locations where the planar-averaged mass fractions achieve values of 1 % and 99 %. The FLASH results shown are at the maximum mesh resolution employed in this study ($512\times512\times1536$) and compared with the corresponding data from [14]. From Figure 6.5, it is clear the initial RM phase of evolution produces scant growth, since the small amplitudes of the imposed perturbations ensure modes remain in linear growth at this stage. Significant amplitude growth is observed beginning at around $\tau \sim 0.96$ following the first reshock event, which re-energizes the nonlinear mixing layer.

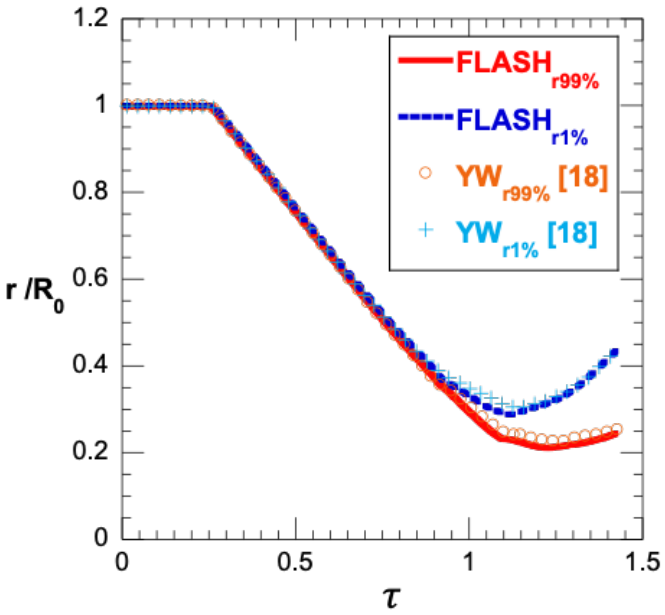

Figure 6. 5 Radial trajectories of the 1% and 99% angular-averaged iso-surfaces of the mass fraction, plotted from the 3D FLASH simulations with multimode initial perturbations. Results are compared with data from YW [14].

This is followed by aggressive growth of the mixing layer driven by a combination of reshock-driven RM growth, variable acceleration RT growth as well as BP effects due to the high convergences at late times. Figure 6.6 (a)–(e) represent iso-surfaces of mass fraction of the inner fluid satisfying the condition $\overline{Y_{inner}} = 0.5$ where the $<\bullet>$ denotes

planar-averaging along (θ,φ). At $\tau = 0.87$, the interface growth favors shorter wavelengths, which have the highest linear RM growth rates. The shape of the mass fraction iso-surface immediately following reshock is illustrated in Figure 6.6 (b), and shows that once individual modes have reached nonlinear saturation ($h \sim \lambda$), larger wavelengths are formed through mode-coupling. By $\tau = 1.08$ (Figure 6.6(c)), we observe the onset of cross-modal interactions and mode coupling which will eventually lead to mixing. Figure 6.6 (d) – (e) show the turbulent mixing layer at late times, when multiple reflected shocks have passed through the interface. At these late times, the iso-surface is characterized by significant levels of mixing, and asymmetry between the bubble and spike fronts. The bubble-spike asymmetry is a result of the large density contrasts between the fluids, but also due to convergence effects which favor inward pointing spikes.

We plot the angular-averaged mass fraction (inner fluid) profiles $\overline{Y_{inner}}$ across the mixing layer in Figure 6.7 (a), corresponding to the times shown in Figure 6.6. When the radial coordinate is scaled as shown in Figure 6.7 (a), the profiles are anchored at $(r-r_c)/W \sim 0.5$. At late times, the flow appears to settle down to a self-similar state, evidenced by the collapse of the mass fraction profiles for $\tau > 0.96$. As the reflected shocks repeatedly impact the flow at late times, the underlying self-similarity of the flow does not appear to be affected. The corresponding product $\overline{Y_{inner}Y_{shell}}$ is plotted as a radial function in Figure 6.7 (b). At late times, $\langle Y_{inner}Y_{shell}\rangle$ peaks at the centerline at ~ 0.18, where a value of 0.25 would indicate perfect mixing. Once again, the profiles collapse at late times ($\tau > 0.96$) suggesting the flow reaches a self-similar state when subjected to mixing from repeated shocks and RT.

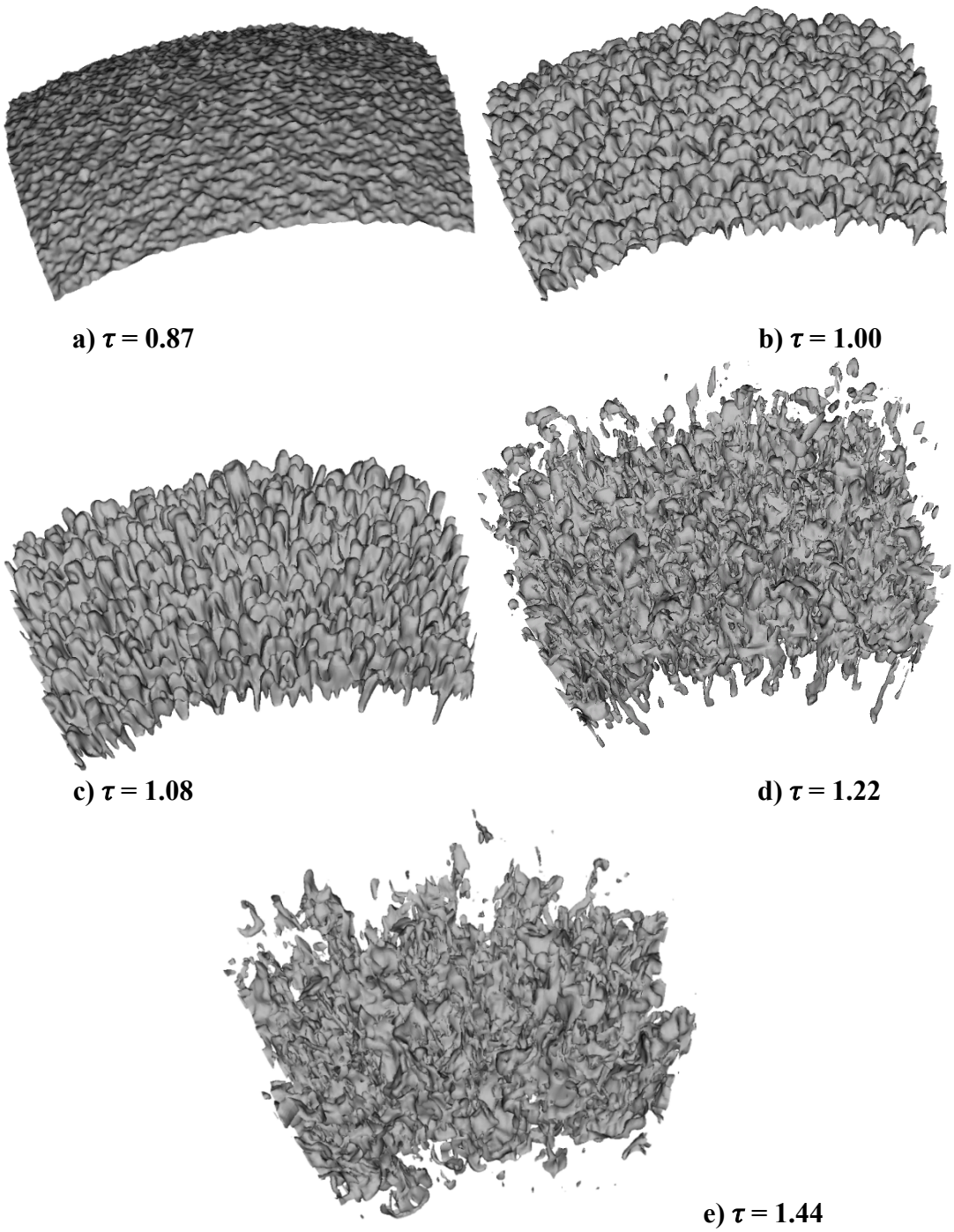

Figure 6. 6 Iso-surfaces of the mass fraction corresponding to the 50% level at (a) τ = 0.87, (b) τ = 1.00, (c) τ = 1.08, (d) τ = 1.22 and (e) τ = 1.44.

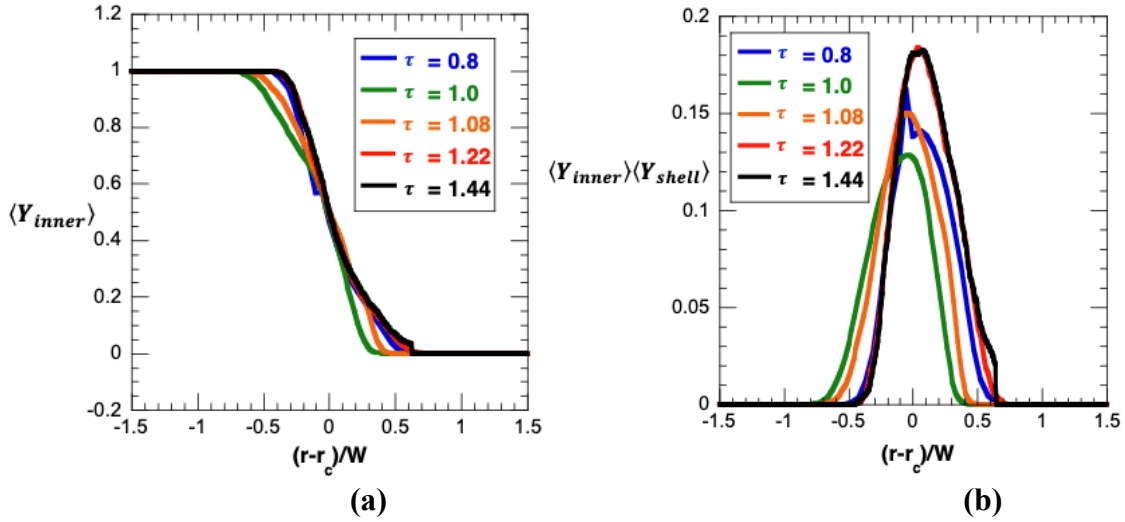

Figure 6. 7 Radial profiles at different times of (a) <Yinner> and (b) <Yinner Yshell>.

For RM flows, the amplitude of the mixing layer is typically defined as $r_{99\%} - r_{1\%}$ where $r_{99\%}$ ($r_{1\%}$) denotes the radial location of the surface $<Y_{inner}> = 99\%\ (1\%)$. In Figure 6.8, we plot the time evolution of the mixing layer amplitude from FLASH simulations with mesh resolutions of $256\times256\times768$ and $512\times512\times1536$. The results are compared with corresponding data from [14], and show good agreement. Consistent with the images of the iso-surfaces discussed above, the growth rate of the mixing layer falls in the linear regime until the first reshock event $\tau \sim 0.96$. Significant nonlinear growth and mixing is observed at late times, due to the combination of RM/RT/BP effects. In Figure 6.8, we also show results from the simulations at lower resolutions (128 zones and 256 zones). At late time, following reshock the simulations show good mesh convergence and are in agreement with the results from [14]. At early times, the simulation with 128 zones (and to a lesser extent the 256 zone calculation) shows a larger mixing width compared with the highest-resolution case. At these early times, the growth of the mixing width is due to the linear growth of

individual modes, so that the larger width observed in the poorly resolved (128 zone) case is attributable to the numerical diffusion dominating over the linear growth.

We track the fraction of molecularly mixed fluid through the atomic mix parameter

$$\Theta(t) = \frac{\wp(t)}{\delta(t)} = \frac{\int_0^\infty <Y(1-Y)> dr}{\int_0^\infty \langle Y\rangle\langle 1-Y\rangle \, dr} \ , \tag{6.2}$$

where $\wp(t)$ and $\delta(t)$ represent the actual chemical product thickness and the maximum thickness product formed with complete mixing respectively [56]. Thus, the measure in eq. (6.2) compares large-scale stirring with small-scale mixing that is associated with a numerical diffusivity.

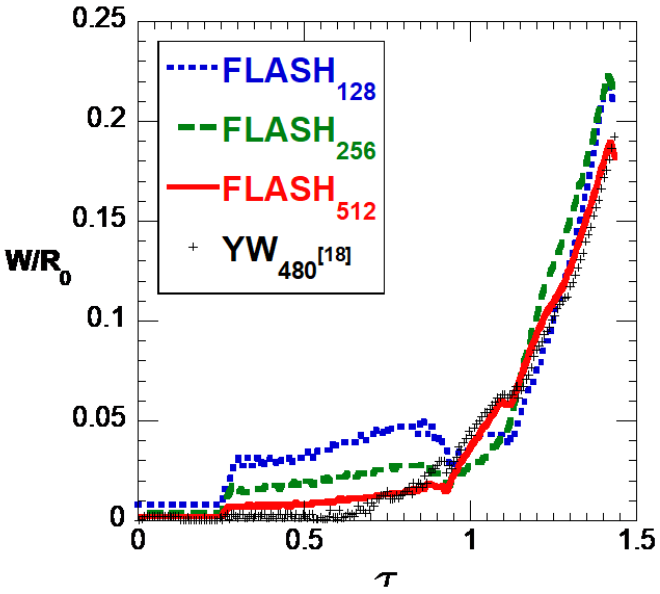

Figure 6. 8 Time evolution of the turbulent mixing amplitude W in a spherical implosion. Results from FLASH are compared with TURMOIL data from [14].

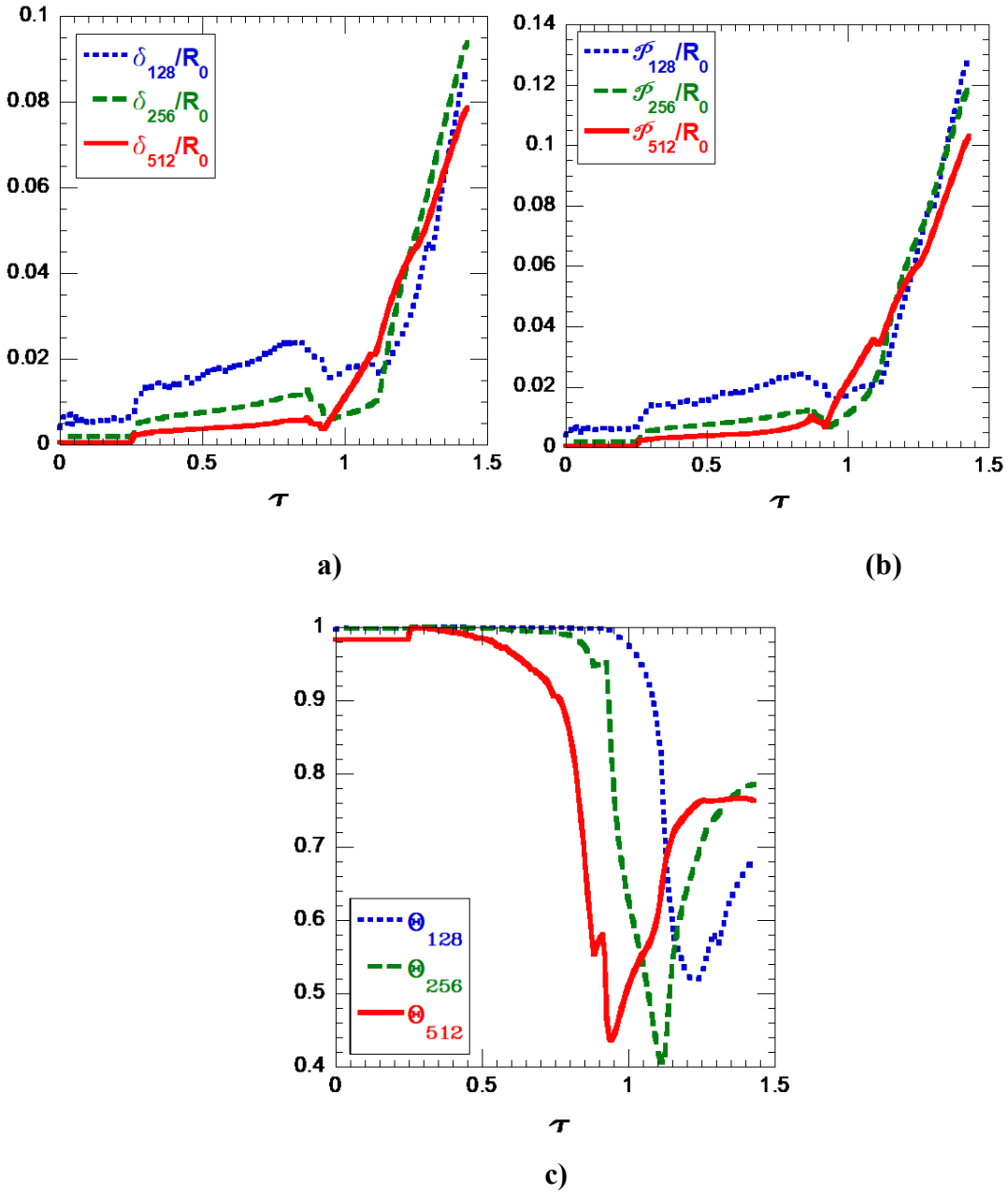

Figure 6. 9 Time evolution of a) the maximum molecular mixing thickness δ(t), b) the total molecular mixing thickness ℘(t), and c) the atomic mix parameterΘ.

Note that $\Theta(t)$ is related to the intensity of segregation $I(t)$ through $\Theta(t) = 1 - I(t)$, and can change from 0 → 1 to indicate variation from segregated to completely mixed states. In Figure 6.9, we plot the evolution of the atomic mix parameter $\Theta(t)$, as well as $\wp(t)$ and $\delta(t)$

from our highest resolution simulations. The high values of $\Theta(t)$ observed at early times ($\tau < 0.96$) during which the linear mixing layer exhibits little mixing, are an artifact of the discrete representation of the initial interface in our simulations. At early times, when the interface is confined to within a cell, the only contribution to the integral in eq. (6.2) is from the presence of both fluids in a given cell volume [115]. After reshock ($\tau > 0.96$), the nonlinear growth spreads the interface across multiple mesh zones, so that the atomic mix becomes a more reliable indicator of the fraction of molecularly mixed fluid within the mixing layer. At late times, the atomic mix parameter approaches a value of ~ 0.7, consistent with earlier findings of mixing in RT and RM flows.

The behavior of the widths $\wp(t)$ and $\delta(t)$ from the lower resolution simulation (128 zones) is consistent with the trend observed in Figure 6.8 for the mixing layer amplitude – discrepancies at early time due to the dominance of numerical diffusion over linear growth of modes, and convergence to the high-resolution results at late times when the flow is dominated by nonlinear growth and turbulence. Simulations at the lower mesh resolution show the same qualitative trend in the behavior of the atomic mix parameter, while the transition from the initial (artificial) Θ value occurs at different times in each case. Specifically, the higher resolution simulations show this transition earlier, since these calculations had much smaller mesh sizes that the nascent flow can outgrow at an earlier time. When this occurs, the value of Θ transitions from the artificial initial value to a measure that is reflective of the fraction of atomically mixed fluid within the flow.

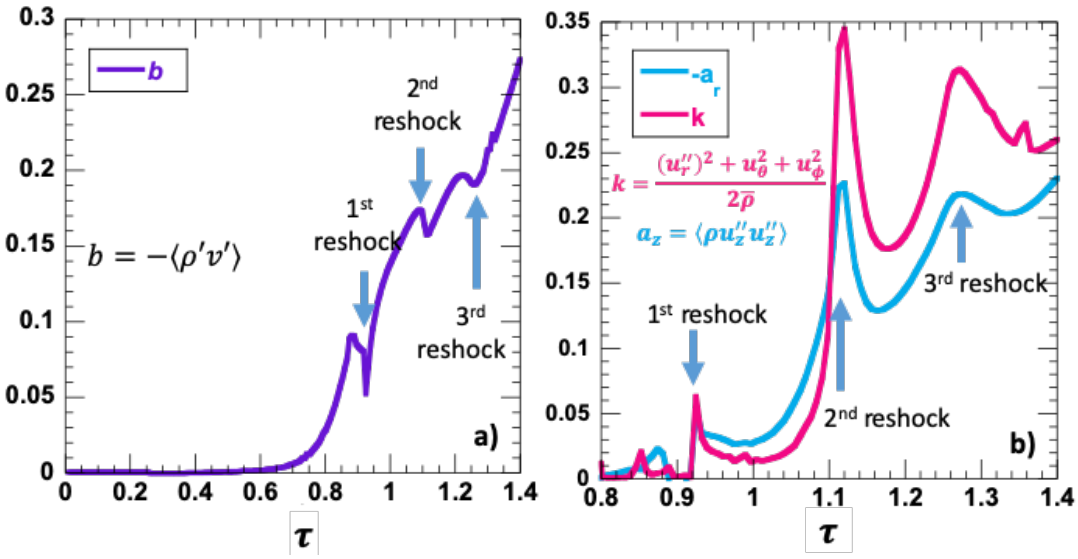

Figure 6. 10 Time evolution of the centerline density-specific volume correlation b in (a) and the radial mass flux a_r and turbulent kinetic energy k in (b).

The time evolution of the density-specific volume correlation $b = -\langle \rho' v' \rangle$ computed at the centerline of the turbulent mixing zone is plotted as a function of the non-dimensional time in Figure 6.10(a). As the mixing layer grows, there is a concomitant increase in *b*. Following the first reshock at $\tau \sim 0.96$, a sharp decrease in *b* occurs, due to compression of the mixing layer by the reflected shock. At late times, the turbulent mixing layer grows due to repeated re-shocking events, as well as Bell-Plessett [15, 16] effects due to confinement. This results in increased mixing, and is observed here as a late-time increase in *b*. In Figure 6.10(b), we plot the time evolution of the radial turbulent mass flux $a_r = < u_r'' >$ and the TKE, *k* computed at the center of the mixing layer. Following [14], we use the definition

$$k = \frac{1}{2}\frac{\langle \rho\left((u_r'')^2 + u_\theta^2 + u_\varphi^2\right)\rangle}{\langle \rho \rangle}, \tag{6.3}$$

where u_r'' is the fluctuation about the mass-averaged radial velocity. Once again, compression due to reshocks are evident as short-lived spikes in these quantities, while the

intensification of the turbulence due to confinement and baroclinic vorticity deposition produces a more secular growth in time.

The radial profile of the turbulent kinetic energy at $\tau \sim 1.44$ is plotted in Figure 6.11 from the FLASH simulations at different mesh levels. The radial coordinate is scaled as $(r - r_c)/W$, where r_c denotes the radial location with $\langle Y \rangle = 0.5$, and W is the amplitude of the mixing layer. In Figure 6.11, the two simulations with the highest resolutions show the TKE has converged across the mixing layer, while the coarsest simulation yields marginally higher values. In Figure 6.12(a) and Figure 6.12(b), we plot cross-stream profiles of the anisotropy tensor at the instance of stagnation, and at the final time respectively.

The anisotropy tensor is defined according to:

$$B_{ij} = \frac{\langle v_i v_j \rangle}{2TKE} - \frac{1}{3}\delta_{ij} \tag{6.4}$$

where $\langle v_i v_j \rangle$ are components of the Reynolds stress tensor. For isotropic turbulence, $B_{ij} = 0$, while strong anisotropy suggests $B_{ij} \rightarrow 2/3$ in the dominant direction (and $B_{ij} \rightarrow -1/3$ in the other directions) [91]. The diagonal components of the anisotropy tensor are plotted as a function of the non-dimensional radial coordinate at stagnation (Figure 6.12(a)) and at the end of the simulation (Figure 6.12(b)). Both plots suggest strong anisotropy in the radial direction with $B_{rr} \sim 0.27 \pm 0.01$ and 0.38 ± 0.01 at $\tau \sim 1.22$ and $\tau \sim 1.44$ respectively. In contrast, the angular components are restricted to 18.5 % of the total energy at those times. However, the levels of anisotropy observed here is lower than in other directed flows such as RT [115], and could be due to the repeated realignment (scrambling) of the mixing layer from multiple reshock events.

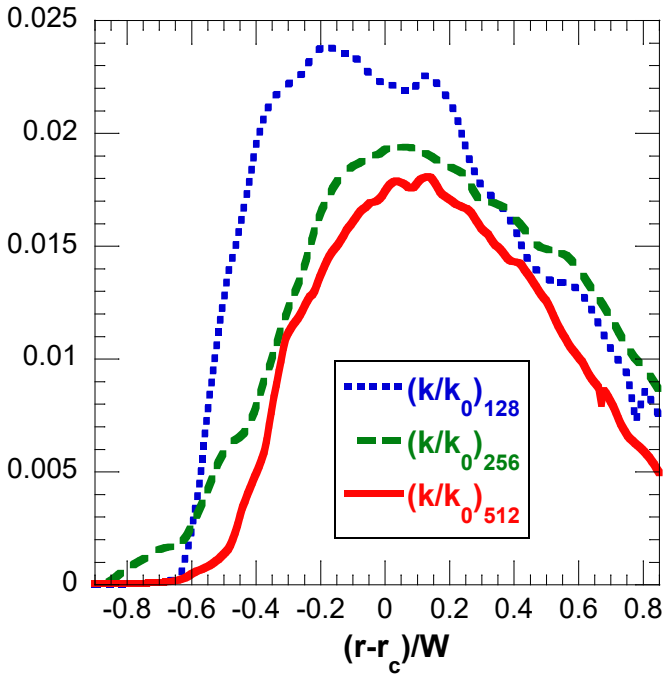

Figure 6. 11 Cross-stream profiles of the turbulent kinetic energy (TKE) scaled by $k_0 = \frac{1}{2}\rho_{avg}\Delta U^2$ from FLASH simulations at different mesh resolution, and plotted at $\tau = 1.44$.

In variable density flows such as RT and RM turbulent flows, quantities such as the normalized mass flux a_i and the density specific volume correlation parameter b are important in understanding turbulent transport within the mixing layer [91, 123]. In particular, in the non-Boussinesq limit, these quantities can develop asymmetries across the mixing layer, in proportion to the density contrast between the fluids. The normalized mass flux in the i^{th} direction is defined as $a_i = \frac{<\rho' v_i'>}{<\rho>}$, and has been recognized to be a critical quantity in the conversion of potential energy to kinetic energy in buoyancy-driven flows [91, 123]. In Figure 6.13(a), we plot the cross-stream profiles of the normalized mass flux in the radial direction (a_r), for the two highest resolved cases at the end of the simulation ($\tau \sim 1.44$).

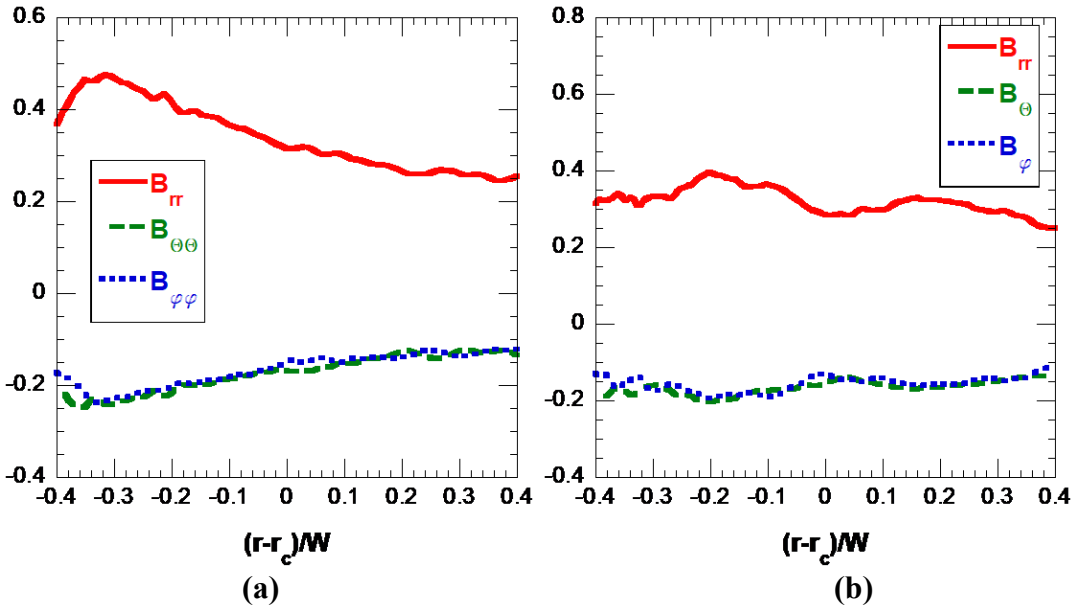

Figure 6. 12 Cross-stream profiles of diagonal components of the anisotropy tensor at (a) τ = 1.2 (stagnation), and (b) at τ = 1.4.

The obtained a_r profiles are asymmetric and skew towards the spikes, suggesting greater mass flux associated with the spikes due to the large density differences. This velocity increase on the spike side is also compounded by greater geometric convergence experienced by the spikes, which are directed inward towards the origin.

In [56, 123], the authors show the density specific volume correlation parameter $b = -\langle \rho' \left(\frac{1}{\rho}\right)' \rangle$, can modify the production term in the radial mass flux equation. In Figure 6.13 (b), we plot the radial profile of the b parameter at $\tau \sim 1.44$, and at the two highest mesh resolutions. The peak values obtained here (~0.28) are similar to values reported by Lombardini and Pullin [56] for their heavy→light simulation in a spherical geometry. Once again, the profiles are skewed towards the light side of the mixing layer, suggesting the flow is highly non-Boussinesq and requiring the solution of variable density equations in modeling transport [123].

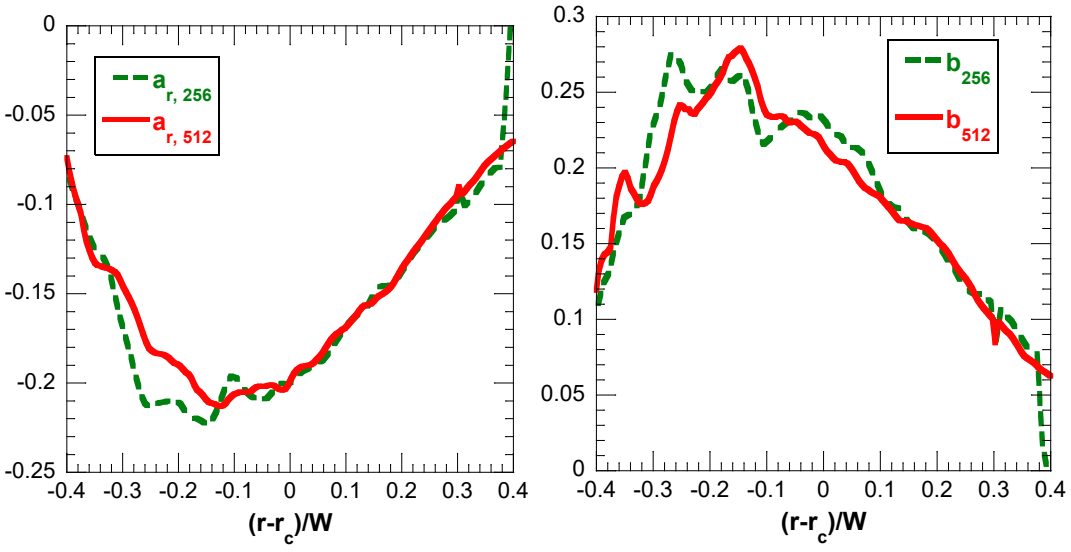

Figure 6. 13: Cross-stream profiles of (a) the radial normalized turbulent mass flux ar, and (b) of the density-specific volume correlation b. Both quantities are plotted at τ = 1.44.

Following [155], we compute the turbulent kinetic energy spectra associated with variable density flow as

$$E(k) = \frac{1}{2}\iint \sum_{i=1}^{3} (\widehat{\rho v_i}\,\hat{v}_i^{*} + \widehat{\rho v_i}^{*}\,\hat{v}_i), \tag{6.5}$$

where '$\widehat{\ }$' indicates a two-dimensional Fourier transform operation performed on a (θ,φ) plane of statistically homogeneous data, while '*' represents the corresponding complex conjugate. Thus, the 2D FFT operations were performed on (θ,φ) planes corresponding to the radial location $r_{|Y_{inner}=0.5}$, while the double integral in the above equation indicates averaging over a circular region in wavenumber space, thus resulting in a 1D kinetic energy spectrum. In Figure 6.14, we plot energy spectra from three critical moments in the flow, viz: following the initial shock as modes achieve nonlinearity (Figure 6.14(a)), immediately following reshock (Figure 6.14(b)), and at late time (Figure 6.14(c)). In each case, the kinetic energy spectra are compensated by the coefficient $k^{5/3}$ to highlight the

inertial range, while the wavenumber axis is non-dimensionalized with *R(t)*, the radius of the corresponding unperturbed interface at that time.

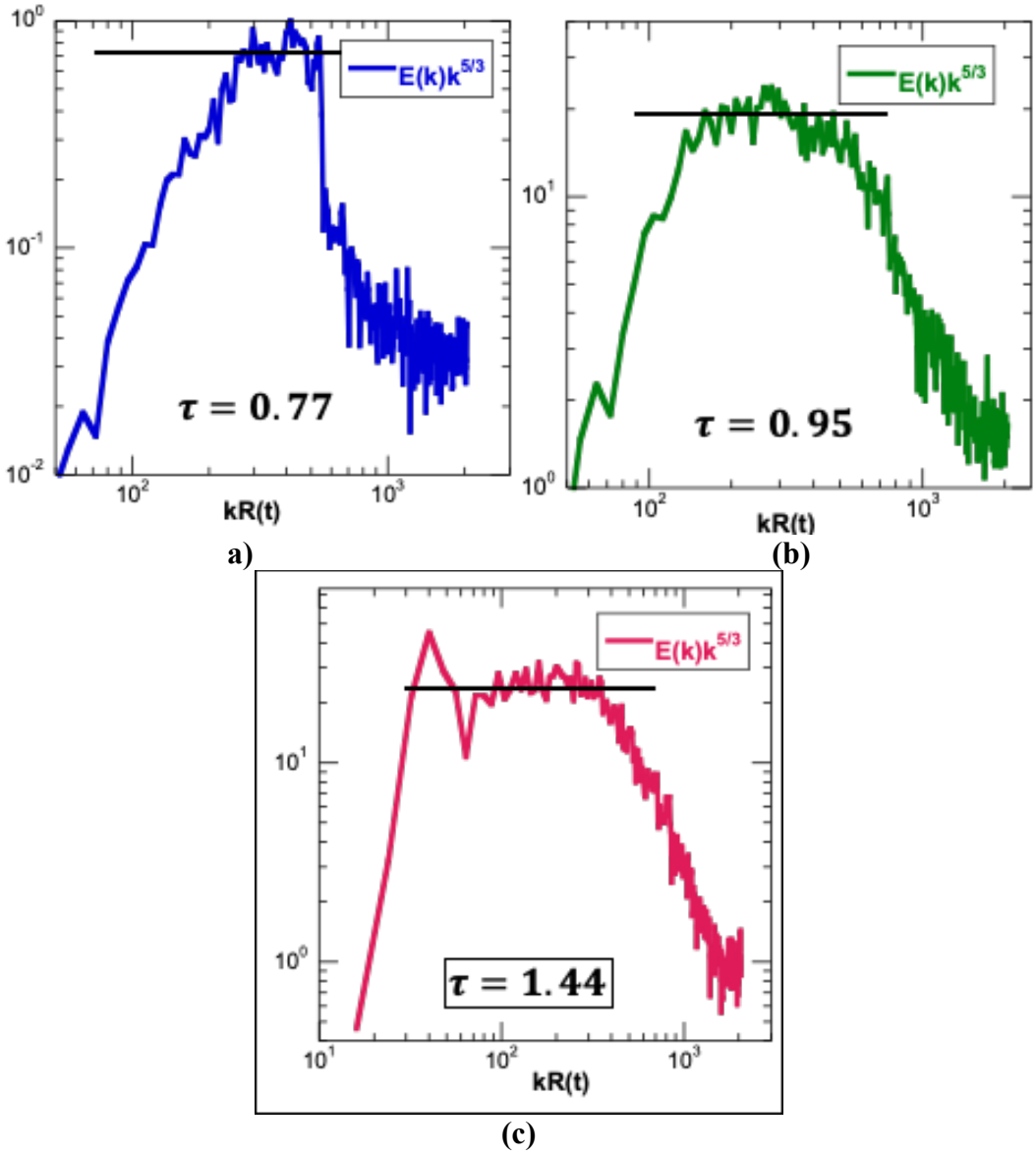

Figure 6. 14 Compensated kinetic energy spectra obtained from radial locations where Y_{inner} = 50%: (a) τ = 0.77, (b) τ = 0.95 and (c) τ = 1.44.

The energy spectrum shown in Figure 6.14(a) was obtained at $\tau = 0.77$, following the incident shock and still shows the imprint of the initial conditions. At this early time, a

narrow band of modes appear to have evolved to nonlinearity ($h \sim \lambda$), while the long wavelengths have not filled in. At $\tau = 0.95$ (Figure 6.14(b)), the appearance of an inertial range is evident as the flow has clearly transitioned to turbulence following the reshock event. However, the inertial range at this time is narrow, and represents a flow developing in to an eventual self-similar state. Figure 6.14(c) is obtained from the $r_{|Y_{inner}=0.5}$ surface at late time ($\tau = 1.44$), and shows an inertial range spanning a decade, with a slope approaching $k^{-5/3}$. The broadband nature of the spectrum, and the existence of a substantial inertial range suggests the flow exhibits a self-similar state at these late times. From the kinetic energy spectra, we determine the inner viscous length scale λ_v as the intersection point between the fiducials corresponding to the inertial and the dissipation ranges. For $\tau = 1.44$, we find $k_v R(t) \sim 220$, where $k_v = 2\pi/\lambda_v$ and $R(t)$ is the location of the corresponding unperturbed interface. The outer length scale is given by $\delta \sim W(t)$, where $W(t)$ is the amplitude of the turbulent mixing layer, so that the effective Reynolds number is obtained as [156-159] $Re = \left(50\,\delta/\lambda_v\right)^{4/3} \sim 1.1e4$. A similar analysis conducted at $\tau = 0.95$, yields $k_v R(t) \sim 410$ and $Re \sim 1.25e3$.

6.3 **Summary and Conclusions**

We have discussed results from numerical simulations of a spherical implosion of relevance to the ICF application. The problem statement was originally defined by YW [14], and also serves as a benchmark for evaluating different numerical algorithms. The simulations were performed here with the widely used FLASH code, for two different conditions: unperturbed interface, and an interface initialized with multimode

perturbations. The flow conditions and initialization was chosen to match parameters in [14, 54], while the problem setup had to be modified to introduce an outer layer of fluid that could serve to support the driving shock. Thus, the interface between the outer fluid and shell material in the Eulerian simulations discussed here serve the purpose of the moving boundary in the ALE code TURMOIL [41, 154]. Nevertheless, we find several quantities of interest including the radial trajectory of the unperturbed interface, and the mixing width of the turbulent flow to be in very good agreement with results from [14].

The implosion of a spherical interface is susceptible to multiple instabilities, resulting in a complex evolution over time. The initial growth is driven by the convergent shock, and can be attributed to RM growth of linear modes. At late times, the nonlinear mixing layer is repeatedly impacted by shocks reflected at the origin, interspersed with stages of RT-driven growth. This is also reflected in the atomic mix parameter, which saturates to ~ 0.7 at late times following the interactions of the interface with the reflected shocks. In addition, at the convergence ratios achieved here BP effects are expected to play a role, thus contributing preferentially to the growth of the spike front. At late times, the flow evolves to higher levels of anisotropy, with much of the turbulent kinetic energy residing in the radial component.

In the future, we plan to extend this work by comparing results from the FLASH simulations with turbulent mix models [52, 123, 155]. Future studies will also include detailed investigations in to the effects of the convergence ratio, the initial conditions, and the shock strength on the development of the turbulent mixing layer properties discussed in this paper.

CHAPTER 7 : SUMMARY AND CONCLUSIONS

A broad class of variable density turbulent flows have been investigated using detailed and carefully designed numerical simulations. The turbulent flow in each case was generated as the culmination of hydrodynamic instabilities associated with perturbed interfaces separating fluids of different densities. The flows may be categorized based on the persistence and form of the applied drive as well as the degree of anisotropy. The RT instability was investigated for multimode perturbations driven by a constant acceleration. In the RM instability, the drive is impulsive and is usually provided by shock passage through the interface of interest. We have investigated the special case of twice-shocked RM instability, in which both shocks were directed from the heavy fluid towards the light. A spherical implosion problem, in which the drive may be considered to be complex and variable was also investigated. We briefly summarize key results from each investigation below:

1. Rayleigh-Taylor Turbulence: In these simulations, a narrow-band perturbation spectrum[47] was imposed on the interface, accelerated by applied gravitational acceleration. In our simulations, the flow appeared to reach self-similarity for $\tau > 1$, where $\tau = t\sqrt{Ag/L_0}$. The self-similar state of the flow is characterized by constant, late-time values of the streamwise mass flux, density-specific volume correlation and the TKE, as well as the collapse of cross-stream profiles of these quantities when plotted on appropriate self-similar coordinates. Results from these simulations were compared with the LWN model of (SCH) [106, 107] , described in §3.2.3. Preliminary comparison with the model results of Steinkamp[106, 107] showed that the mix width and b-profiles to be in good agreement

between the simulation and the model. However, differences in the mass flux and TKE profiles were observed between ILES and the LWN model. These discrepancies may be due to the manner in which the inviscid limit is treated in the ILES calculations and the model, where the implicit numerical dissipation of TKE in the simulations is not included in the model. Follow-on simulations with an added physical viscosity are planned to address these discrepancies.

2. **Double-Shocked Richtmyer-Meshkov turbulence:** In contrast to most studies of RM turbulence in which the interface was processed by a single-shock, or by incident and reflected shocks, we have studied the configuration in which both shocks were in the same direction. The specific case of heavy-to-light (slow-fast) interaction was examined using high-resolution numerical simulations using the FLASH code. The problem was suggested by Mikaelian[144] and is of relevance to recent efforts at the National Ignition Facility (NIF) to exploit precisely-timed shocks to achieve improvements in the fuel areal density and neutron yield. Similarly, in Scramjet combustion, the short fuel residence times are overcome by the use of shock trains that increase mixing[160].

In our simulations, the time of arrival of the second shock was varied as a control parameter, to isolate the effect of the interface initial conditions at the time of the second shock on late-time self-similarity. Simulations in which the second shock arrived at scaled times of τ = 1, 3 and 6 were performed, where $\tau = t\dot{W}_0 \backslash \bar{\lambda}$. At τ = 0, the interface was perturbed with a k^{-2} perturbation defined in the "θ-group collaboration", which was also used as a baseline for comparison. Since both shocks traversed the interface from the heavy fluid to the light, the negative Atwood number associated with these interactions lead to a negative RM growth rate[132], accompanied by phase reversal of the interface. However,

when the interface is already nonlinear at second shock, the phase reversal of leading bubble or spike structures can be hindered by the presence of lagging structures. This leads to collapse and breakup of such structures, which we term 'shredding' after a similar phenomenon observed in accel-decel-accel studies of the Rayleigh-Taylor instabilities. The outcome of shredding is a transition to small-scale structures, and a momentary increase in the atomic mixing (or decrease of b). The dynamics of shredding complicates the initial conditions for the post-second shock growth of the mixing layer, and deserves further analysis. In particular, a detailed modal analysis of the interface immediately before and following the second shock would be instructive.

In spite of these uncertainties associated with the second shock initial conditions, we find the behavior of the late-time mixing layer to conform to self-similarity. The initial conditions appear to determine the initial linear growth rate, and the transition time to self-similar behavior. However, at late-times all the simulations approach a growth exponent $\theta \sim 0.25$, similar to the original θ-group study. This is in contrast to earlier studies of the role of initial conditions on RT turbulence[125, 161], which showed growth rates to retain their dependence on the initial perturbations through the self-similar stage.

3. Spherical Implosions: To investigate the properties of variable density turbulence when it is distorted by geometric confinement, simulations of the spherical implosion problem defined by Youngs[14] were performed using FLASH. To optimize the use of mesh resources, the transmitted shock is tracked using azimuthally-fused cells in the region near the origin (see Appendix A2). Since FLASH is an Eulerian code, the outer moving boundary driving the implosion was modeled by adding an extra layer of fictitious fluid with a prescribed pressure history. This creates a radial trajectory of the boundary between

the outer layer and the shell material. The interface of interest actually separates the shell from the inner fluid, and supports multimode perturbations in the simulations. Unperturbed simulations showed a convergence ratio of ~ 4, while the radial trajectory is affected by RM, variable-g RT as well as Bell-Plessett effects.

Together, these effects constitute a variable drive with a complex acceleration history applied to the perturbed interface. The initial stages of the interface development are dominated by RM instability from the incident shock interaction. During this stage, bubble and spike growth is symmetric. As the interface approaches the origin, it is repeatedly reshocked by the reflected shocks, resulting in deceleration (with a variable g) and stagnation. During the deceleration, the interface is Rayleigh-Taylor unstable, leading to additional growth of the mixing layer. In addition, BP effects are observed due to spherical convergence and contribute significantly to the growth of the mixing layer. These effects create considerable stretching of the coherent structures within the mixing layer, as observed in the increase of b at late times. Similarly, cross-stream profiles of the components of the anisotropy tensor reveal significant levels of anisotropy within the late-stage mixing layer. Such simulations provide a hydrodynamic baseline of implosion physics, that can be used in the validation of mix models that are used in multiphysics codes.

REFERENCES

1. J. D. Lindl, *Inertial confinement fusion* (American Institute of Physics, 1998).

2. S. Atzeni, and J. Meyer-ter-Vehn, *The physics of inertial fusion* (OUP Oxford, 2004).

3. M. Zingale, S. E. Woosley, J. B. Bell, M. S. Day, and C. A. Rendleman, "The physics of flames in Type Ia supernovae," Journal of Physics: Conference Series **16**, 405 (2005).

4. M. Herant, W. Benz, W. R. Hix, C. L. Fryer, and S. A. Colgate, "Inside the supernova: A powerful convective engine," The Astrophysical Journal **435**, 339 (1994).

5. C. Y. Wang, and R. A. Chevalier, "Instabilities and Clumping in Type Ia Supernova Remnants," The Astrophysical Journal **549**, 1119 (2001).

6. Q. Yang, J. Chang, and W. Bao, "Richtmyer-Meshkov Instability Induced Mixing Enhancement in the Scramjet Combustor with a Central Strut," Advances in Mechanical Engineering **6**, 614189 (2014).

7. S. Zhong, and M. T. Zuber, "Degree-1 mantle convection and the crustal dichotomy on Mars," Earth and Planetary Science Letters **189**, 75 (2001).

8. W. R. Peltier, and C. P. Caulfield, "Mixing efficiency in stratified shear flows," Annu Rev Fluid Mech **35**, 135 (2003).

9. J. D. Woods, "Wave-induced shear instability in the summer thermocline," Journal of Fluid Mechanics **32**, 791 (1968).

10. L. Rayleigh, "Investigation of the Character of the Equilibrium of an Incompressible Heavy Fluid of Variable Density," Proceedings of the London Mathematical Society **s1-14**, 170 (1882).

11. G. I. Taylor, "The instability of liquid surfaces when accelerated in a direction perpendicular to their planes. I," Proceedings of the Royal Society of London. Series A. Mathematical and Physical Sciences **201**, 192 (1950).

12. R. D. Richtmyer, "Taylor Instability in Shock-Acceleration of Compressible Fluids," Communications on pure and applied mathematics **13**, 297 (1960).

13. E. E. Meshkov, "Instability of the interface of two gases accelerated by a shock wave," Fluid Dynamics **4**, 101 (1969).

14. D. L. Youngs, and R. J. Williams, "Turbulent mixing in spherical implosions," International journal for numerical methods in fluids **56**, 1597 (2008).

15. G. I. Bell, "Taylor instability on cylinders and spheres in the small amplitude approximation," Los Alamos National Laboratory, Los Alamos, NM, Report LA-1321 (1951).

16. M. Plesset, "On the stability of fluid flows with spherical symmetry," Journal of Applied Physics **25**, 96 (1954).

17. S. W. Haan, J. D. Lindl, D. A. Callahan, D. S. Clark, J. D. Salmonson, B. A. Hammel, L. J. Atherton, R. C. Cook, M. J. Edwards, S. Glenzer, A. V. Hamza, S. P. Hatchett, M. C. Herrmann, D. E. Hinkel, D. D. Ho, H. Huang, O. S. Jones, J. Kline, G. Kyrala, O. L. Landen, B. J. MacGowan, M. M. Marinak, D. D. Meyerhofer, J. L. Milovich, K. A. Moreno, E. I. Moses, D. H. Munro, A. Nikroo, R. E. Olson, K. Peterson, S. M. Pollaine, J. E. Ralph, H. F. Robey, B. K. Spears, P. T. Springer, L. J. Suter, C. A. Thomas, R. P. Town, R. Vesey, S. V. Weber, H. L. Wilkens, and D. C. Wilson, "Point design targets, specifications, and requirements for the 2010 ignition campaign on the National Ignition Facility," Physics of Plasmas **18**, 051001 (2011).

18. V. A. Thomas, and R. J. Kares, "Drive Asymmetry and the Origin of Turbulence in an ICF Implosion," Physical Review Letters **109**, 075004 (2012).

19. V. A. Smalyuk, R. E. Tipton, J. E. Pino, D. T. Casey, G. P. Grim, B. A. Remington, D. P. Rowley, S. V. Weber, M. Barrios, L. R. Benedetti, D. L. Bleuel, D. K. Bradley, J. A. Caggiano, D. A. Callahan, C. J. Cerjan, D. S. Clark, D. H. Edgell, M. J. Edwards, J. A. Frenje, M. Gatu-Johnson, V. Y. Glebov, S. Glenn, S. W. Haan, A. Hamza, R. Hatarik, W. W. Hsing, N. Izumi, S. Khan, J. D. Kilkenny, J. Kline, J. Knauer, O. L. Landen, T. Ma, J. M. McNaney, M. Mintz, A. Moore, A. Nikroo, A. Pak, T. Parham, R. Petrasso, D. B. Sayre, M. B. Schneider, R. Tommasini, R. P. Town, K. Widmann, D. C. Wilson, and C. B. Yeamans, "Measurements of an Ablator-Gas Atomic Mix in Indirectly Driven Implosions at the National Ignition Facility," Physical Review Letters **112**, 025002 (2014).

20. K. S. Raman, V. A. Smalyuk, D. T. Casey, S. W. Haan, D. E. Hoover, O. A. Hurricane, J. J. Kroll, A. Nikroo, J. L. Peterson, B. A. Remington, H. F. Robey, D. S. Clark, B. A. Hammel, O. L. Landen, M. M. Marinak, D. H. Munro, K. J. Peterson, and J. Salmonson, "An in-flight radiography platform to measure hydrodynamic instability growth in inertial confinement fusion capsules at the National Ignition Facility," Physics of Plasmas **21**, 072710 (2014).

21. D. T. Casey, D. T. Woods, V. A. Smalyuk, O. A. Hurricane, V. Y. Glebov, C. Stoeckl, W. Theobald, R. Wallace, A. Nikroo, M. Schoff, C. Shuldberg, K. J. Wu, J. A. Frenje, O. L. Landen, B. A. Remington, and G. Glendinning, "Performance and Mix Measurements of Indirect Drive Cu-Doped Be Implosions," Physical Review Letters **114**, 205002 (2015).

22. V. A. Smalyuk, D. T. Casey, D. S. Clark, M. J. Edwards, S. W. Haan, A. Hamza, D. E. Hoover, W. W. Hsing, O. Hurricane, J. D. Kilkenny, J. Kroll, O. L. Landen, A. Moore, A. Nikroo, L. Peterson, K. Raman, B. A. Remington, H. F. Robey, S. V. Weber, and K. Widmann, "First Measurements of Hydrodynamic Instability Growth in Indirectly Driven

Implosions at Ignition-Relevant Conditions on the National Ignition Facility," Physical Review Letters **112**, 185003 (2014).

23. T. Ma, P. K. Patel, N. Izumi, P. T. Springer, M. H. Key, L. J. Atherton, M. A. Barrios, L. R. Benedetti, R. Bionta, E. Bond, D. K. Bradley, J. Caggiano, D. A. Callahan, D. T. Casey, P. M. Celliers, C. J. Cerjan, J. A. Church, D. S. Clark, E. L. Dewald, T. R. Dittrich, S. N. Dixit, T. Döppner, R. Dylla-Spears, D. H. Edgell, R. Epstein, J. Field, D. N. Fittinghoff, J. A. Frenje, M. G. Johnson, S. Glenn, S. H. Glenzer, G. Grim, N. Guler, S. W. Haan, B. A. Hammel, R. Hatarik, H. W. Herrmann, D. Hicks, D. E. Hinkel, L. F. B. Hopkins, W. W. Hsing, O. A. Hurricane, O. S. Jones, R. Kauffman, S. F. Khan, J. D. Kilkenny, J. L. Kline, B. Kozioziemski, A. Kritcher, G. A. Kyrala, O. L. Landen, J. D. Lindl, S. L. Pape, B. J. MacGowan, A. J. Mackinnon, A. G. MacPhee, N. B. Meezan, F. E. Merrill, J. D. Moody, E. I. Moses, S. R. Nagel, A. Nikroo, A. Pak, T. Parham, H.-S. Park, J. E. Ralph, S. P. Regan, B. A. Remington, H. F. Robey, M. D. Rosen, J. R. Rygg, J. S. Ross, J. D. Salmonson, J. Sater, D. Sayre, M. B. Schneider, D. Shaughnessy, H. Sio, B. K. Spears, V. Smalyuk, L. J. Suter, R. Tommasini, R. P. J. Town, P. L. Volegov, A. Wan, S. V. Weber, K. Widmann, C. H. Wilde, C. Yeamans, and M. J. Edwards, "The role of hot spot mix in the low-foot and high-foot implosions on the NIF," Physics of Plasmas **24**, 056311 (2017).

24. D. S. Clark, C. R. Weber, J. L. Milovich, J. D. Salmonson, A. L. Kritcher, S. W. Haan, B. A. Hammel, D. E. Hinkel, O. A. Hurricane, O. S. Jones, M. M. Marinak, P. K. Patel, H. F. Robey, S. M. Sepke, and M. J. Edwards, "Three-dimensional simulations of low foot and high foot implosion experiments on the National Ignition Facility," Physics of Plasmas **23**, 056302 (2016).

25. T. Ma, P. K. Patel, N. Izumi, P. T. Springer, M. H. Key, L. J. Atherton, L. R. Benedetti, D. K. Bradley, D. A. Callahan, P. M. Celliers, C. J. Cerjan, D. S. Clark, E. L. Dewald, S. N. Dixit, T. Döppner, D. H. Edgell, R. Epstein, S. Glenn, G. Grim, S. W. Haan, B. A. Hammel, D. Hicks, W. W. Hsing, O. S. Jones, S. F. Khan, J. D. Kilkenny, J. L. Kline, G. A. Kyrala, O. L. Landen, S. Le Pape, B. J. MacGowan, A. J. Mackinnon, A. G. MacPhee, N. B. Meezan, J. D. Moody, A. Pak, T. Parham, H. S. Park, J. E. Ralph, S. P. Regan, B. A. Remington, H. F. Robey, J. S. Ross, B. K. Spears, V. Smalyuk, L. J. Suter, R. Tommasini, R. P. Town, S. V. Weber, J. D. Lindl, M. J. Edwards, S. H. Glenzer, and E. I. Moses, "Onset of Hydrodynamic Mix in High-Velocity, Highly Compressed Inertial Confinement Fusion Implosions," Physical Review Letters **111**, 085004 (2013).

26. S. Chandrasekhar, *Hydrodynamic and Hydrodynamic stability* (OUP, 1961).

27. J. Hecht, U. Alon, and D. Shvarts, "Potential flow models of Rayleigh–Taylor and Richtmyer–Meshkov bubble fronts," Physics of Fluids **6**, 4019 (1994).

28. D. Layzer, "On the Instability of Superposed Fluids in a Gravitational Field," The astrophysical journal **122**, 1 (1955).

29. U. Alon, J. Hecht, D. Ofer, and D. Shvarts, "Power Laws and Similarity of Rayleigh-Taylor and Richtmyer-Meshkov Mixing Fronts at All Density Ratios," Physical Review Letters **74**, 534 (1995).

30. V. N. Goncharov, "Analytical Model of Nonlinear, Single-Mode, Classical Rayleigh-Taylor Instability at Arbitrary Atwood Numbers," Physical Review Letters **88**, 134502 (2002).

31. S.-I. Sohn, "Simple potential-flow model of Rayleigh-Taylor and Richtmyer-Meshkov instabilities for all density ratios," Physical Review E **67**, 026301 (2003).

32. S. I. Abarzhi, K. Nishihara, and J. Glimm, "Rayleigh–Taylor and Richtmyer–Meshkov instabilities for fluids with a finite density ratio," Physics Letters A **317**, 470 (2003).

33. K. Read, "Experimental investigation of turbulent mixing by Rayleigh-Taylor instability," Physica D Nonlinear Phenomena **12**, 45 (1984).

34. M. J. Andrews, and D. B. Spalding, "A simple experiment to investigate two-dimensional mixing by Rayleigh–Taylor instability," Physics of Fluids A: Fluid Dynamics **2**, 922 (1990).

35. P. Linden, J. Redondo, and D. Youngs, "Molecular mixing in Rayleigh–Taylor instability," Journal of Fluid Mechanics **265**, 97 (1994).

36. G. Dimonte, and M. Schneider, "Turbulent Rayleigh-Taylor instability experiments with variable acceleration," Physical review E **54**, 3740 (1996).

37. M. B. Schneider, G. Dimonte, and B. Remington, "Large and small scale structure in Rayleigh-Taylor mixing," Physical review letters **80**, 3507 (1998).

38. G. Dimonte, and M. Schneider, "Density ratio dependence of Rayleigh–Taylor mixing for sustained and impulsive acceleration histories," Physics of Fluids **12**, 304 (2000).

39. D. L. Youngs, "Numerical simulation of turbulent mixing by Rayleigh-Taylor instability," Physica D: Nonlinear Phenomena **12**, 32 (1984).

40. D. L. Youngs, "Three-dimensional numerical simulation of turbulent mixing by Rayleigh–Taylor instability," Physics of Fluids A: Fluid Dynamics **3**, 1312 (1991).

41. D. L. Youngs, "Numerical simulation of mixing by Rayleigh–Taylor and Richtmyer–Meshkov instabilities," Laser and particle beams **12**, 725 (1994).

42. D. Oron, L. Arazi, D. Kartoon, A. Rikanati, U. Alon, and D. Shvarts, "Dimensionality dependence of the Rayleigh–Taylor and Richtmyer–Meshkov instability late-time scaling laws," Physics of Plasmas **8**, 2883 (2001).

43. G. Birkhoff, "University of California Report No," LA-1862 (1955).

44. C. Cherfils, and K. O. Mikaelian, "Simple model for the turbulent mixing width at an ablating surface," Physics of Fluids **8**, 522 (1996).

45. N. Inogamov, "Turbulent stage of the Rayleigh-Taylor instability," Pisma v Zhurnal Tekhnischeskoi Fiziki **4**, 743 (1978).

46. A. W. Cook, and P. E. Dimotakis, "Transition stages of Rayleigh–Taylor instability between miscible fluids," Journal of Fluid Mechanics **443**, 69 (2001).

47. G. Dimonte, D. Youngs, A. Dimits, S. Weber, M. Marinak, S. Wunsch, C. Garasi, A. Robinson, M. Andrews, and P. Ramaprabhu, "A comparative study of the turbulent Rayleigh–Taylor instability using high-resolution three-dimensional numerical simulations: the Alpha-Group collaboration," Physics of Fluids **16**, 1668 (2004).

48. H. Robey, P. Celliers, J. Kline, A. Mackinnon, T. Boehly, O. Landen, J. Eggert, D. Hicks, S. Le Pape, and D. Farley, "Precision shock tuning on the National Ignition Facility," Physical review letters **108**, 215004 (2012).

49. Y. Zhou, "Rayleigh–Taylor and Richtmyer–Meshkov instability induced flow, turbulence, and mixing. I," Physics Reports **720-722**, 1 (2017).

50. Y. Zhou, "Rayleigh–Taylor and Richtmyer–Meshkov instability induced flow, turbulence, and mixing. II," Physics Reports **723-725**, 1 (2017).

51. J. D. Lindl, R. L. Mccrory, and E. M. Campbell, "Progress toward Ignition and Burn Propagation in Inertial Confinement Fusion," Physics Today **45**, 32 (1992).

52. K. O. Mikaelian, "Stability and mix in spherical geometry," Physical review letters **65**, 992 (1990).

53. K. O. Mikaelian, "Rayleigh-Taylor and Richtmyer-Meshkov instabilities and mixing in stratified spherical shells," Physical Review A **42**, 3400 (1990).

54. C. Joggerst, A. Nelson, P. Woodward, C. Lovekin, T. Masser, C. L. Fryer, P. Ramaprabhu, M. Francois, and G. Rockefeller, "Cross-code comparisons of mixing during the implosion of dense cylindrical and spherical shells," Journal of Computational Physics **275**, 154 (2014).

55. M. Lombardini, D. Pullin, and D. Meiron, "Turbulent mixing driven by spherical implosions. Part 1. Flow description and mixing-layer growth," Journal of Fluid Mechanics **748**, 85 (2014).

56. M. Lombardini, D. Pullin, and D. Meiron, "Turbulent mixing driven by spherical implosions. Part 2. Turbulence statistics," Journal of Fluid Mechanics **748**, 113 (2014).

57. K. O. Mikaelian, "Rayleigh-Taylor and Richtmyer-Meshkov instabilities and mixing in stratified cylindrical shells," Physics of Fluids **17**, 094105 (2005).

58. M. Lombardini, and D. Pullin, "Small-amplitude perturbations in the three-dimensional cylindrical Richtmyer–Meshkov instability," Physics of Fluids **21**, 114103 (2009).

59. M. Lombardini, *Richtmyer-Meshkov instability in converging geometries* (California Institute of Technology, 2008).

60. K. Guderley, "Starke kugelige und zylindrische verdichtungsstosse in der nahe des kugelmitterpunktes bnw. der zylinderachse," Luftfahrtforschung **19**, 302 (1942).

61. R. Chisnell, "The motion of a shock wave in a channel, with applications to cylindrical and spherical shock waves," Journal of Fluid Mechanics **2**, 286 (1957).

62. G. Terrones, and M. D. Carrara, "Rayleigh-Taylor instability at spherical interfaces between viscous fluids: Fluid/vacuum interface," Physics of Fluids **27**, 054105 (2015).

63. J. D. Ramshaw, "Simple model for linear and nonlinear mixing at unstable fluid interfaces in spherical geometry," Physical Review E **60**, 1775 (1999).

64. O. Reynolds, "On the dynamical theory of incompressible viscous fluids and the determination of the criterion," Philosophical transactions of the royal society of london.(a.) **186**, 935 (1895).

65. S. B. Pope, *Turbulent flows* (2001).

66. J. Boussinesq, *Essai sur la théorie des eaux courantes* (Impr. nationale, 1877).

67. A. Smith, and T. Cebeci, "Numerical Solution of the Turbulent-Boundary-Layer Equations. Report No. DAC 33735 (Contract NOw 66-0324-C), Douglas Aircraft Co," Inc., May **29**, (1967).

68. B. Baldwin, and H. Lomax, *Thin-layer approximation and algebraic model for separated turbulent flows* (1978).

69. D. A. Johnson, and L. King, "A mathematically simple turbulence closure model for attached and separated turbulent boundary layers," AIAA journal **23**, 1684 (1985).

70. L. Prandtl, and K. Wieghardt, *Über ein neues Formelsystem für die ausgebildete Turbulenz* (Vandenhoeck & Ruprecht, 1947).

71. B. Baldwin, and T. Barth, *A one-equation turbulence transport model for high Reynolds number wall-bounded flows* (1991).

72. P. Spalart, and S. Allmaras, *A one-equation turbulence model for aerodynamic flows* (1992).

73. M. M. Rahman, T. Siikonen, and R. K. Agarwal, "Improved Low-Reynolds-Number One-Equation Turbulence Model," AIAA journal **49**, 735 (2011).

74. W. Jones, and B. Launder, "The calculation of low-Reynolds-number phenomena with a two-equation model of turbulence," International Journal of Heat and Mass Transfer **16**, 1119 (1973).

75. W. Jones, and B. E. Launder, "The prediction of laminarization with a two-equation model of turbulence," International journal of heat and mass transfer **15**, 301 (1972).

76. K. H. Ng, and D. B. Spalding, "Turbulence Model for Boundary Layers near Walls," The Physics of Fluids **15**, 20 (1972).

77. P. G. Saffman, and D. C. Wilcox, "Turbulence-Model Predictions for Turbulent Boundary Layers," AIAA journal **12**, 541 (1974).

78. J. Ilegbusi, and D. B. Spalding, "An improved version of the k-w model of turbulence," Heat Transfer 63 (1985).

79. P. G. Saffman, "A model for inhomogeneous turbulent flow," Proceedings of the Royal Society of London. A. Mathematical and Physical Sciences **317**, 417 (1970).

80. J. Rotta, "Statistische theorie nichthomogener turbulenz," Zeitschrift für Physik **129**, 547 (1951).

81. B. J. Daly, and F. H. Harlow, "Transport Equations in Turbulence," The Physics of Fluids **13**, 2634 (1970).

82. K. Hanjalić, and B. Launder, "A Reynolds stress model of turbulence and its application to thin shear flows," Journal of fluid Mechanics **52**, 609 (1972).

83. D. C. Besnard, F. H. Harlow, R. M. Rauenzahn, and C. Zemach, "Spectral transport model for turbulence," Theoretical and computational fluid dynamics **8**, 1 (1996).

84. C. Cambon, "Modélisation spectrale en turbulence homogène anisotrope," 1979.

85. C. Cambon, D. Jeandel, and J. Mathieu, "Spectral modelling of homogeneous non-isotropic turbulence," Journal of Fluid Mechanics **104**, 247 (1981).

86. J.-P. Bertoglio, *A Model of Three-Dimensional Transfer in Non-Isotropic Homogeneous Turbulence* (Springer Berlin Heidelberg, Berlin, Heidelberg, 1982).

87. J.-P. Bertoglio, and D. Jeandel, *A Simplified Spectral Closure for Inhomogeneous Turbulence: Application to the Boundary Layer* (Springer, 1987).

88. P. Chou, "On an extension of Reynolds method of finding apparent stress and the nature of turbulence," Chin. J. Phys **4**, (1940).

89. M. Millionshchikov, *On the theory of homogeneous isotropic turbulence* (1941).

90. T. T. Clark, and C. Zemach, "A spectral model applied to homogeneous turbulence," Physics of Fluids **7**, 1674 (1995).

91. D. Livescu, and J. Ristorcelli, "Variable-density mixing in buoyancy-driven turbulence," Journal of Fluid Mechanics **605**, 145 (2008).

92. J. André, and M. Lesieur, "Influence of helicity on the evolution of isotropic turbulence at high Reynolds number," Journal of Fluid Mechanics **81**, 187 (1977).

93. R. H. Kraichnan, "The structure of isotropic turbulence at very high Reynolds numbers," Journal of Fluid Mechanics **5**, 497 (1959).

94. I. Proudman, W. H. Reid, and G. I. Taylor, "On the decay of a normally distributed and homogenous turbulent velocity field," Philosophical Transactions of the Royal Society of London. Series A, Mathematical and Physical Sciences **247**, 163 (1954).

95. T. Tatsumi, and G. I. Taylor, "The theory of decay process of incompressible isotropic turbulence," Proceedings of the Royal Society of London. Series A. Mathematical and Physical Sciences **239**, 16 (1957).

96. R. H. Kraichnan, "Irreversible Statistical Mechanics of Incompressible Hydromagnetic Turbulence," Physical Review **109**, 1407 (1958).

97. W. Heisenberg, "On the theory of statistical and isotropic turbulence," Proceedings of the Royal Society of London. Series A. Mathematical and Physical Sciences **195**, 402 (1948).

98. E. E. O'Brien, and G. C. Francis, "A consequence of the zero-fourth-cumulant approximation in the decay of isotropic turbulence," Journal of Fluid Mechanics **13**, 369 (1962).

99. Y. Ogura, "A consequence of the zero-fourth-cumulant approximation in the decay of isotropic turbulence," Journal of Fluid Mechanics **16**, 33 (1963).

100. R. H. Kraichnan, "Lagrangian-History Closure Approximation for Turbulence," The Physics of Fluids **8**, 575 (1965).

101. C. E. Leith, "Diffusion Approximation to Inertial Energy Transfer in Isotropic Turbulence," The Physics of Fluids **10**, 1409 (1967).

102. S. A. Orszag, "Analytical theories of turbulence," Journal of Fluid Mechanics **41**, 363 (1970).

103. C. E. Leith, "Atmospheric Predictability and Two-Dimensional Turbulence," Journal of the Atmospheric Sciences **28**, 145 (1971).

104. R. H. Kraichnan, "An almost-Markovian Galilean-invariant turbulence model," Journal of Fluid Mechanics **47**, 512 (1971).

105. R. H. Kraichnan, "Test-field model for inhomogeneous turbulence," Journal of Fluid Mechanics **56**, 287 (1972).

106. M. J. Steinkamp, T. T. Clark, and F. H. Harlow, "Two-point description of two-fluid turbulent mixing—I. Model formulation," International Journal of Multiphase Flow **25**, 599 (1999).

107. M. Steinkamp, T. Clark, and F. Harlow, "Two-point description of two-fluid turbulent mixing—II. Numerical solutions and comparisons with experiments," International journal of multiphase flow **25**, 639 (1999).

108. N. Pal, S. Kurien, T. Clark, D. Aslangil, and D. Livescu, "Two-point spectral model for variable-density homogeneous turbulence," Physical Review Fluids **3**, 124608 (2018).

109. B. Fryxell, K. Olson, P. Ricker, F. Timmes, M. Zingale, D. Lamb, P. MacNeice, R. Rosner, J. Truran, and H. Tufo, "FLASH: An adaptive mesh hydrodynamics code for modeling astrophysical thermonuclear flashes," The Astrophysical Journal Supplement Series **131**, 273 (2000).

110. A. C. Calder, B. Fryxell, T. Plewa, R. Rosner, L. Dursi, V. Weirs, T. Dupont, H. Robey, J. Kane, and B. Remington, "On validating an astrophysical simulation code," The Astrophysical Journal Supplement Series **143**, 201 (2002).

111. A. Dubey, A. C. Calder, C. Daley, R. T. Fisher, C. Graziani, G. C. Jordan, D. Q. Lamb, L. B. Reid, D. M. Townsley, and K. Weide, "Pragmatic optimizations for better scientific utilization of large supercomputers," The International Journal of High Performance Computing Applications **27**, 360 (2013).

112. A. Dubey, K. Antypas, A. Calder, B. Fryxell, D. Lamb, P. Ricker, L. Reid, K. Riley, R. Rosner, and A. Siegel, *The software development process of FLASH, a multiphysics simulation code* (IEEE Press, 2013).

113. A. Lawrie, "Rayleigh-Taylor mixing: confinement by stratification and geometry," University of Cambridge, 2010.

114. A. G. Lawrie, and S. B. Dalziel, "Turbulent diffusion in tall tubes. I. Models for Rayleigh-Taylor instability," Physics of Fluids **23**, 085109 (2011).

115. P. Ramaprabhu, V. Karkhanis, and A. G. Lawrie, "The Rayleigh-Taylor Instability driven by an accel-decel-accel profile," Physics of Fluids **25**, 115104 (2013).

116. P. Ramaprabhu, V. Karkhanis, R. Banerjee, H. Varshochi, M. Khan, and A. Lawrie, "Evolution of the single-mode Rayleigh-Taylor instability under the influence of time-dependent accelerations," Physical Review E **93**, 013118 (2016).

117. P. Colella, and P. R. Woodward, "The piecewise parabolic method (PPM) for gas-dynamical simulations," Journal of computational physics **54**, 174 (1984).

118. P. MacNeice, K. M. Olson, C. Mobarry, R. De Fainchtein, and C. Packer, "PARAMESH: A parallel adaptive mesh refinement community toolkit," Computer physics communications **126**, 330 (2000).

119. G. Strang, "On the construction and comparison of difference schemes," SIAM journal on numerical analysis **5**, 506 (1968).

120. F. F. Grinstein, L. G. Margolin, and W. J. Rider, *Implicit large eddy simulation: computing turbulent fluid dynamics* (Cambridge university press, 2007).

121. A. Aspden, N. Nikiforakis, S. Dalziel, and J. Bell, "Analysis of implicit LES methods," Communications in Applied Mathematics and Computational Science **3**, 103 (2009).

122. W. H. Cabot, and A. W. Cook, "Reynolds number effects on Rayleigh–Taylor instability with possible implications for type Ia supernovae," Nature Physics **2**, 562 (2006).

123. D. Livescu, J. Ristorcelli, R. Gore, S. Dean, W. Cabot, and A. Cook, "High-Reynolds number Rayleigh–Taylor turbulence," Journal of Turbulence N13 (2009).

124. D. Livescu, J. Ristorcelli, M. Petersen, and R. Gore, "New phenomena in variable-density Rayleigh–Taylor turbulence," Physica Scripta **2010**, 014015 (2010).

125. P. Ramaprabhu, G. Dimonte, and M. Andrews, "A numerical study of the influence of initial perturbations on the turbulent Rayleigh–Taylor instability," Journal of Fluid Mechanics **536**, 285 (2005).

126. J. Ristorcelli, and T. Clark, "Rayleigh–Taylor turbulence: self-similar analysis and direct numerical simulations," Journal of Fluid Mechanics **507**, 213 (2004).

127. D. L. Youngs, "Modelling turbulent mixing by Rayleigh-Taylor instability," Physica D: Nonlinear Phenomena **37**, 270 (1989).

128. D. L. Youngs, "The density ratio dependence of self-similar Rayleigh–Taylor mixing," Philosophical Transactions of the Royal Society A: Mathematical, Physical and Engineering Sciences **371**, 20120173 (2013).

129. J. D. Schwarzkopf, D. Livescu, R. A. Gore, R. M. Rauenzahn, and J. R. Ristorcelli, "Application of a second-moment closure model to mixing processes involving multicomponent miscible fluids," Journal of Turbulence N49 (2011).

130. D. L. Sandoval, The dynamics of variable-density turbulence Document No. Number, 1995.

131. M. Lombardini, D. Hill, D. Pullin, and D. Meiron, "Atwood ratio dependence of Richtmyer–Meshkov flows under reshock conditions using large-eddy simulations," Journal of fluid mechanics **670**, 439 (2011).

132. R. L. Holmes, G. Dimonte, B. Fryxell, M. L. Gittings, J. W. Grove, M. Schneider, D. H. Sharp, A. L. Velikovich, R. P. Weaver, and Q. Zhang, "Richtmyer–Meshkov instability growth: experiment, simulation and theory," Journal of Fluid Mechanics **389**, 55 (1999).

133. B. Thornber, J. Griffond, O. Poujade, N. Attal, H. Varshochi, P. Bigdelou, P. Ramaprabhu, B. Olson, J. Greenough, and Y. Zhou, "Late-time growth rate, mixing, and anisotropy in the multimode narrowband Richtmyer–Meshkov instability: The θ-group collaboration," Physics of Fluids **29**, 105107 (2017).

134. T. B., G. J., B. P., B. I., R. P., S. O., and J. R. W. R., "Turbulent transport and mixing in the multimode narrowband Richtmyer-Meshkov instability," To appear in Physics of Fluids (2019).

135. M. Latini, O. Schilling, and W. S. Don, "High-resolution simulations and modeling of reshocked single-mode Richtmyer-Meshkov instability: Comparison to experimental data and to amplitude growth model predictions," Physics of Fluids **19**, 024104 (2007).

136. O. Schilling, M. Latini, and W. S. Don, "Physics of reshock and mixing in single-mode Richtmyer-Meshkov instability," Physical Review E **76**, 026319 (2007).

137. B. Balakumar, G. Orlicz, J. Ristorcelli, S. Balasubramanian, K. Prestridge, and C. Tomkins, "Turbulent mixing in a Richtmyer–Meshkov fluid layer after reshock: velocity and density statistics," Journal of Fluid Mechanics **696**, 67 (2012).

138. B. Balakumar, G. Orlicz, C. Tomkins, and K. Prestridge, "Simultaneous particle-image velocimetry–planar laser-induced fluorescence measurements of Richtmyer–Meshkov instability growth in a gas curtain with and without reshock," Physics of Fluids **20**, 124103 (2008).

139. S. Balasubramanian, G. Orlicz, K. Prestridge, and B. Balakumar, "Experimental study of initial condition dependence on Richtmyer-Meshkov instability in the presence of reshock," Physics of fluids **24**, 034103 (2012).

140. B. M. Haines, F. F. Grinstein, L. Welser-Sherrill, and J. R. Fincke, "Simulations of material mixing in laser-driven reshock experiments," Physics of Plasmas **20**, 022309 (2013).

141. G. Malamud, E. Leinov, O. Sadot, Y. Elbaz, G. Ben-Dor, and D. Shvarts, "Reshocked Richtmyer-Meshkov instability: Numerical study and modeling of random multi-mode experiments," Physics of Fluids **26**, 084107 (2014).

142. J. McFarland, D. Reilly, S. Creel, C. McDonald, T. Finn, and D. Ranjan, "Experimental investigation of the inclined interface Richtmyer–Meshkov instability before and after reshock," Experiments in fluids **55**, 1640 (2014).

143. J. A. McFarland, J. A. Greenough, and D. Ranjan, "Simulations and analysis of the reshocked inclined interface Richtmyer–Meshkov instability for linear and nonlinear interface perturbations," Journal of Fluids Engineering **136**, 071203 (2014).

144. M. Karnig O, private communication (2019).

145. K. O. Mikaelian, "Freeze-out and the effect of compressibility in the Richtmyer–Meshkov instability," Physics of Fluids **6**, 356 (1994).

146. K. Mikaelian, "Testing an analytic model for Richtmyer–Meshkov turbulent mixing widths," Shock Waves **25**, 35 (2015).

147. K. Meyer, and P. Blewett, "Numerical Investigation of the Stability of a Shock-Accelerated Interface between Two Fluids," The Physics of Fluids **15**, 753 (1972).

148. G. Dimonte, and P. Ramaprabhu, "Simulations and model of the nonlinear Richtmyer–Meshkov instability," Physics of Fluids **22**, 014104 (2010).

149. M. Brouillette, "The richtmyer-meshkov instability," Annu Rev Fluid Mech **34**, 445 (2002).

150. Q. Zhang, and M. J. Graham, "A numerical study of Richtmyer–Meshkov instability driven by cylindrical shocks," Physics of Fluids **10**, 974 (1998).

151. R. Chisnell, "An analytic description of converging shock waves," Journal of Fluid Mechanics **354**, 357 (1998).

152. A. Nelson, and P. Ramaprabhu, *Large amplitude nonlinear Richtmyer-Meshkov instability in convergent geometries* (Springer, 2013).

153. T. Nelson, "Shock-driven fluid instabilities in convergent geometries," University of North Carolina at Charlotte, 2013.

154. D. L. Youngs, "Time-dependent multi-material flow with large fluid distortion," Numerical methods for fluid dynamics (1982).

155. N. M. Hoffman, B. A. Hammel, and O. Schilling, *Calibrating mix models for NIF tuning* (IOP Publishing, 2010).

156. Y. Zhou, H. F. Robey, and A. C. Buckingham, "Onset of turbulence in accelerated high-Reynolds-number flow," Physical Review E **67**, 056305 (2003).

157. Y. Zhou, B. Remington, H. Robey, A. Cook, S. Glendinning, A. Dimits, A. Buckingham, G. Zimmerman, E. Burke, and T. Peyser, "Progress in understanding turbulent mixing induced by Rayleigh–Taylor and Richtmyer–Meshkov instabilities," Physics of Plasmas **10**, 1883 (2003).

158. Y. Zhou, "Unification and extension of the similarity scaling criteria and mixing transition for studying astrophysics using high energy density laboratory experiments or numerical simulations," Physics of Plasmas **14**, 082701 (2007).

159. Y. Zhou, and B. Thornber, "A comparison of three approaches to compute the effective Reynolds number of the implicit large-eddy simulations," Journal of Fluids Engineering **138**, 070905 (2016).

160. J. A. McFarland, and M. Hagenmaier, "Computational Study of Shock-Driven Multiphase Mixing in Scramjet Conditions," AIAA Journal **56**, 4004 (2018).

161. P. K. Ramaprabhu, "On the dynamics of Rayleigh-Taylor mixing," Texas A&M University, 2004.

APPENDIX: NUMERICAL CONVERGENCE STUDY & CHARACTERISATION OF NUMERICAL VISCOSITY IN ILES CALCULATIONS

A.1 Grid Resolution Convergence Study:

In this section, we discuss the numerical convergence of the spherical implosion simulation results obtained in chapter 6. We note the highest resolution cases (256 zones and 512 zones) are converged with respect to several quantities such as the mixing width $\delta(t)$ shown in Figure 6.9(a) and the product mixing widths $\wp(t)$, shown in Figure 6.9(b), with the lowest resolution case (128 zones), as expected, showing some discrepancy. Similarly, in Figure 6.11, the TKE profiles are in reasonable agreement for the simulations with 256 and 512 zones, while the lower resolution case is considerably different. We further demonstrate the 512 zone case presented here is converged by comparing with results from a simulation with 1024 zones in the figures below. (The 1024 zone simulation dataset is not included in chapter 6 results, but will be the focus of a separate paper).

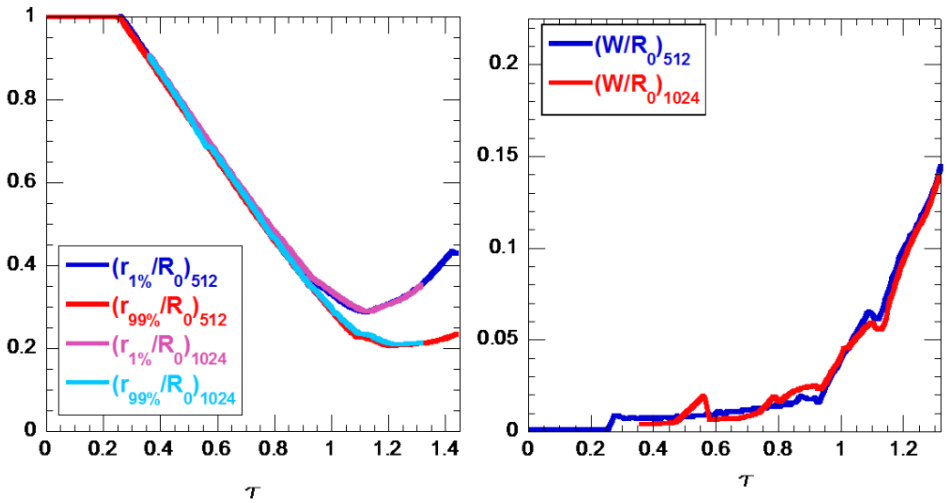

Figure A1 (a) Time histories of the radial locations of the 1% and 99% surfaces from simulations with 512 and 1024 zones respectively. (b) Time evolution of the mixing layer amplitude from simulations with 512 zones and 1024 zones respectively.

A.2 Study of the Effect of Fusing Mesh Cells near the Origin:

As the transmitted shock approaches the origin point, an AMR mesh would mandate CFL numbers → 0, thereby making the computations prohibitively expensive. We address this issue by azimuthally fusing the mesh cells near the origin, while maintaining sufficient radial resolution to resolve the shock. This strategy ensures the 1D radial shock continues to be adequately resolved, while avoiding additional computational overhead. Care is also taken to fused-mesh region is never breached by the turbulent mixing layer.

We quantify the error from the fused mesh approach in figures A2 below. The maximum discrepancy between the local values of pressure between the two cases never exceeds 10% at any time. At all other times, the two cases are in excellent agreement as demonstrated in the series of figures below. In figs. A2 (a) – (e), we plot the radial profiles of pressure and density from simulations with local de-refinement and full resolution, and at times corresponding to the interface images in Figure 6.6 (a) – (b). In each of these images, the pressure and density profiles are in excellent agreement for the two. Further, we compare the time history of the unperturbed interface from the simulations with and without the local mesh de-refinement in figure A3. Both simulations are in excellent agreement with each other for $R_{unperturbed}(t)$.

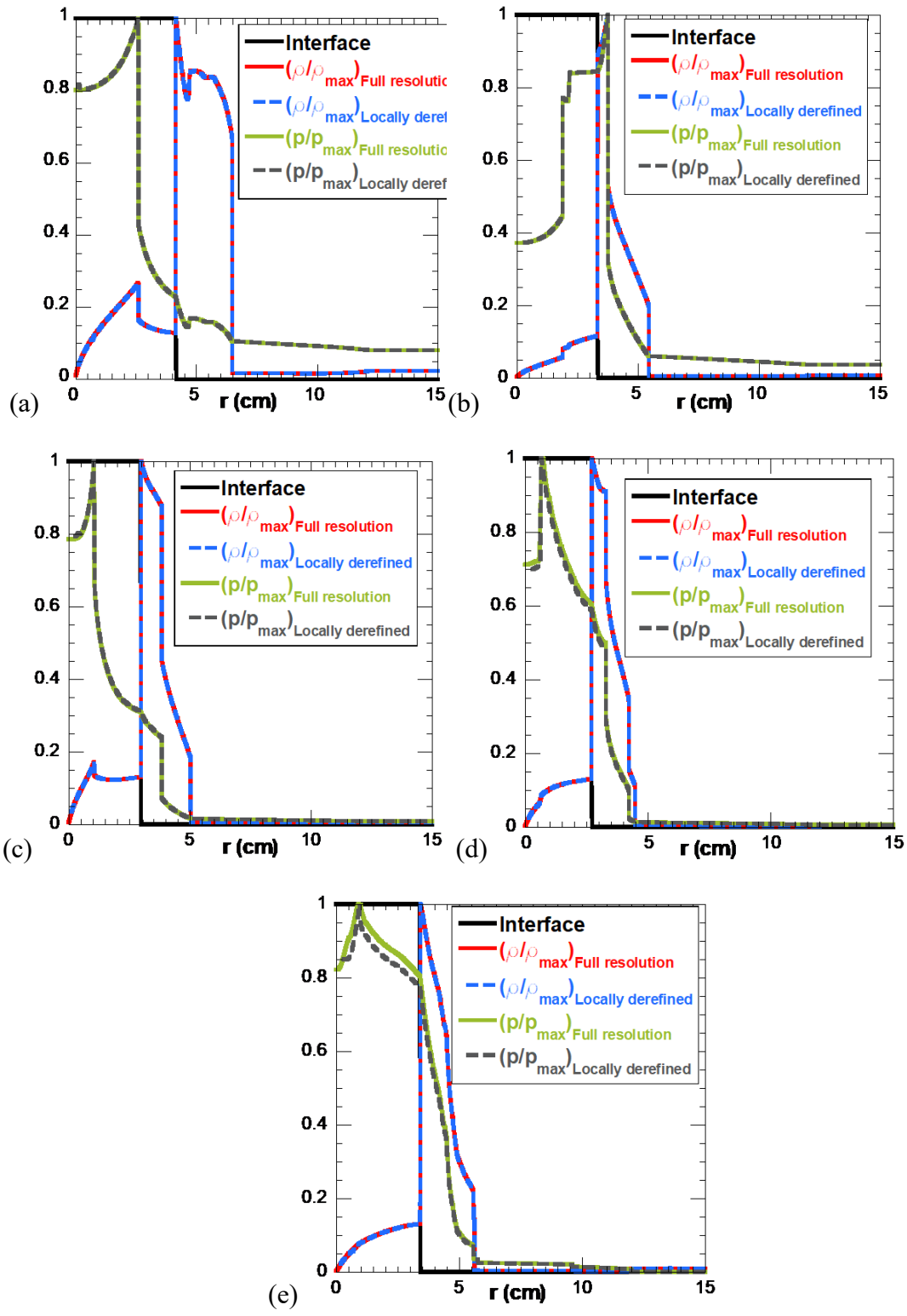

Figure A2 (a) – (e) Radial profiles of pressure and density at the times corresponding to figure 6.6 (a) – (e) in Chapter 6.

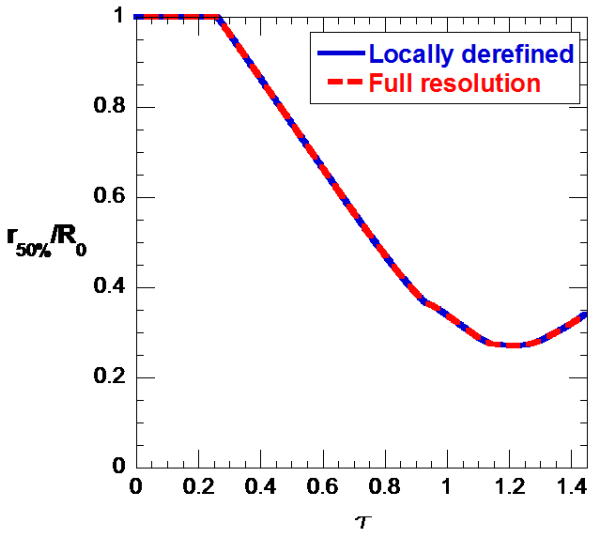

Figure A3 Time history of the location of the unperturbed interface from simulations with the full resolution and local mesh de-refinement.

A.3 Characterization of Numerical Viscosity in ILES Calculations:

The simulations presented here fall under the definition of Implicit Large Eddy Simulations (ILES), where the mixing between fluids is numerical. In these methods, small-scale dissipation is modeled numerically, thus eliminating the need for an explicit sub-grid filter with tunable coefficients. Such approaches have been widely used in the study of flows with sharp discontinuities and shocks, and have been considered desirable in such applications due to their monotonicity-preserving attributes. In contrast, the use of Direct Numerical Simulation (DNS) approaches would require the interfaces between fluids to be diffuse initially, to avoid oscillations.

The following approach can be used to infer a numerical viscosity and effective Reynolds numbers from our ILES simulations. From the kinetic energy spectra, we determine the inner viscous length scale λ_v as the intersection point between the fiducials corresponding to the inertial and the dissipation ranges in figure 6.14. For $\tau = 1.44$, we find $k_v R(t) \sim 220$,

where $k_v = 2\pi/\lambda_v$ and R(t) is the location of the corresponding unperturbed interface. The outer length scale is given by $\delta \sim W(t)$, where W(t) is the amplitude of the turbulent mixing layer, so that the effective Reynolds number is obtained as [156-159] $Re = \left(50\,{}^{\delta}/_{\lambda_v}\right)^{4/3} \sim 1.1e4$. A similar analysis conducted at $\tau = 0.95$, yields $k_v R(t) \sim 410$ and Re ~ 1.25e3.